Title	Evaluation of SIFs for Fatigue Cracks in Welding Residual Stress Fields Using the Crack Face Traction Force Analysis
Author(s)	Gadallah, Ramy Saeed Shafeak
Citation	大阪大学, 2017, 博士論文
Version Type	VoR
URL	https://doi.org/10.18910/67160
rights	
Note	

Osaka University Knowledge Archive : OUKA

https://ir.library.osaka-u.ac.jp/

Osaka University

Doctoral Dissertation

Evaluation of SIFs for Fatigue Cracks in Welding Residual Stress Fields Using the Crack Face Traction Force Analysis

き裂面分布応力を用いた溶接残留応力場中にある疲労き裂の応力拡大係数評価

Ramy Saeed Shafeak Gadallah

July 2017

Department of Naval Architecture and Ocean Engineering
Division of Global Architecture
Graduate School of Engineering
Osaka University

Dedication

To

My parents

Abstract

Cracks, in general, are considered one of the main factors that influence the structural integrity of welded structures such as ships, offshore structures, bridges, constructions, etc. As well, cracks are frequently found in complicated residual stress (RS) fields. Further, surface cracks may occur in several structural components and take various shapes, for example, cracks in fillet-welded joints show long shallow shapes (i.e. semi-elliptical surface cracks). For a reliable prediction of fatigue crack propagation life and fracture strength, accurate stress intensity factor (SIF) solutions along the crack front are needed. Therefore, in order to obtain accurate SIF solutions for surface cracks in welding RS stress fields, the influence of RS field must be included when calculating SIF.

This study is composed of seven chapters, as follows:

1) Chapter 1 gives a background on RS produced due to welding and their influence on the integrity of structures. As well, cracks, their types, and existence of cracks in RS fields are addressed. The concept of the SIF and the principle of superposition are also reviewed. This chapter also discusses the challenges, faced problems, objectives and outlook related to this study.

2) Chapter 2 addresses a background on the numerical integration methods that used in SIF evaluation for 3-D cracks with crack face tractions. In addition, this chapter reviews the formulation of the domain integral (DI) method and the interaction integral method (IIM) that form the basis of the numerical procedures used in this study.

3) In chapter 3, the superposition method was numerically validated using different FE models and solvers by employing the MSC Marc-DI and WARP3D-IIM. Furthermore, the significance and effectiveness of the crack face traction integral (CFT-integral) in improving the accuracy of the CFT-solution was discussed. It was found that, when the WARP3D-IIM that implements the CFT-integral, the difference between the solutions obtained by the external loading and CFT is less than 0.5% at the crack deepest point in the case of flat plate model. However, the CFT-integral implemented in WARP3D-IIM is valid only for a uniform distributed stress field over the crack face. On the other hand, a difference of less than 5% was obtained at the crack deepest point between the solutions computed by external loading and crack nodal traction (CNT) for the flat plate model and T-butt welded model, when MSC Marc-DI was employed that omits the CFT-integral. Based on that, commercial nonlinear FE codes that neglect the CFT-

integral (e.g. MSC Marc) can be used to give a rough estimation of SIF for engineering fracture mechanics problems using traction force analysis under the conditions examined in this study.

4) Chapter 4 introduces a proposed technique in order to evaluate the SIF (K_I) for a semi-elliptical surface cracks in welding RS fields. The proposed technique based on two main points: 1) utilizing the CFT-integral implemented in WARP3D-IIM, and 2) using a particular crack-block mesh density. The crack-block mesh density showed a significant influence on the calculated CFT-solutions along the crack front under different loading conditions. It was observed that when the crack-block mesh becomes fine enough, the smoothness and accuracy of the CFT-solutions are improved. The results of the different numerical examples presented in this chapter showed an excellent agreement between the CFT-solutions and those given by external loading along the crack front especially at the crack deepest point when the proposed technique was employed. A percentage difference of less than 1% was obtained at the crack deepest point between the CFT-solution and that given by external loading for all the numerical examples studied in this chapter. As well, the proposed technique was validated for a butt-welded joint using a calculated welding RS. The SIF solutions calculated by the proposed technique gave excellent agreement along the crack front with those obtained by the reference solution. Furthermore, the proposed technique was employed to calculate SIF for a surface cracked butt-welded joint using real welding RS. The SIF solutions calculated by real welding RS showed good agreement with the solution obtained by external loading. As well, negative SIF solutions were given when a compressive welding RS was used. On the other hand, it was found that simplification of welding RS has a clear influence on the calculated SIF. Therefore, actual welding RS distribution is highly recommended to be used in order to obtain accurate and realistic SIF solutions. Further, for the results obtained by MSC Marc-DI, a percentage difference of less than 4% was obtained at the crack deepest point between the CNT-solutions and those calculated by external loading for the different numerical examples. Thus, commercial FE packages that omit the CFT-integral can be utilized to evaluate SIF roughly for surface cracks in non-uniform stress fields for engineering problems under the conditions examined in this chapter.

5) Chapter 5 conducts a comprehensive validation study based on the proposed technique that discussed in chapter 4. This chapter investigates the influence of the change in

welding heat input (HI) on welding simulation results and the behavior of SIF and fatigue crack propagation (FCP) for a bead-on-plate model. The results showed that the change in welding HI has a clear influence on welding penetration, welding distortion and welding RS distribution. However, the change in welding HI did not give considerable impact on the behavior of SIF and FCP for the applied welding HI cases and selected FE model. Based on that, a fundamental study was conducted to understand why no clear influence was obtained in the behavior of SIF and FCP when welding HI changed. It is observed that when the difference in the applied RS is small, the RS has a negligible influence on the behavior of SIF and FCP. However if the difference in the applied RS is large, the RS reveals a considerable impact on the behavior of SIF and FCP. On the other hand, the results revealed that welding RS has a significant influence on the behavior of SIF and FCP when compared with those neglect the influence of welding RS. When welding RS included in SIF solutions, SIF magnitude drastically increased compared to the case of no welding RS. Therefore, a large reduction in the calculated fatigue lives was observed when welding RS taken into account. A reduction percentage of 37.8%–49.3% in fatigue lives was obtained for the applied stress amplitude loadings. Moreover, the calculated fatigue lives based on the proposed technique that adopted for computing SIF solutions considering welding RS were validated with experiments. As well, the accuracy of the calculated fatigue lives were verified with simulated data.

6) In chapter 6, the WARP3D-IIM was modified based on the Cauchy stress tensor approach in which the normal and shear stress components (i.e. 6-components of stress) can be included in the calculation of the traction forces when a simulated or real RS field is applied to the crack face. Based on that, mixed-mode SIFs of complicated welded geometries and complex welding RS fields can be calculated accurately. To verify the adequacy of the modified WARP3D-IIM, an inclined penny crack in an infinite body was examined. Two FE numerical examples were studied using different crack mesh softwares (i.e. Zencrack and FEAcrack). To validate the calculated mixed-mode SIFs (K_I, K_{II} and K_{III}) for the inclined penny crack problem, the SIFs obtained by the external loading using the WARP3D-IIM was verified firstly with analytical solutions. The percentage difference between the SIFs obtained by the external loading and analytical equations is less than 0.3% for the Zencrack mesh and less than 0.05% for the FEAcrack mesh at the crack deepest point. The superposition method was thereafter employed to

evaluate the mixed-mode SIFs based on the modified WARP3D-IIM when a non-uniform stress field with normal and shear components is applied to the crack face. The mixed-mode SIFs calculated by CFT were validated with those given by the external loading for the two numerical examples. A percentage difference of less than 1% was obtained between the SIFs computed by CFT and those given by the external loading at the crack deepest point for the Zencrack mesh. On the other hand, a percentage difference of less than 0.5% was obtained at the crack deepest point for the FEAcrack mesh. It is observed that the behavior of the CFT-SIFs given by Zencrack mesh is not smooth at some locations at and near the crack front. This behavior may be due to the geometry of the crack face elements adjacent to the crack front. Therefore, an appropriate crack mesh must be employed in order to obtain accurate and smooth SIFs.

7) Chapter 7 summarizes the conclusions of the main points in this study. This chapter also discusses further works that may improve the effectiveness and adequacy of the proposed technique.

Table of contents

Nomenclature

Symbols

$1/\sqrt{r}$ = singularity of stress field

a = crack depth, mm

a/c = crack depth-to-crack length ratio

a/t = crack depth-to-model thickness ratio

a_1 = minimum element size in thickness direction, mm

c = crack half-length, mm

C & m = fatigue crack propagation material constants

C_{ijkl} = consecutive tensor

E = Young's modulus, GPa

E^* = effective Young's modulus

F_T = forecast value at time T

F_{T+1} = forecast value at time $T+1$

$I(s)$ = interaction integral at crack front location s

$\bar{I}(s)$ = integral with interacting actual and auxiliary term

$J(s)$ = J-integral at crack front location s

$\bar{J}(s)$ = energy released per unit advance of crack front segment, L_C

K_I = mode-I stress intensity factor, MPa.mm$^{1/2}$

K_{II} = mode-II stress intensity factor, MPa.mm$^{1/2}$

K_{III} = mode-III stress intensity factor, MPa.mm$^{1/2}$

K_{Imin} = minimum stress intensity factor for mode-I, MPa.mm$^{1/2}$

K_{Imax} = maximum stress intensity factor for mode-I, MPa.mm$^{1/2}$

K_{In} = non-dimensional mode-I stress intensity factor (=$K_I/\sigma_o\sqrt{\pi a/Q}$)

L_C = crack front segment

n_i = normal vector components

P = applied load/stress, MPa

q = weight function

Q = shape parameter for elliptical and semi-elliptical cracks

q_T = actual, known series value at time T
r = distance from the crack front
R = stress ratio
R^* = local stress ratio
R^+ = stress ratio including clamping stress
s = node location along the crack front
S = surface
S^+ = upper crack face
S^- = lower crack face
t = thickness, mm
T = time
T_{Ms} = martensitic transformation start temperature, ^{o}C
$T_j^{(n)}$ = stress vector
t_j = crack face traction components
U = total strain energy
U^* = stress range ratio
u^* & w = longitudinal displacements for duplicate nodes on the crack faces
u_j = displacement components
U_x, U_y & U_z = displacement in x-, y- and z-directions, respectively
V = volume
W = strain energy density
ΔK = stress intensity factor range, MPa.mm$^{1/2}$
ΔK_{eff} = effective stress intensity factor range, MPa.mm$^{1/2}$
ΔK_{th} = threshold stress intensity factor range, MPa.mm$^{1/2}$

Greek symbols

θ = angle of inclination for an element far from the crack front with a distance r
α = smoothing constant
δ_{1i} = Kronecker delta
$\Delta\sigma$ = stress range

$\Delta\sigma_{eff}$ = effective stress range

ε_{ij} = strain components

ν = Poisson’s ratio

ρ = material density, g/mm^3

ρ^* = weld toe radius, mm

$\boldsymbol{\sigma}$ = stress tensor

σ = normal stress, MPa

σ_o = loading acting on the model boundary (maximum stress), MPa

σ_{cl} = clamping stress

σ_{ij} = stress components

σ_{max} = maximum stress

σ_{min} = minimum stress

σ_Y = yield stress, MPa

τ = shear stress, MPa

φ = parameter angle for the ellipse, deg.

Acronyms

BOP = bead-on-plate

CFT = crack face traction

CMOD = crack mouth opening displacement, mm

CNT = crack nodal traction

CTOD = crack tip opening displacement

DI = domain integral

FCP = fatigue crack propagation

FE = finite element

FEA = finite element analysis

FEM = finite element method

HI = heat input, KJ/mm

IIM = interaction integral method

LTT = low transformation temperature

RBE2 = rigid body element

RS = residual stress
SIF = stress intensity factor (mode-I)
SIFs = stress intensity factors (mode-I, mode-II and mode-III)
TEP = thermal-elastic-plastic
VCCM = virtual crack closure method

Superscripts

aux = auxiliary state
I = interaction integral
S = superimposed state

Subscripts

x, y, z = in x-, y-, z-directions, respectively
xx, yy, zz = in x-, y-, z-directions, respectively, used for normal stress components
xy, yz, xz = in xy-, yz-, xz-directions, respectively, used for shear stress components

CHAPTER 1

Introduction

1.1 Background

Welding, nowadays, is one of the most important manufacturing tools used in the construction industry including ships, offshore structures, bridges, constructions, etc. Welding offers various advantages such as simple set up, low manufacturing cost and high joint efficiency. However, due to the non-uniform temperature distributions produced by welding, inevitable residual stress (RS) is obtained[1][2]. RS is considered one of the major problems that induced due to welding. Since many of welded structures subject to external cyclic loadings, therefore the presence of welding RS in these structures can considerably influence the fatigue life[3][4]. Due to the superposition of external tensile cyclic loading with welding RS, a reduction in the maximum endurable load of a structure occurs especially when welding RS is tensile[5]. This reveals that welding tensile RS is generally detrimental to fatigue life where it increases the rate of fatigue crack propagation (FCP). On the other hand, there is also the possibility of flaws, e.g. cracks, being created due to welding. The presence of a crack in a RS field is highly risky for a structure integrity.

Due to the high tensile RS as well as stress concentration, welded joints are targets for cracks formation. Cracks, in general, are considered one of the main factors that influence the structural integrity of welded structures. In service, since welded joints subject to external loading in addition to the existence of RS, cracks may easily propagate leading to a premature failure of a structure. The type of crack propagation determines the failure type. For example, sudden crack propagation leads to brittle fracture; however, gradual crack propagation leads to fatigue, creep or corrosion fracture. There are different crack types that form in steel welded joints such as hot cracks, cold cracks, fatigue cracks and corrosion cracks. Hot cracks and cold cracks are formed in and around the weld. Hot cracks are created during the cooling process while the weld temperature is high. However, cold cracks are produced after the weld has cooled down. On the other hand, fatigue cracks and corrosion cracks may form in and near the weld. Fatigue cracks, which frequently initiate at weld toe and weld root, form due to RS and stress concentration that assist in the initiation and then propagation in the presence of external cyclic loadings. Figure 1.1 shows different types of cracks that form in welded joints. For further details on the cracks types, causes and remedies refer to Refs.[6][7].

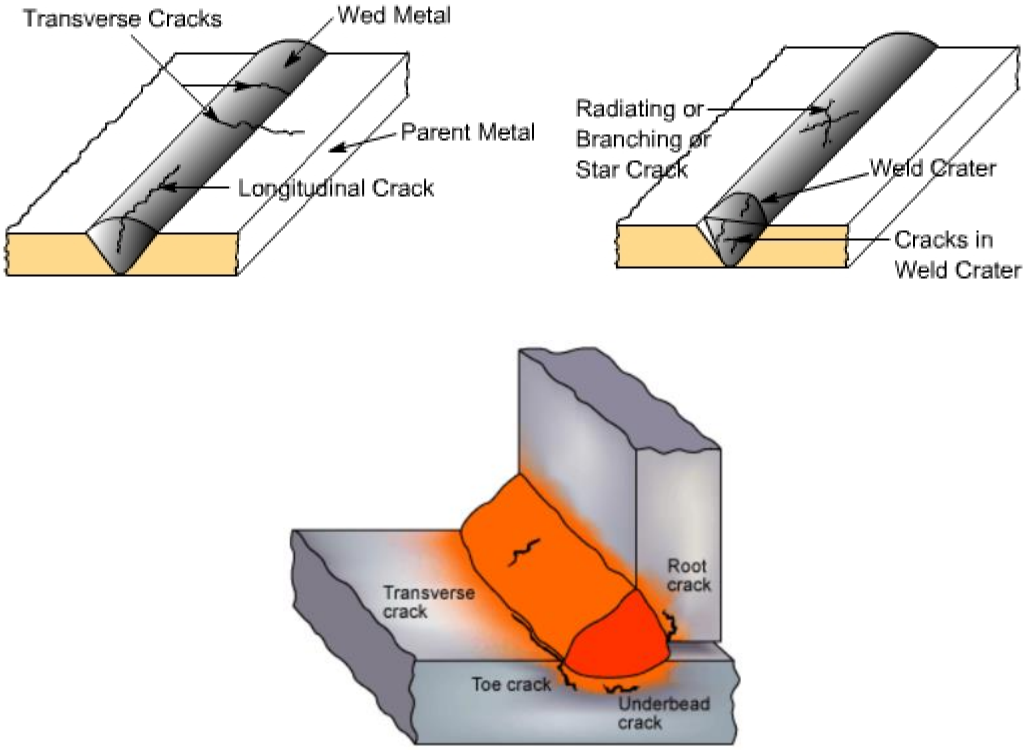

Fig. 1.1 Schmatic drawing of typical locations of cracks in welded joints.

Engineering structures generally have complex configurations in which cracks often initiate at the locations of high stress concentration[8]. Surface cracks may occur in several structural components and take various shapes, for example, surface cracks in fillet welded joints show long shallow shapes (i.e. semi-elliptical surface cracks). Surface cracks frequently initiate at the regions of stress concentrations such as at the weld toe of welded joints which may cause an early failure of the joint[9][10]. In the case of surface cracks that initiate at the weld toe of weld joints, the situation is complicated. This is due to the high stress concentration as well as the large RS values at the weld toe. Geometrical parameters of fillet welded joints such as the shape of the weld bead and weld toe angle not only influence the stress distribution when the weld joint does not include a crack, but also will cause a change in the stress intensity factors (SIFs) distribution when a crack exists in the weld joint[11]. The evaluation of SIFs is a key step in a structural integrity analysis for a damaged structure with fatigue cracks or stress corrosion cracking[12][13].

1.2 The concept of stress intensity factor

For fracture phenomena, the local stress field close to the crack front is crucial. The stress rises to a singularity at the sharp crack front. The SIF defines the intensity of the crack front singularity. The intensity of this singularity relies on the magnitude of the relevant structural stresses. Stresses close to the crack front increase in proportion to SIF, see Fig. 1.2(a). Furthermore, the conditions of the crack front are completely defined based on SIF. For example, if SIF is known, it is possible to solve for all components of stress, strain and displacement as a function of r and θ, see Fig. 1.2(b). For example, Eqns. 1.1–1.5 show how stress components may be calculated based on the SIF at a stressed element near the crack front. The SIF is represented mathematically by the variable K. The SIF is therefore considered one of the most important concepts in fracture mechanics[14][15].

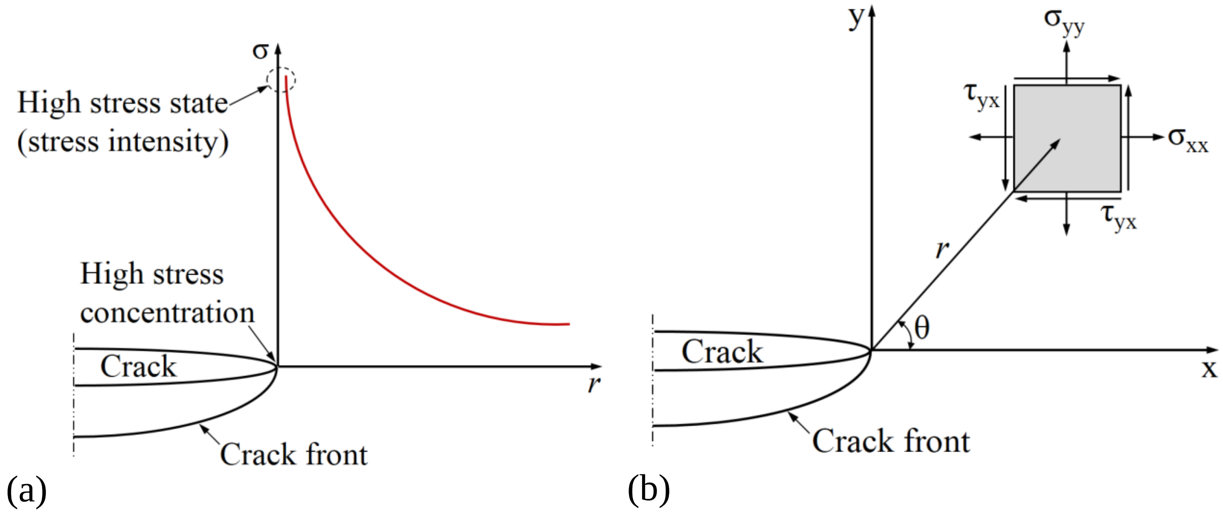

Fig. 1.2 Stress near the crack front in an elastic material. (a) stress singularity at the crack front, (b) stressed element near the crack front under combined loading with the in-plane stresses on this element (note that: z-direction is normal to the page).

$$\sigma_{xx} = \frac{K_I}{\sqrt{2\pi r}} cos\left(\frac{\theta}{2}\right)\left[1 - sin\left(\frac{\theta}{2}\right) sin\left(\frac{3\theta}{2}\right)\right] \tag{1.1}$$

$$\sigma_{yy} = \frac{K_I}{\sqrt{2\pi r}} cos\left(\frac{\theta}{2}\right)\left[1 + sin\left(\frac{\theta}{2}\right) sin\left(\frac{3\theta}{2}\right)\right] \tag{1.2}$$

$$\tau_{xy} = \frac{K_I}{\sqrt{2\pi r}} cos\left(\frac{\theta}{2}\right) sin\left(\frac{\theta}{2}\right) cos\left(\frac{3\theta}{2}\right) \tag{1.3}$$

$$\sigma_{zz} = \begin{cases} 0 & (plane\ stress) \\ \nu(\sigma_{xx} + \sigma_{yy}) & (plane\ strain) \end{cases} \tag{1.4}$$

$$\tau_{xz}, \tau_{yz} = 0 \tag{1.5}$$

where ν represents Poisson's ratio. When $\theta = 0$, the shear stress is zero, which means that a pure mode-I loading is produced. Based on that and according equations 1.1–1.5, the stresses in x- and y-directions are equal and given as[14]:

$$\sigma_{xx} = \sigma_{yy} = \frac{K_I}{\sqrt{2\pi r}} \tag{1.6}$$

From equations 1.1–1.5, it is clear that each stress component is proportional to a single constant (K_I). The whole stress distribution at the crack front can be calculated with equations 1.1–1.5 if this single constant K_I is known. This constant fully describes the crack front conditions in a linear elastic material. For a flat plate with a through-thickness crack, see Fig. 1.3, the SIF (K_I) is defined as[14]:

$$K_I = \sigma\sqrt{\pi a} \tag{1.7}$$

where a is the crack half-length.

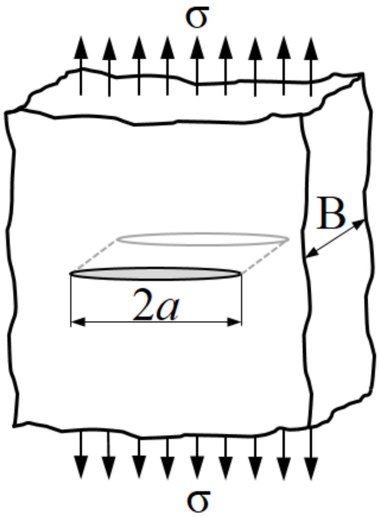

Fig. 1.3 Through-thickness crack in an infinite body subject to a remote tensile stress.

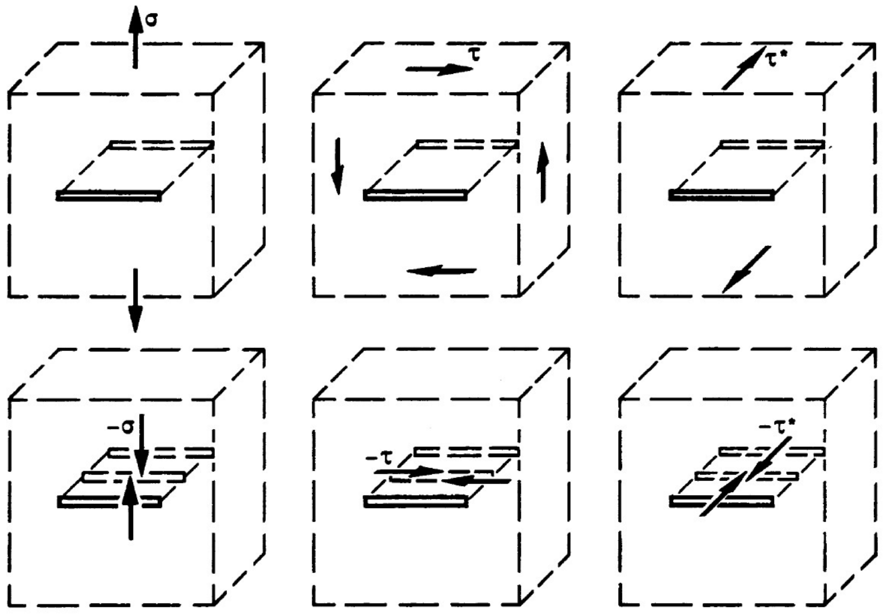

(a) (b) (c)

Fig. 1.4 Basic singular loading modes of cracks. (a) mode-I, (b) mode-II, (c) mode-III. Note that arrows denote remote boundary or crack flank stresses[16].

The local 3-D stress field at a particular point of the crack front may be separated into 2-D stress fields that are superimposed, namely, three loading modes with singular stresses and three loading modes with non-singular stresses. The singular loading modes include transverse tensile loading (mode-I), in-plane shear loading (mode-II) and out-of-plane shear loading (mode-III), see Fig. 1.4. The non-singular loading modes comprise crack-parallel tensile or compressive loading (mode 0I), crack-front-parallel tensile or compressive loading (0II) and crack-front shear loading (mode 0III), see Fig. 1.5[15]. The three singular loading modes: mode-I, mode-II and mode-III represented by K_I, K_{II} and K_{III}, respectively. The mode-related SIFs K_I, K_{II} and K_{III}depend on the magnitude of the applied load, the crack length and the geometry of the considered configuration.

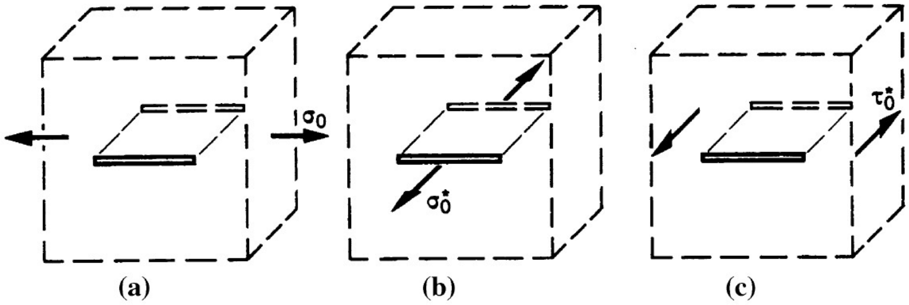

Fig. 1.5 Basic non-singular loading modes of cracks. (a) mode 0I, (b) mode 0II, (c) mode 0III. Note that arrows denote remote boundary stresses[16].

The SIF cannot only characterize the stress distribution at the crack front by computing the stress components, but also can play a significant role in evaluating the FCP rate. The FCP rate can be evaluated using the S-N curve technique[17] or using the fracture mechanics approach[14]. The key parameter for evaluating FCP rate based on the fracture mechanics approach is the SIF. Therefore for a reliable prediction of FCP rate as well as fracture strength, accurate SIF solutions along the crack front are needed for cracked components[18][19][20][21]. For welded structures, surface cracks frequently initiate at complicated RS fields. Based on that, in real situation, a complex welding RS field will arise over the crack face. It is therefore needed to improve the accuracy of the calculated SIF solutions by taking the influence of RS into account. Based on that, a powerful tool is needed to consider RS in SIF solutions.

1.3 The principle of superposition

According to the linear elastic fracture mechanics approach, the principle of superposition is considered an efficient tool for cracks in RS fields and for crack cohesive force models. The concept of the superposition principle is based on that remote loading and crack face traction (CFT), that equals to the negative of the stress acting on the crack face when the body is uncracked, applied to a cracked body result in the same SIF using the same displacement boundary conditions[14]. In other words, stresses acting on the boundary of a cracked body can be replaced with traction forces that act over the crack face, where the two loading configurations result in the same SIF solutions. The superposition method can be used to evaluate SIF for a crack in a complex stress field, by dividing the complex loading configuration into simple cases[11]. The superposition method is only used for adding SIF (*K*-value) for the same loading mode conditions, i.e. mode-I, mode-II or mode-III[14], as well as this method can only be applied for models with the same displacement boundary conditions.

The superposition method for a semi-elliptical surface cracked body subjected to a uniform remote loading system is shown in Fig. 1.6. Based on the principle of superposition, the stress intensity factor, SIF ($K_I^{(a)}$) for the cracked body subjected to remote loading condition, σ, (Fig. 1.6(a)) equals to that ($K_I^{(c)}$) for the cracked body subjected to loading, σ, over the crack face (Fig. 1.6(c)). The SIF ($K_I^{(b)}$) for the body loaded with the remote loading condition (σ) and the crack faces closing loading (−σ) in Fig. 1.6(b) equals zero (i.e. $K_I^{(b)} = 0$), because the crack faces are closed and the body behaves as if there is no crack under such conditions, i.e. uncracked body[14].

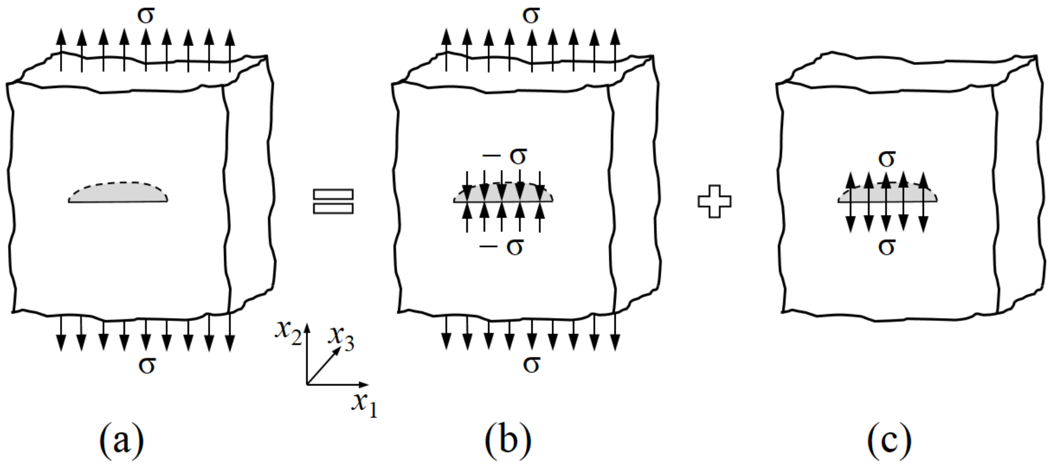

Fig. 1.6 The principle of superposition. (a) a cracked body subjected to a remote tensile loading σ, (b) a geometrically identical uncracked body with the stress field (−σ) in the crack plane produced by the loading system σ, (c) a geometrically identical cracked body with a crack subjected to the stress field (σ).

To validate the solution for each step of the superposition method (see Fig. 1.6), the total strain energy (U) for the solutions should satisfy Eq. 1.8. In addition, the crack mouth opening displacement ($CMOD$) of the remote loading solution and that obtained by CFT should satisfy Eq. 1.9. The subscripts (a), (b) and (c) in Eqns. 1.8 and 1.9 represent the three cases shown in Fig. 1.6.

$$U_{(a)} = U_{(b)} + U_{(c)} \tag{1.8}$$

$$CMOD_{(a)} = CMOD_{(c)} \tag{1.9}$$

For surface cracks exist in welding RS fields (i.e. nonlinear stress fields), the superposition method can be adopted to obtain accurate SIF solutions. However, in case of simple crack problems, they are usually analyzed by applying remote loading configurations. When analyzing a crack in a RS field, the influence of the stress field can be considered by applying the RS as traction forces over the crack face. The value of traction forces represent the negative of the stress field[22].

1.4 Faced problems and challenges

As mentioned before, in order to improve the accuracy of the SIF for fatigue cracks in welded joints the influence of welding RS must be included in the SIF solutions. So that, an important term in the SIF calculation methods called the crack face traction integral ‘CFT-integral’ should be implemented in the applied numerical integration method. This integral is needed when traction forces (i.e. stress fields) are applied to the crack face. However, most of the available commercial FE packages do not offer this integral in the implemented numerical integration methods. On the other hand, an open source code called WARP3D implements the CFT-integral in its numerical integration methods; however, the CFT-integral that implemented in WARP3D is only available for analyzing cracks that bear uniform distributed stress field over its surfaces. This means that WARP3D in its current version is available for analyzing cracks in simple geometries that offer uniform stress field over the crack face. However, in real situation, cracks initiate at complicated locations of welded structural components (i.e. complicated geometries). As well, these welded structures, in most cases, subject to complex external loading conditions. This leads to a complex RS field (i.e. non-uniform RS) to arise over the crack face. However, the WARP3D code in the current version is limited only for simple geometries and cannot be employed for such complex problems. Based on that, an efficient tool is needed to analyze surface cracks in non-uniform RS field in which the influence of this complex RS field can be taken into account when calculating SIF.

On the other hand, some literatures simplify the applied RS field when calculating the SIF. Simplification of RS may not give accurate and realistic behavior of the calculated SIF. The most appropriate way to obtain accurate and realistic SIF solution resulting from non-uniform RS field is to consider the RS field as is (i.e. without simplification) such as RS introduced by experiments and simulations (e.g. welding RS). Based on that, a powerful technique is needed to consider the actual RS field when computing SIF.

To achieve this target, WARP3D code is the best option for two reasons: 1) WARP3D code offers the CFT-integral and 2) it implements the interaction integral method that provides extraction of mixed-modes SIFs. However to benefit from WARP3D code, this code must be modified to overcome the current challenges. Furthermore, a robust technique is needed to be established to analyze various cracked welded joints with high accuracy.

On the other hand, since this study focuses on the evaluation of SIF for fatigue cracks in welding RS fields. Therefore, RS fields should be applied to the crack face as traction forces. However, preparation of RS field as a traction force file takes long time and tedious. To overcome this challenge as well as to improve the accuracy of the prepared traction force file, a technique should be developed to map welding RS over the crack face.

1.5 Objectives and structure of this study

The main objective of this study is to develop a robust technique based on the interaction integral method to calculate the SIF in addition to mixed-mode SIFs accurately for fatigue cracks in welding RS fields. The proposed technique calculates SIFs with welding RS using the crack face traction force analysis. The proposed technique is applicable to a wide range of problems, for example, surface cracks in flat plates under different loading conditions, surface cracks in welded joints (e.g. butt-welded joints, T-butt welded joints, tubular welded joints, etc.) subject to various loading conditions. The proposed technique can also employ the 6-components (i.e. normal and shear components) of welding RS generated by real welding and simulations in the calculated SIFs solutions. The accuracy of the calculated SIFs using the proposed technique are verified with well-established reference solutions, therefore more accurate FCP analysis becomes possible. Furthermore, large-scale problems can be solved using the proposed technique in short time.

As well, another objective of this study is to develop a technique to map welding RS fields as traction forces over the crack face in short time and accurately.

Moreover, this study also discusses the influence of the change in welding heat input (HI) on the distribution of welding RS. As well, study the influence of the change of welding HI and welding RS on the behavior of SIF and FCP.

The structure of this study is as follows:

1) Chapter 1 gives a background on RS produced due to welding and their influence on the integrity of structures. As well, cracks, their types, and existence of cracks in a RS field are addressed. The concept of the SIF and the principle of superposition are also reviewed. This chapter also discusses the challenges, problems, objectives and outlook related to this study.

2) Chapter 2 addresses a background on the numerical methods that used in SIF evaluation for 3-D cracks. In addition, this chapter reviews the formulation of the domain integral method and the interaction integral method that form the basis of the numerical procedures used in this study.
3) Chapter 3 discusses the validation of the superposition method using different numerical integration methods and FE models. In this chapter, an automatic equivalent nodal load calculation system is presented as a step in the validation of the superposition method. In addition, an automatic crack mesh generation system is developed for generating a weld toe with curvature for a T-butt welded joint with surface crack. On the other hand, the effectiveness of including the CFT-integral in the applied numerical integration method on the accuracy of CFT-solutions is examined for surface cracks in flat plate models.
4) Chapter 4 introduces the methodology of a proposed technique that used for calculating SIF (K_I) in a non-uniform stress field as well as investigates the influence of the crack-block mesh density on the accuracy of the CFT-solutions. Furthermore, the significance of the CFT-integral in improving the accuracy of SIF solutions are also discussed. On the other hand, numerical examples of different welded joints under different loading conditions are examined to demonstrate the adequacy of the proposed technique. As well, SIF solutions are evaluated for a surface crack in a butt-welded joint based on real welding RS due to conventional and low transformation temperature (LTT) welds. The influence of simplifying welding RS on the calculated SIF is also discussed.
5) Chapter 5 conducts a comprehensive validation study based on the proposed technique that discussed in chapter 4. This chapter investigates the influence of the change in welding HI on welding simulation results and the behavior of SIF and FCP for a bead-on-plate model. Different welding HI cases as well as additional case without welding are employed. To simulate the welding process, a thermal-elastic-plastic (TEP) finite element analysis (FEA) is firstly conducted. The proposed technique is thereafter employed to calculate SIF solutions considering welding RS resulting from the applied welding HI cases under different constant stress amplitude loadings. The fatigue lives are then evaluated based on the calculated SIF solutions and validated with experiments. Moreover, this chapter presents a fundamental study that investigates the influence of the change in RS on the behavior of SIF and FCP.

6) Chapter 6 presents a developed code based on WARP3D-IIM that can be used for computing mixed-mode SIFs (K_I, K_{II} and K_{III}) for fatigue cracks in non-uniform stress fields with high accuracy. A numerical FE examples with an inclined penny crack embedded in an infinite body are used to validate the developed code based on analytical solutions and the superposition method.
7) Chapter 7 summarizes the conclusions of the main points in this study. This chapter also discusses further works that may improve the effectiveness and adequacy of the proposed technique.

CHAPTER 2

Theoretical background on SIFs evaluation methods

2.1 Background

Different methods, nowadays, are employed for calculating SIFs. For instance, the weight function method[14][18] and finite element method (FEM) are widely utilized in computing SIFs. Although the weight function method can be used for calculating SIF resulting from RS; however, most weight functions were developed for simple geometries or require some correction. As well, some weight functions have very complicated forms that make the calculation process complex due to the complex integral equations involved in these functions[18]. On the other hand, the FEM is more powerful tool for complicated geometries and loading conditions as well as it is effective for computing linear and nonlinear fracture mechanics parameters. For linear analyses, SIF (K_I) is calculated from the energy release rate based on the J-integral[23][24][25]. For nonlinear analyses, the deformation intensity along the crack front is determined by the crack tip opening displacement (CTOD) and/or a pointwise value of the J-integral[26]. FEM has been successfully employed in fracture analysis for welded joints[27][28][29]. Due to the rapid development of computers as well as the implementation of fracture mechanics analysis routines in the commercial FE codes, this method is getting more robust and popular. One of the most important factors that make the FEM is more powerful than weight function method in evaluating the influence of RS on SIF is that FEM is considered effective tool for analyzing complicated welded components[18].

There are different methods available for evaluating the SIF by FEM, for example, the J-integral method, the interaction integral method (IIM), the virtual crack closure method (VCCM) and the crack tip displacements extrapolation method. The J-integral, VCCM and displacement extrapolation methods are widely employed in the commercial FE packages. On the other hand, the IIM is used for extracting the mixed-mode SIFs that is suitable for calculating SIFs resulting from welding RS for complicated welded structural components. In this research, the domain integral (DI) and the IIM that are based on the J-integral were employed where they have been widely used for evaluating SIFs. The following sections will give more details on the DI and IIM.

2.2 The domain integral for 3-D cracks with surface tractions

The DI method was employed for calculating the J-integral[23], and has been considered a powerful numerical method for its path-independence in homogenous materials. This method is highly versatile where it can be applied to both quasistatic and dynamic problems with elastic, plastic, or viscoplastic material response, in addition to thermal loading. Furthermore, the DI formulation is very effective and relatively simple to implement numerically[14]. Using the DI method, a crack front contour integral is expressed as a domain/volume integral over a finite domain surrounding the crack front[30]. Shih et al.[31][32] developed a domain integral expression to estimate the J-integral along a 3-D crack front that includes a surface integral for a crack face that bears traction forces. Further, Moran and Shih[33] derived the crack tip flux integrals (i.e. J-integral) and their associated domain representations from momentum and energy balance. The general formula of the J-integral requires that the contour surrounding the crack front be very small[14].

Dodds and Vargas[34] developed computational procedures for non-vanishing, finite-sized contours in order to evaluate the J-integral numerically in the context of FEA. Their developments have proceeded along two lines with the corresponding introduction of 'Domain Integral' (integrals over element volumes) and 'Contour Integral' (line integrals and area integrals) methods. Moreover, Nikishkov and Atluri[35] introduced an equivalent DI method with numerical algorithms to calculate fracture mechanics parameters for an arbitrary 3-D crack. Kumar and Raju[36], as well, developed a general formulation of the equivalent DI method for 3-D mixed-mode fracture problems in cracked solids.

The J-integral at location s (see Fig. 2.1) along a 3-D crack front has the general formula[31]:

$$J(s) = \lim_{\Gamma\to 0}\int_{\Gamma} \left(W\delta_{1i} - \sigma_{ij}u_{j,1}\right)n_i d\Gamma \tag{2.1}$$

where W is strain energy density, δ_{ij} denotes the Kronecker delta, σ_{ij} is stress components, and u_j represents displacement components. The contour Γ, with normal vector components n_i, exists in X_1–X_2 plane in the local coordinate system, and it starts from the lower crack face and ends at the upper crack face as shown in Fig. 2.1.

Shih et al.[31] formulated Eq. 2.1 into two main parts: 1) volume integral and 2) surface integral; to be suitable for numerical analysis in case of 3-D cracks. They formulated the energy relaesed per unit advance of crack front segement L_C, $\bar{J}(s)$, as follows:

$$\bar{J}(s) = \int_{V} \left(\sigma_{ij}u_{j,1} - W\delta_{1i}\right) q_{,i} dV + \int_{V} \left(\sigma_{ij}u_{j,1} - W\delta_{1i}\right)_{,i} q dV - \int_{S^{+}+S^{-}} t_{j}u_{j,1} q dS \qquad (2.2)$$

where t_j are crack face traction components. Surfaces $S^{+}, S^{-}, S_1, S_2, S_3$ and S_4 (see Fig. 2.1) form volume V, and surface S_2 shrinks to the crack front (i.e. $r \rightarrow 0$). The weight function q, varies smoothly within volume V. Equation 2.2 requires that $q = 0$ at S_1, S_3 and S_4 and equals 1.0 at location s on S_2[31], see Fig. 2.2. On the other hand, the third integral in Eq. 2.2, $\int_{S^{+}+S^{-}} t_{j}u_{j,1} q dS$, represents the CFT-integral.

The second and third integrals in Eq. 2.2 are ignored for elastic, homogenous materials under quasistatic, isothermal loading in case of body forces, thermal strain, and crack face traction are absent in which Eq. 2.2 gives the identical (volume) domain integral expressions for J[31][37]. The third integral, i.e. the CFT-integral, is omitted in most commercial nonlinear FE codes (e.g. MSC Marc).

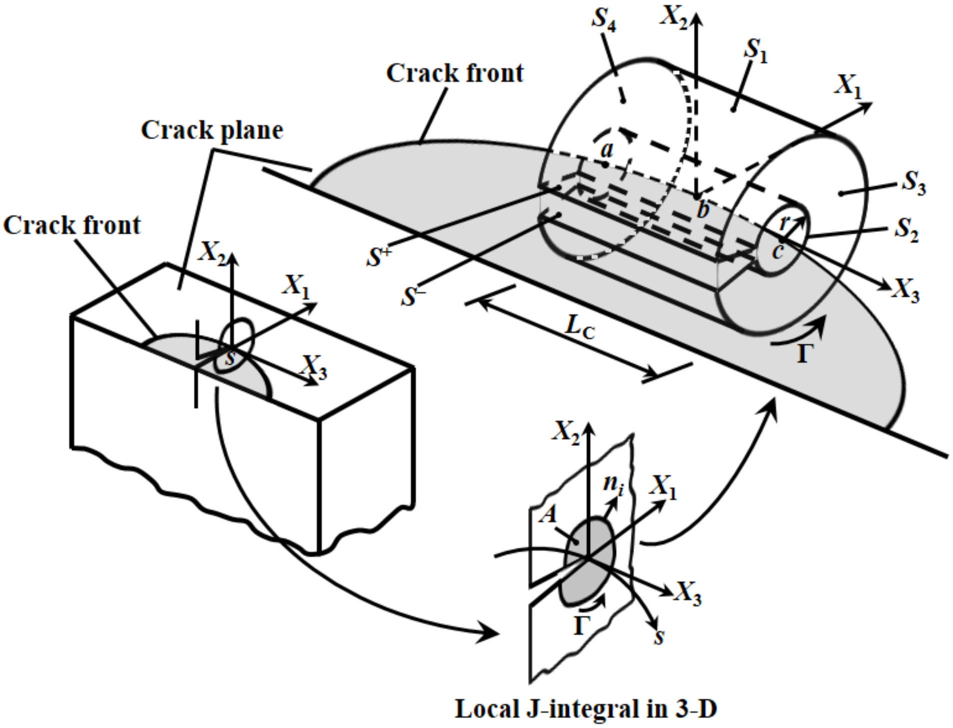

Fig. 2.1 Finite volume for use in DI formulation at crack front location s that extends over the length L_C.

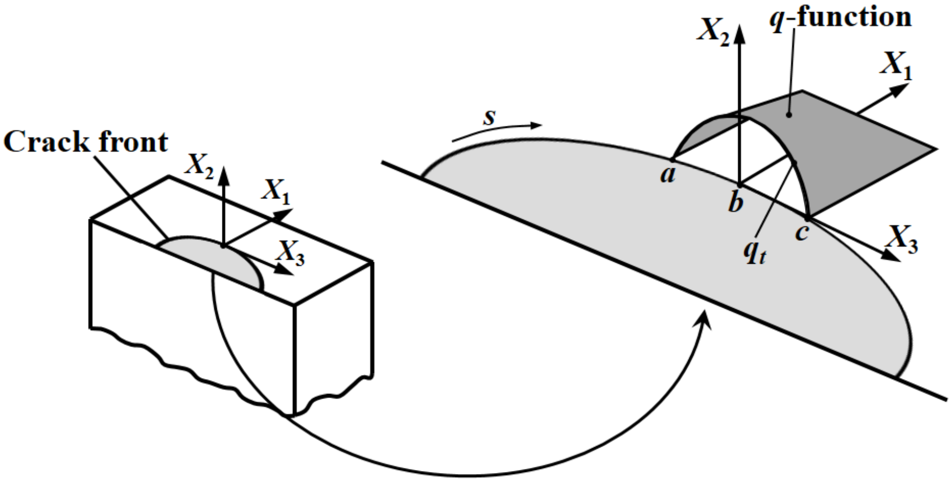

Fig. 2.2 Variation of weight function, q, over volume at crack front.

Shih et al.[31] derived the approximate formula of the J-integral by assuming that the energy release rate varies slowly over L_C:

$$J(s) = \frac{\bar{J}(s)}{\int_{L_C} q(s)ds} \tag{2.3}$$

The SIFs are valid only for linear-elastic analyses, and assume pure mode-I, mode-II or mode-III loading conditions. The SIFs for the three mode conditions (K_I, K_{II} or K_{III}) can be calculated using the J-integral, $J(s)$, in Eq. 2.3 as follows[26]:

$$K_I = \sqrt{J(s)E^*},\ K_{II} = \sqrt{J(s)E^*} \text{ and } K_{III} = \sqrt{\frac{J(s)E}{(1+\nu)}} \tag{2.4}$$

where $E^* = E$ for plane stress condition (i.e. SIF at the crack mouth) and $E^* = E/(1-\nu^2)$ for plane strain condition (i.e. SIF at the element corner nodes at the crack front except at the crack mouth. As well, E represents Young's modulus and ν denotes Poisson's ratio. For more details on the DI method, refer to Refs.[26][31].

2.3 The interaction integral method for 3-D cracks with surface tractions

Recently, the IIM has emerged an accurate and powerful approach to evaluate the SIFs in mixed-mode fracture mechanics problems. To extract the mixed-mode SIFs, an interaction energy integral method[38][39] was derived based on the DI method by combining two admissible states (the actual fields and known auxiliary fields). Yau et al.[39] initially developed an IIM to solve 2-D mixed-mode crack problem in an isotropic homogenous material. Wang et al.[40] adopted this method to conduct the SIF evaluations of anistropic material. Then, Nakamura and Parks[41] extended the IIM to 3-D problems. The DI approach was thereafter applied to calculate the mixed-mode SIFs by Nikishkov and Atluri[35], Shivakumar and Raju[36] and Raju and Shivakumar[42]. The IIM, thereafter, was develobed by Matos et al.[43] to extract the components of the comples SIFs (K_I and K_{II}). Nakamura[44] applied this method to calculate the mixed-mode SIFs along straight, three-dimensional interface cracks. Gosz and his coworkers[44][45], then, developed an IIM to extract the mixed-mode SIFs along planar interface cracks and non-planar crack tips in 3-Ds. Walters et al.[37] developed an interaction integral procedures for 3-D curved cracks that include crack face tractions. The IIM has emerged a robust method and the most accurate and readily approach to calculate mixed-mode SIFs[37].

The IIM has been employed for evaluating the fracture parameters in a wide range of appliactions as well as for different materials. Qian et al.[46] calculated the mixed-mode SIFs for tubular K-joints with weld toe cracks. Rao and Rahman[47] developed an interaction integral method for analysis of cracks in orthotropic functionally graded matrials. Kim and Paulino[48][49][50] developed approaches and formulations based on the IIM for evaluating the mixed-mode SIFs, T-stresses and crack initiation angle in functionally graded matrials. Further, Johnson and Qu[51] provided an IIM for computing mixed-mode SIFs for curved bimaterials interface cracks in non-uniform temperature fields. In addition, the IIM was employed for evaluating the mixed-mode SIFs for complex interfacial fracture problems of nonhomogenous materials[52][53][54]. Furthermore, Daimon and Okada[55] evaluated the mixed-mode SIFs by the IIM for quadratic tetrahedral FE with correction terms. Moreover, the IIM with the DI approach was employed for problems of cracks in anistropic material and of interface cracks. Further, Sukumar et al.[56] and Moes et al.[57] adopted the IIM and the DI method to compute the J-integral and the SIFs by the X-FEM.

The IIM provides two solutions. The first one gives actual fields (e.g. displacement, stress, and strain) of an equilibrium state for a boundary value problem. The other solution provides auxiliary fields that include desired quantities, such as, SIFs or T-stresses[49][58] by another selected equilibrium state. A linear combination of actual equilibrium fields with auxiliary fields forms a third equilibrium state called superimposed state. The calculation of the J-integral for this superimposed state leads to a conservation integral, composed of interacting actual and auxiliary terms, that permits direct calculation of SIF[26]. The energy released per unit advance of crack segment for the superimposed state, $\bar{J}^S$, is calculated as follows[37]:

$$\begin{aligned}\bar{J}^S(s) = &\int_V \left[\left(\sigma_{ij} + \sigma_{ij}^{aux}\right)\left(u_{j,1} + u_{j,1}^{aux}\right) - W^S\delta_{1i}\right] q_{,i} dV \\ &+ \int_V \left[\left(\sigma_{ij} + \sigma_{ij}^{aux}\right)\left(u_{j,1} + u_{j,1}^{aux}\right) - W^S\delta_{1i}\right]_{,i} q dV \\ &- \int_{S^+ + S^-} \left(t_j + t_j^{aux}\right)\left(u_{j,1} + u_{j,1}^{aux}\right) q dS\end{aligned} \tag{2.5}$$

The superscript 'S' represents the superimposed state. For linear-elastic material, the strain energy density for the superimposed state, W^S, is[37]:

$$W^S = \frac{1}{2}\left(\sigma_{ij} + \sigma_{ij}^{aux}\right)\left(\varepsilon_{ij} + \varepsilon_{ij}^{aux}\right) = W + W^{aux} + W^I \tag{2.6}$$

where W is the strain energy density for the actual state, W^{aux} denotes the strain energy density for the auxiliary state and W^I represents the strain energy density for the interaction integral that is given by[37]:

$$W^I = \frac{1}{2}\left(\sigma_{ij}\varepsilon_{ij}^{aux} + \sigma_{ij}^{aux}\varepsilon_{ij}\right) \tag{2.7}$$

The $\bar{J}^S$ is divided into three terms as[37]:

$$\bar{J}^S(s) = \bar{J}(s) + \bar{J}^{aux}(s) + \bar{I}(s) \tag{2.8}$$

where $\bar{J}(s)$ represents the DI for the actual state and equals Eq. 2.2; $\bar{J}^{aux}(s)$, is the DI for the auxiliary state; and $\bar{I}(s)$ is an integral with interacting actual and auxiliary term, defined as[37]:

$$\bar{I}^S(s) = \int_V \left[\sigma_{ij}u_{j,1}^{aux} + \sigma_{ij}^{aux}u_{j,1} - \frac{1}{2}\left(\sigma_{jk}\varepsilon_{jk}^{aux} + \sigma_{jk}^{aux}\varepsilon_{jk}\right)\delta_{1i}\right]q_{,i}dV$$
$$+ \int_V \left[\sigma_{ij}u_{j,1}^{aux} + \sigma_{ij}^{aux}u_{j,1} - \frac{1}{2}\left(\sigma_{jk}\varepsilon_{jk}^{aux} + \sigma_{jk}^{aux}\varepsilon_{jk}\right)\delta_{1i}\right]_{,i} qdV \qquad (2.9)$$
$$- \int_{S^+ + S^-} \left(t_j u_{j,1}^{aux} + t_j^{aux}u_{j,1}\right)qdS$$

For straight cracks, the second integral in Eq. 2.9 vanishes for quasistatic, isothermal loading of homogenous materials in the absence of body forces. The third integral also vanishes for crack faces without traction forces[37].

The IIM developed by Walters et al.[37] assumed that the same constitutive tensor, C_{ijkl}, couples actual and auxiliary stress and strain components as following:

$$\sigma_{ij} = C_{ijkl}\varepsilon_{kl} \text{ and } \sigma_{ij}^{aux} = C_{ijkl}\varepsilon_{kl}^{aux} \qquad (2.10)$$

The constitutive tensor becomes the same for the 3-D actual fields and for the 2-D auxiliary fields by preparing appropriate definitions of auxiliary strain components. Thus, useful relationships can be obtained based on Eq. 2.10, as follows[37]:

$$\sigma_{ij}\varepsilon_{ij}^{aux} = C_{ijkl}\varepsilon_{kl}\varepsilon_{ij}^{aux} = C_{klij}\varepsilon_{ij}^{aux}\varepsilon_{kl} = \sigma_{ij}^{aux}\varepsilon_{ij} \qquad (2.11)$$

Equation 2.11 enables simplification of the stress-strain terms in the first and second integrals of Eq. 2.9. Furthermore, Eq. 2.11 leads to the cancellation of two additional terms[37]:

$$\begin{aligned}\sigma_{ij}^{aux}u_{j,1i} - \sigma_{ij,1}\varepsilon_{ij}^{aux} &= \sigma_{ij}^{aux}u_{j,1i} - C_{ijkl,1}\varepsilon_{kl}\varepsilon_{ij}^{aux} + C_{ijkl}\varepsilon_{kl,1}\varepsilon_{ij}^{aux} \\ &= \sigma_{ij}^{aux}u_{j,1i} - C_{klij}\varepsilon_{ij}^{aux}\varepsilon_{kl,1} = \sigma_{ij}^{aux}u_{j,1i} - \sigma_{ij}^{aux}\varepsilon_{ij,1} = 0\end{aligned} \qquad (2.12)$$

It was observed by Nahta and Moran[59] that the 2-D plane-strain auxiliary fields given by Williams's solution[60] do not satisfy the equilibrium and compatibility of strain-displacement when defined in curvlinear coordinates. Based on that, Walters et al. defined the following relationships[37]:

$$\sigma_{ij}\left(u_{j,1i}^{aux} - \varepsilon_{ij,1}^{aux}\right) \neq 0 \text{ and } \sigma_{ij,i}^{aux} \neq 0 \tag{2.13}$$

The third integral in Eq. 2.9 simplifies with the assumption that the auxiliary state has no applied tractions over the crack face, because the auxiliary fields correspond to an arbitrary specified equilibrium state. Based on the preceding arguments, Eq. 2.9 can be written in the following form[37]:

$$\begin{aligned}\bar{I}(s) = \int_V \left(\sigma_{ij}u_{j,1}^{aux} + \sigma_{ij}^{aux}u_{j,1} - \sigma_{jk}\varepsilon_{jk}^{aux}\delta_{1i}\right)q_{,i}dV \\ + \int_V \left[\sigma_{ij}\left(u_{j,1i}^{aux} - \varepsilon_{ij,1}^{aux}\right) + \sigma_{ij,1}^{aux}u_{j,1}\right]qdV - \int_{S^+ + S^-} t_j u_{j,1}^{aux} qdS\end{aligned} \tag{2.14}$$

where $\bar{I}(s)$ is the domain for the interaction integral. The third integral in Eq. 2.14, $\int_{S^+ + S^-} t_j u_{j,1}^{aux} qdS$, represents the CFT-integral. This integral has a significant contribution to the accuracy of the calculated SIFs. As for the other quantities in the CFT-integral, they do not rely on the finite element solution of the boundary value problem[37].

By calculating the value of $\bar{I}(s)$ from Eq. 2.14, the interaction integral calculation at location s (see Fig. 2.1) over a 3-D crack front follows Eq. 2.3 as[37]:

$$I(s) = \frac{\bar{I}(s)}{\int_{L_C} q(s)ds} \tag{2.15}$$

To extract the SIFs at crack front location s for the three modes, an expression for the energy release rate in terms of mixed-mode SIFs K_I, K_{II} and K_{III} is given[14]:

$$J(s) = \frac{K_I^2 + K_{II}^2}{E^*} + \frac{1+\nu}{E}K_{III}^2 \tag{2.16}$$

Equation 2.16 assumes self-similar crack growth. Where E^* conditions are defined previously for Eq. 2.4 and s refers to location of a node at crack front. In case of the superimposed state, Eq. 2.16 takes the form[37]:

$$J^S(s) = \frac{1}{E^*}[(K_I + K_I^{aux})^2 + (K_{II} + K_{II}^{aux})^2] + \frac{1+\nu}{E}(K_{III} + K_{III}^{aux})^2 \\ = J(s) + J^{aux}(s) + I(s) \tag{2.17}$$

where $I(s)$ defined as[37]:

$$I(s) = \frac{1}{E^*}(2K_I K_I^{aux} + 2K_{II}K_{II}^{aux}) + \frac{1+\nu}{E}(2K_{III}K_{III}^{aux}) \tag{2.18}$$

By selecting appropriate values for the auxiliary modes of SIFs (K_I^{aux}, K_{II}^{aux} and K_{III}^{aux}) in Eq. 2.18, relationships between K_I, K_{II}, K_{III} and $I(s)$ can be obtained[37]:

$$K_I = \frac{E^*}{2}I(s),\ K_{II} = \frac{E^*}{2}I(s),\ \text{and}\ K_{III} = \mu I(s) \tag{2.19}$$

where $\mu = E/2(1+\nu)$. The selection $K_I^{aux} = 1.0$, $K_{II}^{aux} = K_{III}^{aux} = 0.0$, the selection $K_{II}^{aux} = 1.0$, $K_I^{aux} = K_{III}^{aux} = 0.0$, and the selection $K_{III}^{aux} = 1.0$, $K_I^{aux} = K_{II}^{aux} = 0.0$ in Eq. 2.18 give the relationships in Eq. 2.19. To obtain K_I, K_{II} and K_{III} from Eq. 2.19, the value of $I(s)$ in Eq. 2.15 is applied. For more details on the IIM and the exact integration of the CFT-integral for elements incident on the crack front, refer to Refs.[26][37].

CHAPTER 3

Numerical validation of the superposition method

To evaluate the SIF accurately for surface cracks in welded structural components, the influence of welding RS must be included in the SIF solutions. An efficient tool is needed to consider welding RS in the computed SIF. The superposition method has emerged as a powerful tool that offers solutions of SIF due to the application of external loading configurations as well as traction forces over the crack face. One of the advantages of this method is that the solutions obtained by the crack face tractions (i.e. CFT-solution) can be validated with those calculated by external loading (see Fig. 1.6(a) and Fig. 1.6(c)). Therefore, the main goal of this chapter is to verify the superposition method for different FE models using different numerical integration methods. On the other hand, most of commercial nonlinear FE codes, such as MSC Marc solver, do not take the CFT-integral into account. Therefore, another objective of this chapter is to examine the significance of the CFT-integral on the accuracy of SIF obtained by different numerical integral methods using the crack face traction analysis force technique.

3.1 Numerical analysis procedures

3.1.1 Definition of FE models

In this study, the SIF (K_I) was evaluated for a surface cracked flat plate model and T-butt welded model. The surface cracked bodies used in this study are shown in Figs. 3.1 and 3.2. The cracked T-butt welded body (Fig. 3.2) consists of a one-sided weld with a radiused weld toe as used by Bowness and Lee[61]. Two cases were employed for each cracked body (Figs. 3.1 and 3.2) in order to examine the accuracy of the numerical solutions, i.e. the DI and IIM, for CFT cases based on the superposition method. The dimensions of surface cracks, crack aspect ratios, and crack depth ratios for each case are shown in Table 3.1, where *a* is the crack depth, *c* is the crack half-length, and *t* is the model thickness.

The FE models corresponding to Figs. 3.1 and 3.2 are shown in Figs. 3.3 and 3.4, respectively. Since the cracked bodies are symmetric about the longitudinal axis, one-half symmetric models were used in this study; for the flat plate and T-butt welded joint. The arrows in Figs. 3.3 and 3.4 show the applied boundary conditions to prevent the rigid body motion. The crack face FE mesh for the flat plate model and T-butt welded model is shown in Fig. 3.5. The flat plate model generated using FEAcrack software[62]. The T-butt welded model generated in two steps: 1) create the crack-block mesh using Zencrack software[63], and 2) generate the global model that consists of a flat plate with an attachment using Patran software. The crack-block mesh then tied to the global model using glue contact option that available in MSC Marc solver. For the T-butt welded model, a FORTRAN program was developed to automatically create the radiused-welded toe.

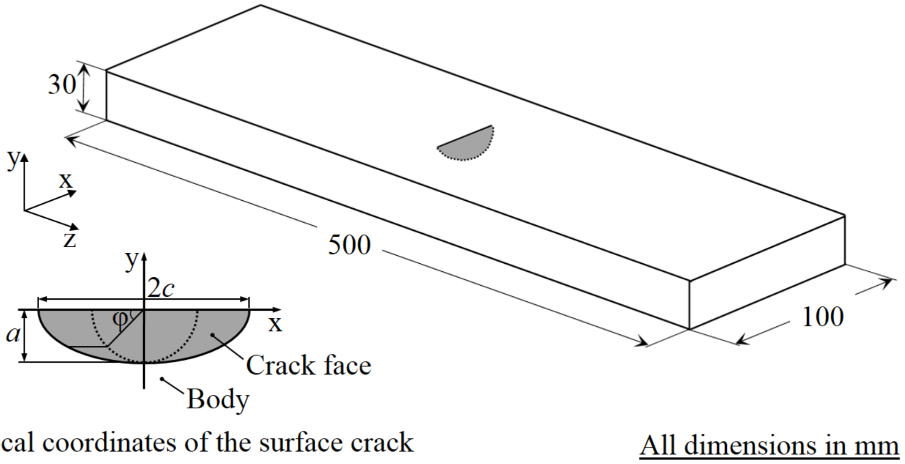

Fig. 3.1 Surface cracked flat plate body.

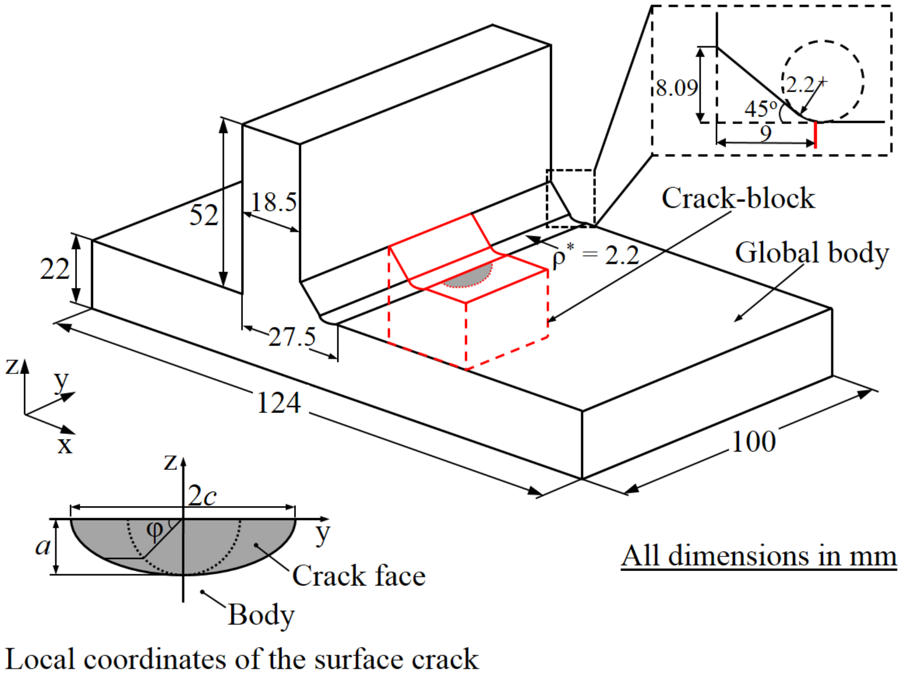

Fig. 3.2 Surface cracked T-butt welded body. (Note: ρ^* is the radius of weld toe).

Table 3.1 Crack dimensions and aspect ratios for the flat plate and T-butt welded FE models.

Model type	Analysis case	*a* (mm)	*c* (mm)	*a*/*c*	*a*/*t*
Flat plate	Case 1	3.6	6.1	0.59	0.12
	Case 2	5.8	12.6	0.46	0.19
T-butt joint	Case 1	2.0	2.0	1.00	0.09
	Case 2	4.0	4.0	1.00	0.18

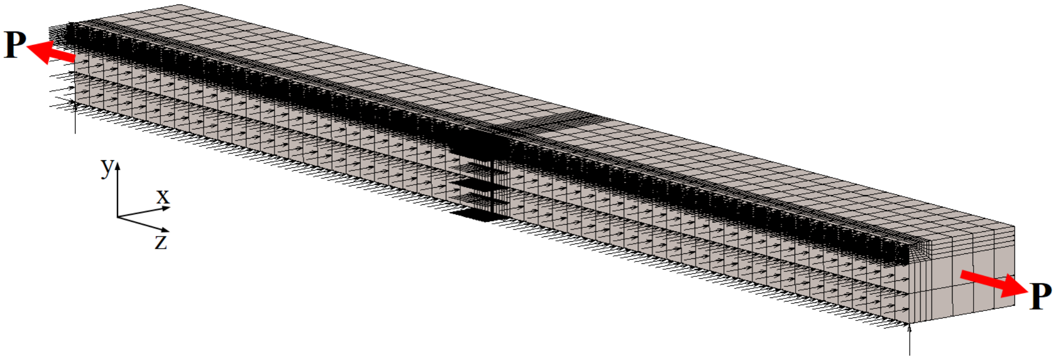

Fig. 3.3 Typical one-half symmetric FE mesh with boundary conditions of the flat plate.

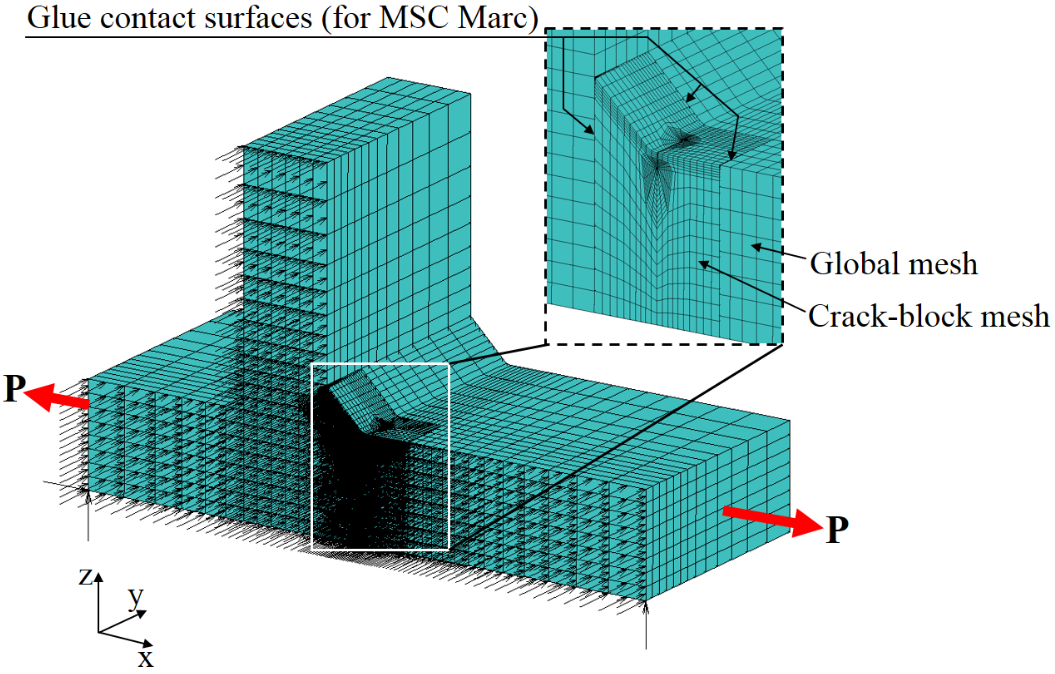

Fig. 3.4 Typical one-half symmetric FE mesh with boundary conditions of the T-butt welded joint.

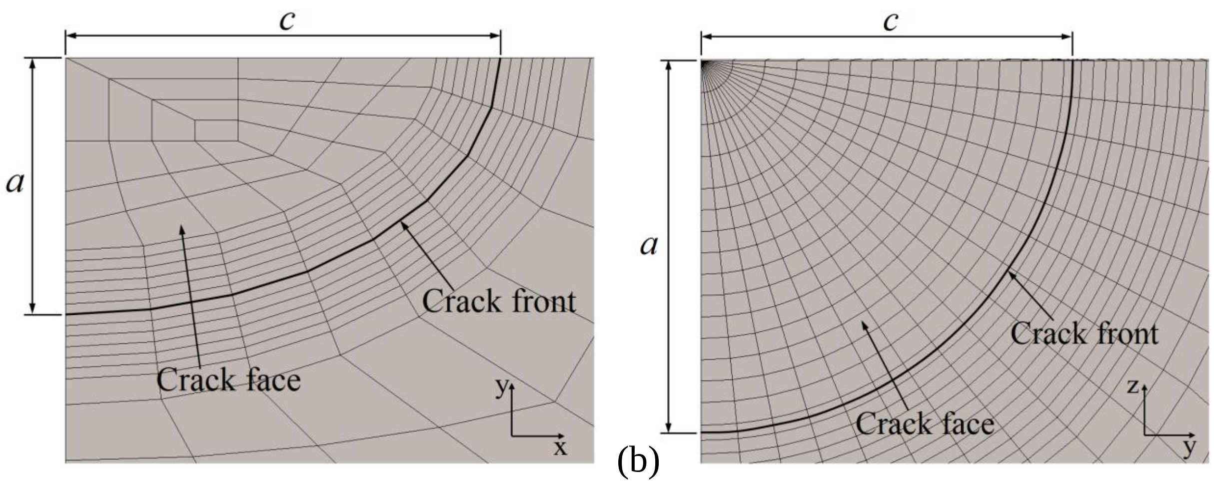

Fig. 3.5 Crack face FE mesh. (a) flat plate model and (b) T-butt welded model.

The FE mesh of the cracked models was generated using 20-noded isoparametric hexahedral brick elements. Along the crack front, the 20-noded hexahedral elements are collapsed to quarter-point wedge elements, which are used to simulate the $1/\sqrt{r}$ singularity of the stress field close to the crack front. The Young's modulus and Poisson's ratio used in the analyses are 210 GPa and 0.3, respectively. The rigid body motion of the FE models was prevented by applying the minimum displacement constraints, as shown in Figs. 3.3 and 3.4.

3.1.2 The superposition method procedures

In this study, the linear elastic fracture mechanics approach was performed. The cracked models, for the flat plate and T-butt welded joint, subjected to a uniaxial uniform remote tensile loading in the longitudinal direction. The superposition method was implemented through three steps (see Fig. 1.6):

1) calculation of SIF (K_I-value) by applying uniform external tensile loading (see Fig. 1.6(a)) to the cracked flat plate model and T-butt welded model. the calculated SIF solution in this step called "external loading solution",
2) stress field that arises over the crack face calculated by applying the same external tensile loading configuration to a geometrically identical uncracked model (Fig. 1.6(b)); and
3) calculated stress field in step 2 is applied as traction forces over the crack face with an opposite sign in order to calculate the SIF solutions (K_I-value) for a geometrically identical cracked model (Fig. 1.6(c)). The calculated SIF solution in this step called "CFT-solution".

To implement the superposition method, two solvers were utilized, a commercial nonlinear FE solver that progresses the DI method using MSC Marc and neglects the CFT-integral. The other is an open source research solver that progresses the IIM using WARP3D and includes the CFT-integral. The two solvers were applied to firstly verify the superposition method and thereafter to evaluate the accuracy of SIF solutions obtained by traction forces over the crack face. The SIF calculated by external loading solution, for the flat plate model and T-butt welded model, were validated through well-established results. The accuracy of the superposition method was verified by comparing the SIF solution obtained by CFT with those given by external loading solution. Further details on the procedures and results are given in the following sections. The structure of the applied numerical analyses is shown in Fig. 3.6.

In order to examine the significance and effectiveness of the CFT-integral (see Eqns. 2.2 and 2.14) on the accuracy of the SIF solutions obtained by CFT, this study is divided into two parts:

1) evaluation of SIF using face tractions without considering the CFT-integral; and
2) evaluation of SIF using face tractions with considering the CFT-integral.

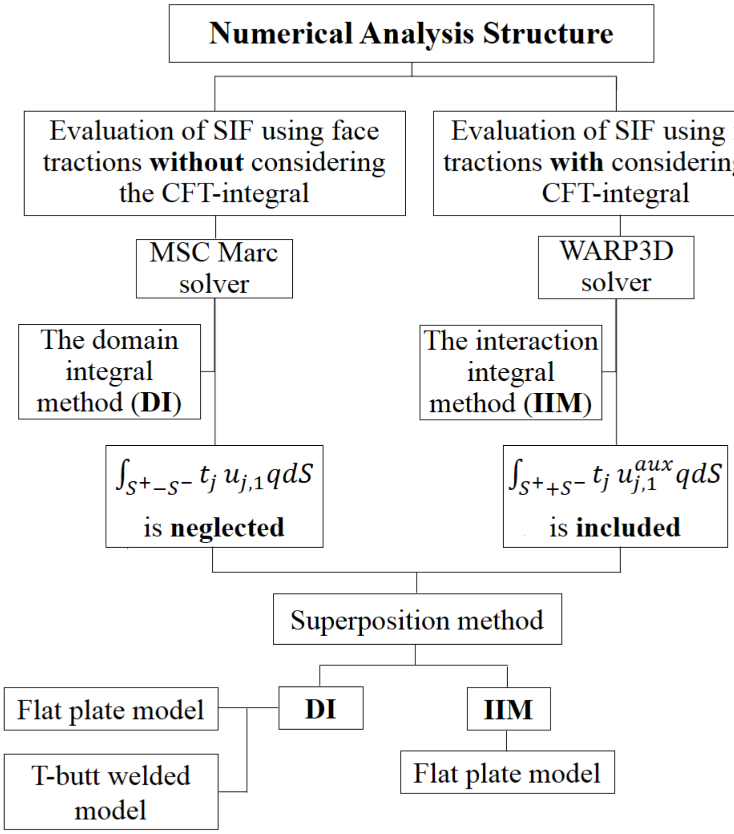

Fig. 3.6 Structure of the applied numerical analyses.

3.2 Evaluation of SIF using face tractions without considering the CFT-integral

In this section, the SIF was evaluated for surface cracks in a flat plate model and T-butt welded model using the superposition method. The SIF (K_I-value) evaluated based on the DI method employing the crack option of MSC Marc solver. As mentioned before, MSC Marc solver does not provide the CFT-integral in the DI solution. Therefore, the CFT-integral is neglected in the SIF solutions. The SIF calculated by external loading for the case of flat plate model was verified with the solutions given by Newman-Raju[64][65][66] for surface cracked plates subjected to uniform tension. For the case of T-butt welded model, the SIF solution that given by external loading was validated with different reference solutions. As mentioned section 1.3, the superposition method cannot be implemented for models with different displacement boundary conditions. Therefore, the three steps of the superposition method, mentioned in section 3.1.2 and shown in Fig. 1.6, performed using the same displacement boundary conditions.

3.2.1 Flat plate model

It is known for simple geometries, such as flat plates, when external tensile loading is applied to an uncracked flat plate model, a uniform distributed stress field will arise over the crack face. To apply the induced stress field as traction forces over the crack face, the stress field should be properly processed. In order to reduce the man-hours needed to prepare the equivalent nodal force for each node over the crack face, i.e. crack nodal traction (CNT), a FORTRAN program was developed to process the generated stress field and gives the required equivalent nodal forces over the crack face nodes. The processed stress field was then applied to the crack face nodes as CNT for the same cracked model that was used for external loading solution except with an opposite sign. The CNT tries to open the crack (Fig. 1.6(c)) as in the case of external tensile loading, which is applied to a cracked body (Fig. 1.6(a)). Based on that, the SIF solution (i.e. CNT-solution) was calculated by taking into account the influence of the stress field using MSC Marc DI method (i.e. MSC Marc-DI).

The accuracy of the numerical DI method for the CNT-cases was examined, by comparing the SIF solution obtained by CNT with those given by external loading. To validate the solution for each step of the superposition method (see Fig. 1.6), Eq. 1.8 that examines the total strain energy, U and Eq. 1.9 that examines the crack mouth opening displacement, $CMOD$ for the external loading solution and the CNT-solution should be satisfied. Where U is given in N.mm and $CMOD$ is given in mm. The solutions for the superposition method steps were verified for the flat plate cases through Tables 3.2 and 3.3; note that $w_1$and w_2 are the longitudinal displacements for two duplicate nodes on the crack faces.

Table 3.2 Validation of the solutions of the superposition method steps obtained by the DI method using the total strain energy, U and $CMOD$ for the flat plate model (case 1).

$U_{(a)}$	$U_{(b)}$	$U_{(c)}$	$U_{(b)} + U_{(c)}$	% difference between $U_{(a)}$ and $U_{(b)} + U_{(c)}$
1.79E+00	1.79E+00	3.33E-04	1.79E+00	0.0004
Case	w_1 (mm)	w_2 (mm)	$CMOD$	% difference between $CMOD_{(a)}$ and $CMOD_{(c)}$
Fig. 1.6(a)	1.16E-03	1.22E-03	6.74E-05	0.0027
Fig. 1.6(c)	-3.41E-05	3.33E-05	6.74E-05	

Table 3.3 Validation of the solutions of the superposition method steps obtained by the DI method using the total strain energy, U and $CMOD$ for the flat plate model (case 2).

$U_{(a)}$	$U_{(b)}$	$U_{(c)}$	$U_{(b)} + U_{(c)}$	% difference between $U_{(a)}$ and $U_{(b)} + U_{(c)}$
1.79E+00	1.79E+00	1.98E-03	1.79E+00	0.0003
Case	w_1 (mm)	w_2 (mm)	$CMOD$	% difference between $CMOD_{(a)}$ and $CMOD_{(c)}$
Fig. 1.6(a)	1.13E-03	1.25E-03	1.21E-04	0.0008
Fig. 1.6(c)	-6.24E-05	5.82E-05	1.21E-04	

The distribution of the normalized SIF solutions for mode-I (K_{In}) that calculated by the external loading and that obtained by CNT for the flat plate model is shown in Fig. 3.7. The external loading solutions were firstly verified with Newman-Raju solutions[64][65][66]. A good matching was obtained between the external loading solutions and those obtained by Newman-Raju. Note that, the crack mouth and the crack deepest point are represented at $2\varphi/\pi = 0$ and $2\varphi/\pi = 1$, respectively. The computed SIF is normalized based on a standard normalization formula for elliptical cracks as shown in Eq. 3.1[37].

$$K_{In} = \frac{K_I}{\sigma_o\sqrt{\pi a/Q}} \tag{3.1}$$

where σ_o is the external uniform tensile stress and $\sqrt{Q}$ is a complete elliptic integral of the second kind equal to $l/4c$, where l is the arc length of the ellipse. Most of the SIF solutions for elliptical and semi-elliptical cracks are written in terms of a flaw shape parameter Q that takes the following approximate expression, which for $a/c \leq 1$[14]:

$$Q = 1 + 1.464\left(\frac{a}{c}\right)^{1.65} \tag{3.2}$$

Moreover, good agreement was obtained between the external loading solution and that given by CNT as shown in Fig. 3.7. It is clear, from Fig. 3.7, that there is difference between the external loading solution and that computed by CNT. This difference is due to the absence of the CFT-integral in the applied DI method, where the CFT-integral in the CNT-solution is omitted from Eq. 2.2. The percentage difference between the SIF given by the external loading solution and that obtained by the CNT at the crack deepest point (at $2\varphi/\pi = 1$) is 4.4% for case 1 and 4.6% for case 2.

3.2.2 T-butt welded model

For the T-butt welded model, the two meshes (i.e. global mesh and crack-block mesh) were connected using the glue contact option that is offered by MSC Marc analysis code. The employed glue contact for the applied analyses does not have a significant influence on the calculated SIF. Due to the geometrical parameters of the T-butt welded model (e.g. weld bead shape), a non-uniform stress field is introduced over the crack face when an external tensile loading is applied to the uncracked model's boundaries. The evaluation of SIF using the CNT technique for the T-butt welded model follows the same procedures that utilized in case of the flat plate model (refer to section 3.2.1). In the same way, the total strain energies and the crack mouth opening displacements for the superposition method steps were verified based on Eqns. 1.8 and 1.9. Tables 3.4 and 3.5 show the validation of the solutions for the superposition method steps. Where u_1^* and u_2^* represent the longitudinal displacements for two duplicate nodes on the crack faces.

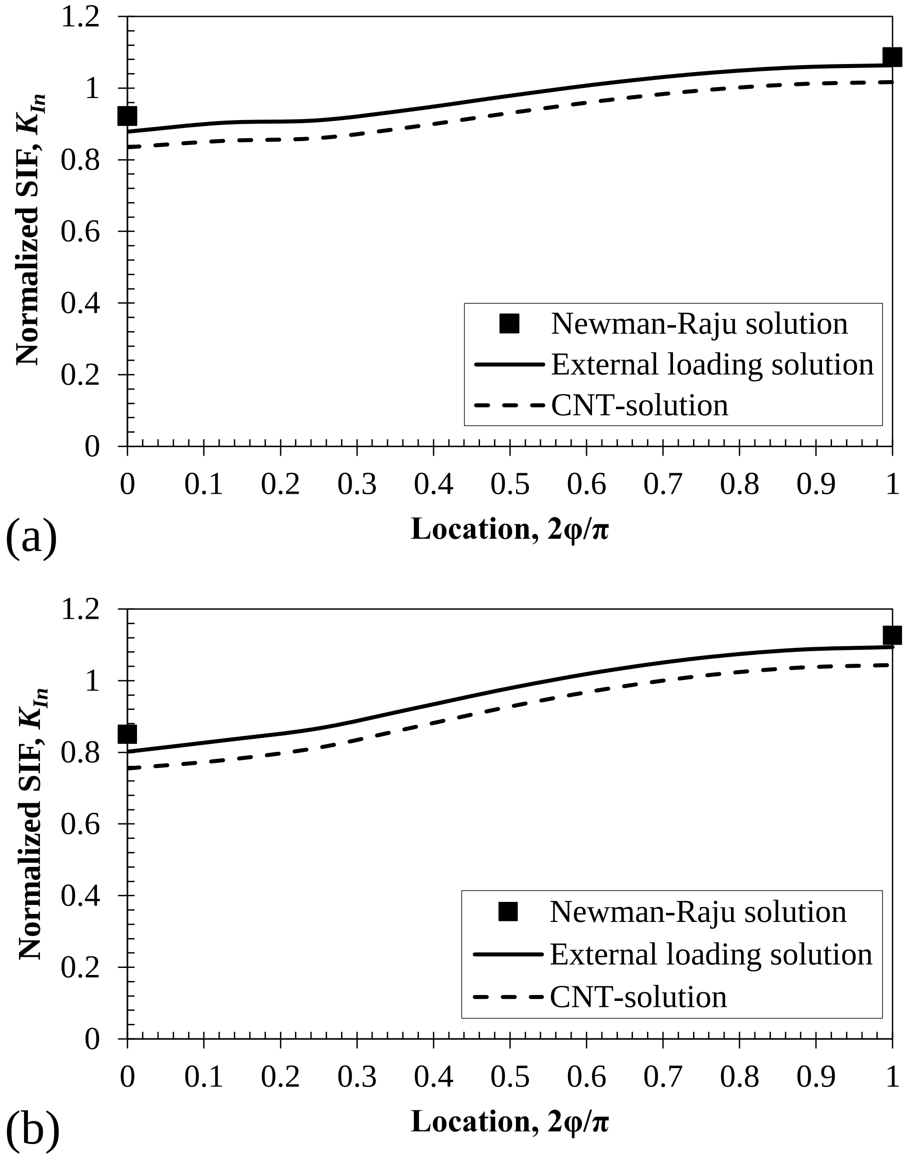

Fig. 3.7 Distribution of the normalized SIF (K_{In}) along the crack front given by the external loading and CNT for the flat plate model using MSC Marc-DI (CFT-integral is neglected). (a) case 1, and (b) case 2.

Table 3.4 Validation of the solutions of the superposition method steps obtained by the DI method using the total strain energy, U and $CMOD$ for the T-butt welded model (case 1).

$U_{(a)}$	$U_{(b)}$	$U_{(c)}$	$U_{(b)}+U_{(c)}$	% difference between $U_{(a)}$ and $U_{(b)}+U_{(c)}$
1.28E+04	1.28E+04	1.54E+00	1.28E+03	0.0003
Case	u_1^* (mm)	u_2^* (mm)	$CMOD$	% difference between $CMOD_{(a)}$ and $CMOD_{(c)}$
Fig. 1.6(a)	5.49E-02	6.15E-02	6.63E-03	1.953
Fig. 1.6(c)	-2.77E-03	4.00E-03	6.77E-03	

Table 3.5 Validation of the solutions of the superposition method steps obtained by the DI method using the total strain energy, U and $CMOD$ for the T-butt welded model (case 2).

$U_{(a)}$	$U_{(b)}$	$U_{(c)}$	$U_{(b)}+U_{(c)}$	% difference between $U_{(a)}$ and $U_{(b)}+U_{(c)}$
1.28E+04	1.28E+04	1.03E+01	1.28E+04	0.0049
Case	u_1^* (mm)	u_2^* (mm)	$CMOD$	% difference between $CMOD_{(a)}$ and $CMOD_{(c)}$
Fig. 1.6(a)	5.28E-02	6.43E-02	1.15E-02	0.2757
Fig. 1.6(c)	-4.91E-03	6.55E-03	1.15E-02	

The distribution of the normalized SIF solutions (K_{In}) given by the external loading and CNT for the T-butt welded model is shown in Fig. 3.8. The external loading solution was validated with two analytical solutions, namely, Bowness and Lee[61] and the British standard[67] as well as it was verified with that computed by Tanaka et al.[68]. An excellent agreement was achieved between the external loading solution and that given by Tanaka et al. along the crack front. On the other hand, the two analytical solutions gave very good agreement with the external loading solution at the crack deepest point (at $2\varphi/\pi = 1$). However, a clear difference in the calculated SIF was observed between the external loading solution and that given by Bowness and Lee[61] at the crack mouth (at $2\varphi/\pi = 0$). The reason of this difference may be due the restraining effect of the attachment that reduced the singularity from $r^{0.5}$ to about $r^{0.4}$[61]. However, in this study, the focus is given to the SIF at the crack deepest point in which the two analytical solutions gave a very good matching with the solution obtained by the external loading.

As discussed in the case of the flat plate model, a difference between the external loading solution and that obtained by CNT was observed for the two cases of the T-butt welded model.

The cause of this difference is again due to the omission of the CFT-integral in the applied DI method. Although the CFT-integral is not included in the CNT-solutions, the results in Fig. 3.8 show good matching between the CNT-solutions and those obtained by external loading. The percentage difference between the SIF obtained by the CNT and that given by the external loading at the crack deepest point (at $2\varphi/\pi = 1$) is 4.1% for case 1 and 4.3% for case 2.

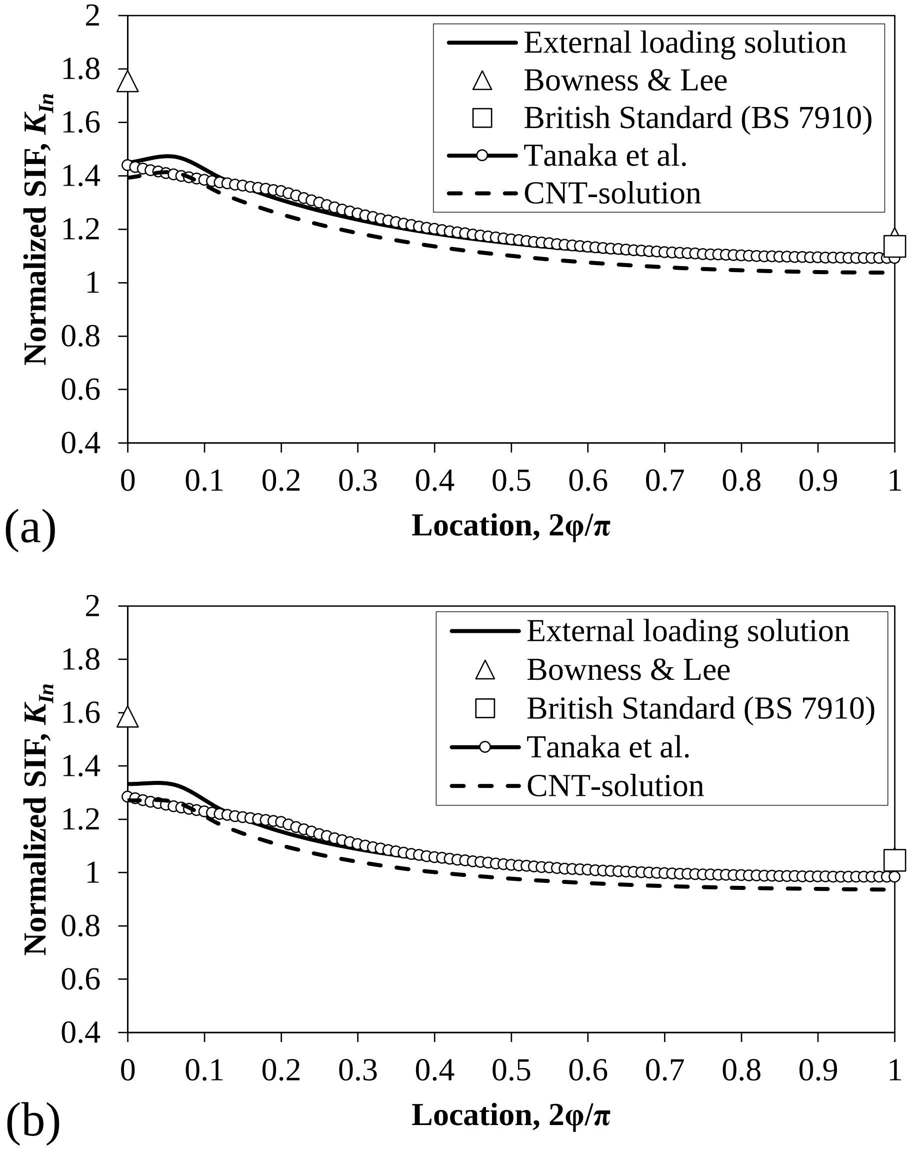

Fig. 3.8 Distribution of the normalized SIF (K_{In}) along the crack front given by the external loading and CNT for the T-butt welded model using MSC Marc-DI (CFT-integral is neglected). (a) case 1, and (b) case 2.

3.2.3 Discussion

As shown in Tables 3.2–3.5, the difference between the total strain energies (i.e. $U_{(a)}$ and $U_{(b)} + U_{(c)}$) and the difference between the crack mouth opening displacements (i.e. $CMOD_{(a)}$ and $CMOD_{(c)}$) for the solutions are negligible and satisfy Eqns. 1.8 and 1.9. This reveals the accuracy of the numerically implemented superposition method for each step (see Fig. 1.6).

On the other hand, it was observed that the solutions given by the CNT are underestimated compared to those given by the external loading as shown in Figs. 3.7 and 3.8. It is known that the CFT-integral is needed when considering crack nodal traction forces in the DI method[11][37]. However, although the CFT-integral is not included in the MSC Marc-DI method, the results obtained by the numerical analyses for the flat plate model and T-butt welded model gave reasonable accuracy when using the DI method available in the commercial FE code, MSC Marc. It was found that the difference between the two solutions (i.e. external loading solution and CNT-solution) of the flat plate model and T-butt welded model at the crack deepest point is less than 5%, even when the CFT-integral is not considered in the CNT-solutions. This shows that the commercial nonlinear FE codes that neglect the CFT-integral can be applied for rough estimation of SIF for surface cracks in stress fields for engineering problems under the conditions examined in this study.

3.3 Evaluation of SIF using face tractions with considering the CFT-integral

In this part, the SIF (K_I-value) was evaluated for surface cracks in the flat plate model using the superposition method in which the CFT-integral is considered. The IIM was used to evaluate the SIF using the WARP3D analysis code[26]. The WARP3D is an open source research code for nonlinear FEA of large-scale, 3-D solids and structures subjected to static and dynamic loads. Although the CFT-integral is implemented in the IIM; however, it is only available for a uniform distributed stress field over the crack face. Therefore, in this section, the numerical analysis was performed only for the flat plate model. The same two cases of the flat plate model that given in Table 3.1 were used in this section. The numerical analyses applied the same displacement boundary conditions and the same external tensile loading configuration as conducted in section 3.2.1.

The external loading solutions (K_I-values) given by WARP3D interaction integral method (WARP3D-IIM) were verified with the solutions obtained by Newman-Raju[64][65][66]. Because the generated stress field over the crack face of the uncracked model is uniform, so the applied external loading will be used directly with an inverse sign as traction forces over the crack face. The effectiveness of the CFT-integral on the accuracy of the CFT-solution was verified by comparing the CFT-solution with that computed by external loading. Once again, Eqns. 1.8 and 1.9 were used to examine the solutions of the superposition method steps. Tables 3.6 and 3.7 show the validation of the solutions obtained by the superposition method using the total strain energy and the $CMOD$. It is clear that the difference between the total strain energies and the difference between the crack mouth opening displacements, in Tables 3.6 and 3.7 are negligible which demonstrate the accuracy of the solutions given by the superposition method.

Table 3.6 Validation of the solutions of the superposition method steps obtained by the IIM using the total strain energy, U and $CMOD$ for the flat plate model (case 1).

$U_{(a)}$	$U_{(b)}$	$U_{(c)}$	$U_{(b)} + U_{(c)}$	% difference between $U_{(a)}$ and $U_{(b)} + U_{(c)}$
1.79E+00	1.79E+00	3.33E-04	1.79E+00	5.05E-06
Case	w_1 (mm)	w_2 (mm)	$CMOD$	% difference between $CMOD_{(a)}$ and $CMOD_{(c)}$
Fig. 1.6(a)	1.16E-03	1.22E-03	6.75E-05	0.0178
Fig. 1.6(c)	-3.41E-05	3.34E-05	6.75E-05	

Table 3.7 Validation of the solutions of the superposition method steps obtained by the IIM using the total strain energy, U and $CMOD$ for the flat plate model (case 2).

$U_{(a)}$	$U_{(b)}$	$U_{(c)}$	$U_{(b)} + U_{(c)}$	% difference between $U_{(a)}$ and $U_{(b)} + U_{(c)}$
1.79E+00	1.79E+00	1.98E-03	1.79E+00	7.90E-05
Case	w_1 (mm)	w_2 (mm)	$CMOD$	% difference between $CMOD_{(a)}$ and $CMOD_{(c)}$
Fig. 1.6(a)	1.13E-03	1.25E-03	1.21E-04	0.0149
Fig. 1.6(c)	-6.26E-05	5.84E-05	1.21E-04	

Figure 3.9 shows the distribution of the normalized SIF (K_{In}) calculated by external loading and that obtained by CFT for the flat plate model. The external loading solutions were verified with those obtained by Newman-Raju. A very good matching was obtained between the solutions obtained by external loading and Newman-Raju. On the other hand, an excellent agreement between the external loading solution and that given by CFT along the crack front was obtained

when the CFT-integral is included in the CFT-solution, except at the crack mouth. The difference obtained at the crack mouth between the solutions computed by CFT and external loading may be due to the influence of the FE modeling. As the SIF at the crack mouth strongly depends on the FE modeling and the applied SIF evaluation method.

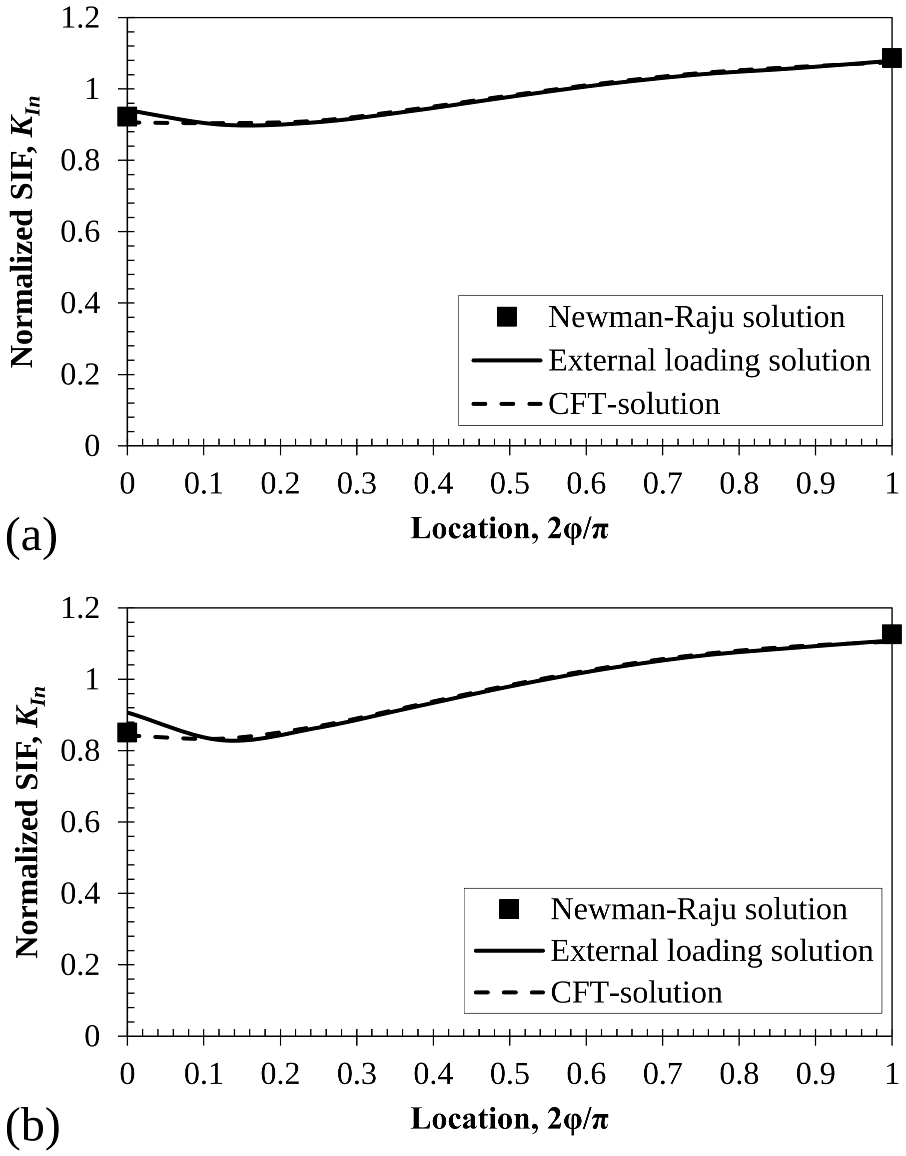

Fig. 3.9 Distribution of the normalized SIF (K_{In}) along the crack front given by the external loading and CFT for the flat plate model using WARP3D-IIM (CFT-integral is considered). (a) case 1, and (b) case 2.

The implementation of the CFT-integral in WARP3D-IIM noticeably decreases the difference between the CFT-solution and that given by external loading, by improving the accuracy of the solutions obtained by CFT. The two solutions become almost identical along the crack front, except at the crack mouth. Further, the percentage difference at the crack deepest point (at $2\varphi/\pi = 1$) between the SIF given by the CFT and that calculated by the external loading is 0.39% for case 1 and 0.28% for case 2.

To confirm the effectiveness of the CFT-integral in improving the accuracy of the CFT-solution, comparisons of the computed SIF are plotted with and without considering the CFT-integral, as shown in Fig. 3.10. For the sake of comparison, the external loading solutions that given by the DI method and IIM are used in Fig. 3.10 as references. It is found that the CFT-integral significantly improves the accuracy of the solutions obtained by CFT. For example, the CFT-integral increases the accuracy of the SIF given by the CFT for the two cases of the flat plate model by 5–6.5% along the crack front (except SIF at the crack mouth) when compared with the solutions that ignored this integral (i.e. CNT-solutions).

In this study, the superposition method is examined only using tensile loading system for the flat plate model and T-butt welded model. However, it is necessary to calculate SIF for surface cracks in non-uniform stress fields based on the superposition method as well as considering the CFT-integral. Therefore, a proposed technique based on the CFT-integral implemented in WARP3D-IIM is introduced in chapter 4.

3.4 Summary

In this chapter, the superposition method was validated numerically using different FE models as well as different numerical integration methods and FE solvers. Furthermore, the significance and effectiveness of the CFT-integral in improving the accuracy of the CFT-solution was discussed. It was found that the difference between the solutions obtained by the external loading and CFT is less than 0.5% at the crack deepest point for the flat plate model. On the other hand, a difference of less than 5% was obtained at the crack deepest point between the solutions computed by external loading and CNT for the flat plate model and T-butt welded model, where the CFT-integral is omitted in MSC Marc-DI solution. Based on that, commercial nonlinear FE codes that neglect the CFT-integral (e.g. MSC Marc) can be used for rough estimation of SIF for surface cracks in stress fields for engineering fracture mechanics problems under the conditions examined in this study.

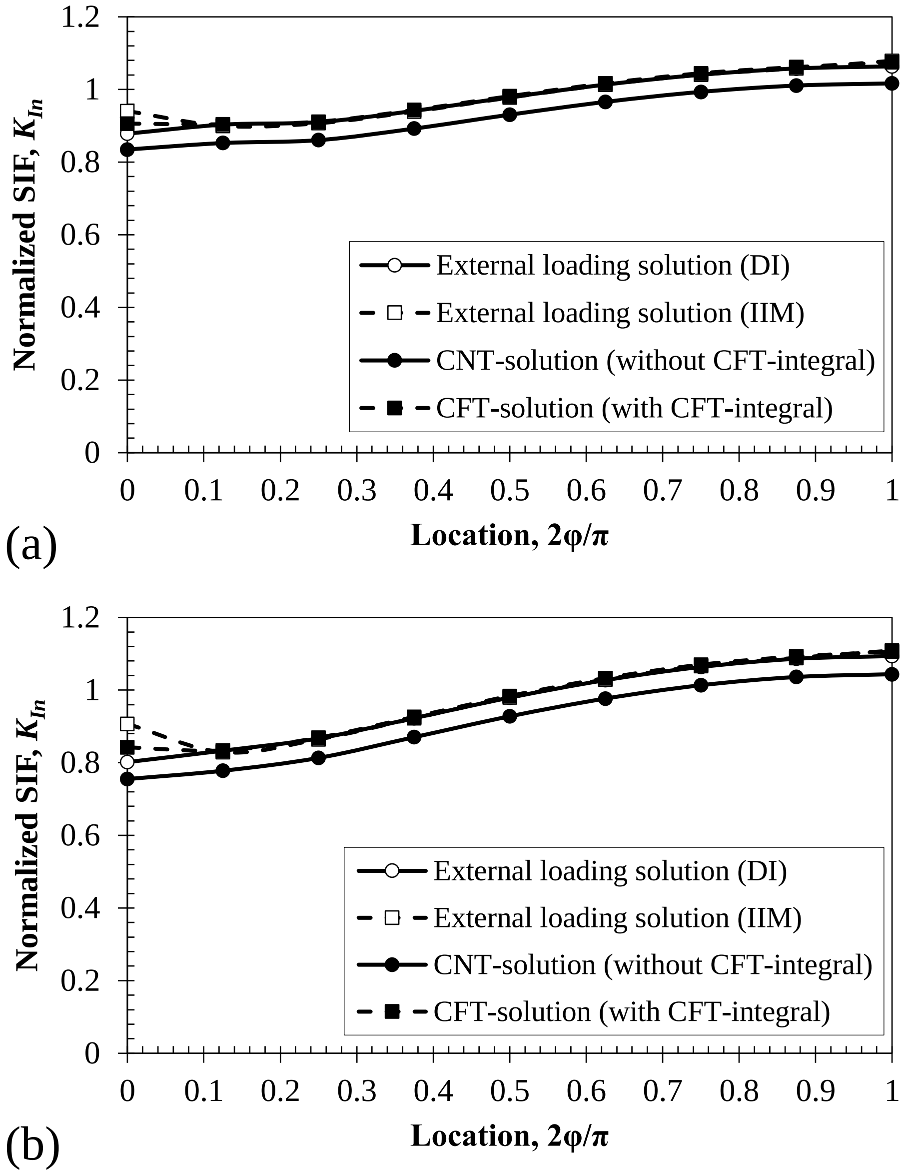

Fig. 3.10 Comparison of the normalized SIF (K_{In}) along the crack front shows the effectiveness of the CFT-integral in improving the accuracy of the SIF calculated by CFT for flat plate model. (a) case 1, and (b) case 2.

CHAPTER 4

Proposed technique for surface cracks in non-uniform stress fields

4.1 Introduction

To consider the RS field in SIF solutions, it is necessary to incorporate the CFT-integral in the applied numerical integration method. The WARP3D-IIM as well as a commercial FE code (i.e. MSC Marc), that neglects the CFT-integral, using the DI method were utilized to evaluate the SIF solutions along the crack front for 3-D surface cracks in flat plate models under external loading and crack face/nodal tractions[69][70]. Gadallah et al.[69][70] also applied the MSC Marc-DI to calculate the SIF for a surface crack in a T-butt welded model. The calculated SIF solutions showed that the CFT-integral must be included in the SIF evaluation methods for cracks in non-uniform stress fields in order to obtain accurate SIF solutions. However, the CFT-integral that implemented in WARP3D code is valid only for uniform distributed tractions over the crack face. This means that this CFT-integral is limited to simple cracked geometries that introduce uniform stress fields over the crack face. For complicated geometries, e.g. welded joints, the crack face bears non-uniform stress fields; due to external loading conditions and induced welding RS. It is therefore necessary to include the non-uniform stress field when calculating SIF to obtain accurate solutions.

An efficient technique is needed to evaluate the SIF for surface cracks in welding RS fields that represent non-uniform stress field. For this reason, a technique that is based on utilizing the CFT-integral implemented in the WARP3D-IIM for models with a particular crack-block mesh density is proposed. 3-D flat plate models with different crack-block mesh densities are employed under different loading conditions to examine the accuracy, conditions and easiness to use of the proposed technique as well as to establish good procedures of applications using this technique. The influence of the crack-block mesh density on the calculated SIF solutions due to the application of non-uniform tractions over the crack face is also discussed. The effectiveness of the proposed technique is then validated for different 3-D numerical examples of welded joints under different loading conditions. To examine the adequacy of the proposed technique and the significance of the CFT-integral on the accuracy of SIF solutions, MSC Marc-DI that neglects the CFT-integral is also adopted. Moreover, the proposed technique is validated for a surface cracked butt-welded joint using a calculated welding RS. After verifying the proposed technique with different numerical examples, it is then employed to evaluate the SIF for a surface cracked butt-welded joint based on real welding RS.

4.2 The proposed technique methodology

The proposed technique[71][72] based on two main points: 1) utilizing the CFT-integral implemented in WARP3D-IIM, and 2) using a particular crack-block mesh density. Therefore, the first part of this section (sections 4.2.1–4.2.3) is dedicated to examine the influence of the crack-block mesh density on the accuracy of the calculated SIF solutions. The CFT-solutions for each crack-block are then examined with those given by external loading configurations. The second part of this section (section 3.2.4) discusses the significance of the CFT-integral on the accuracy of the CFT-solutions based on the proposed technique.

4.2.1 Applied crack-block meshes

The crack-block mesh density was examined using three crack-blocks with different mesh densities, namely, coarse mesh, intermediate mesh and fine mesh. The three crack-blocks have the same size. The crack-block mesh was verified properly and the selected crack-block size was examined appropriately based on trial and error for evaluating the SIF. The FE meshes of the applied crack-blocks are shown in Fig. 4.1. The reason why one-half symmetric FE meshes are used is that all the numerical examples presented in this chapter are symmetric about the longitudinal axis. Only the FE model used in section 4.4 utilized full cracked FE mesh because real welding RS was used. The crack face FE mesh and crack front of the crack-blocks are shown in Fig. 4.2. The crack-blocks are generated with semi-elliptical surface crack. The surface crack has the same aspect ratios for the three crack-blocks as $a/c = 0.5$ and $a/t = 0.225$. An aspect ratio (a_1/a) between the smallest element length (a_1) through the crack depth and the crack depth is given in Table 4.1 to show the variance of the crack-block mesh densities especially over the crack face. As well, the limit of element aspect ratio is to make the element size as small as possible to minimize the difference between the element center and the center of the element face; more details are mentioned in section 4.2.3. Further details of the FE crack-block meshes are given in Table 4.1. The FE meshes of the crack-blocks generated using 20-noded isoparametric hexahedral brick elements. Along the crack front, the 20-noded hexahedral elements are collapsed to quarter-point wedge elements, which are used to simulate the $1/\sqrt{r}$ singularity of the stress field close to the crack front.

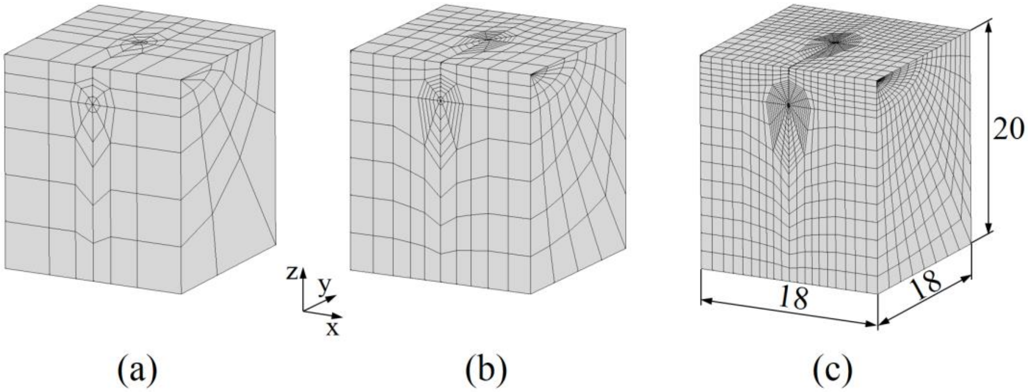

Fig. 4.1 Typical one-half symmetric FE meshes of the crack-blocks. (a) coarse crack-block mesh, (b) intermediate crack-block mesh, (c) fine crack-block mesh. (Note: all dimensions in mm).

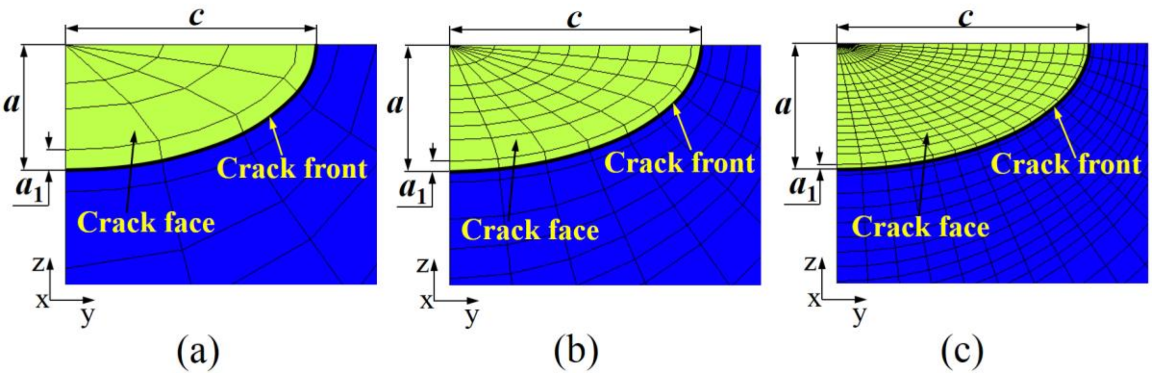

Fig. 4.2 Crack face FE mesh and crack front of the crack-blocks. (a) coarse crack-block mesh, (b) intermediate crack-block mesh, (c) fine crack-block mesh.

Table 4.1 Details of the applied crack-block meshes$^{a)}$.

Crack-block mesh	a_1/a	Total number of elements	Number of elements along the crack front	Number of elements over the crack face	Total number of nodes along the crack front
Coarse	0.167	224	4	16	9
Intermediate	0.083	992	8	64	17
Fine	0.042	7936	16	256	33

$^{a)}$ All data mentioned in this table are for one-half FE crack-block mesh.

4.2.2 FE model definition

For the sake of simplicity, in order to examine the influence of the crack-block mesh density on the accuracy of the calculated SIF solutions, a flat plate model was employed. The geometry of the surface cracked flat plate body is shown in Fig. 4.3. The flat plate body consists of two main parts, namely, the crack-block and global body. The flat plate FE model generated in two steps: 1) create the FE mesh of the crack-block and 2) generate the global mesh. The global mesh generated using 20-noded hexahedral elements. The crack-block mesh then connected to the global mesh using the mesh-tying option offered by WARP3D code. Figure 4.4 shows a close-up view of the tied faces between the crack-block mesh and the global mesh for the different crack-block meshes. The mesh-tying technique makes possible to transit from fine crack-block mesh to coarser global mesh. The constraints produced by mesh-tying define two or more geometrically identical surfaces, as the independent surface which represents the coarse surface and the dependent surface which represents the more refined surface. By selecting the more refined surface as the dependent surface, the possibility of unconnected independent elements is avoided as well as ensures full tying between the independent and dependent surfaces[46].

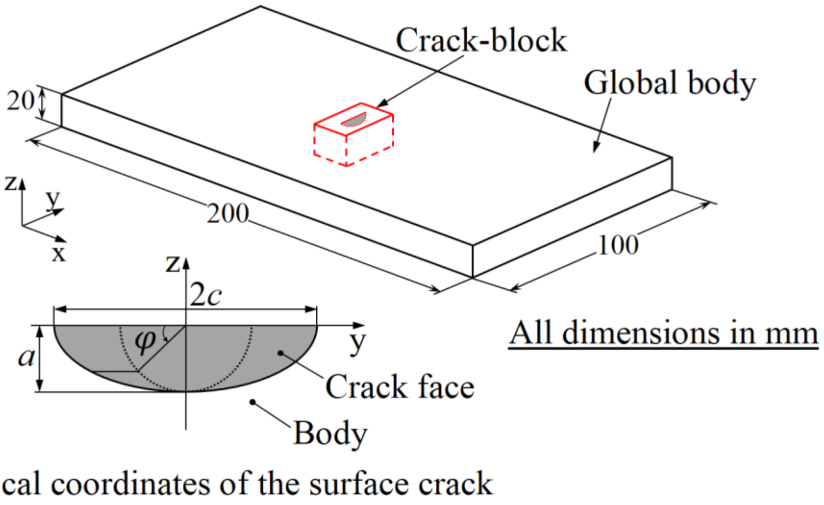

Fig. 4.3 Geometry of the surface cracked flat plate body.

One example of the FE flat plate models that corresponds to Fig. 4.3 and employs the fine crack-block mesh as well as the applied boundary conditions is shown in Fig. 4.5. To introduce non-uniform stress field over the crack face, two separate external loading configurations were employed as bending loading and combined loading as shown in Fig. 4.5(b). The bending loading condition was applied as distributed bending loads at the nodes of the model boundary (y–z plane). The combined loading condition consists of tension load and bending load, in which the tension load was applied as uniform distributed stress over the element faces of the model boundary (y–z plane). Since the cracked body is symmetric about the x-z plane, one-half model was used in the analysis. The arrows in Fig. 4.5(a) show the applied boundary conditions that prevent the rigid body motion of the model. The Young's modulus and Poisson's ratio adopted in the analyses are 210 GPa and 0.3, respectively.

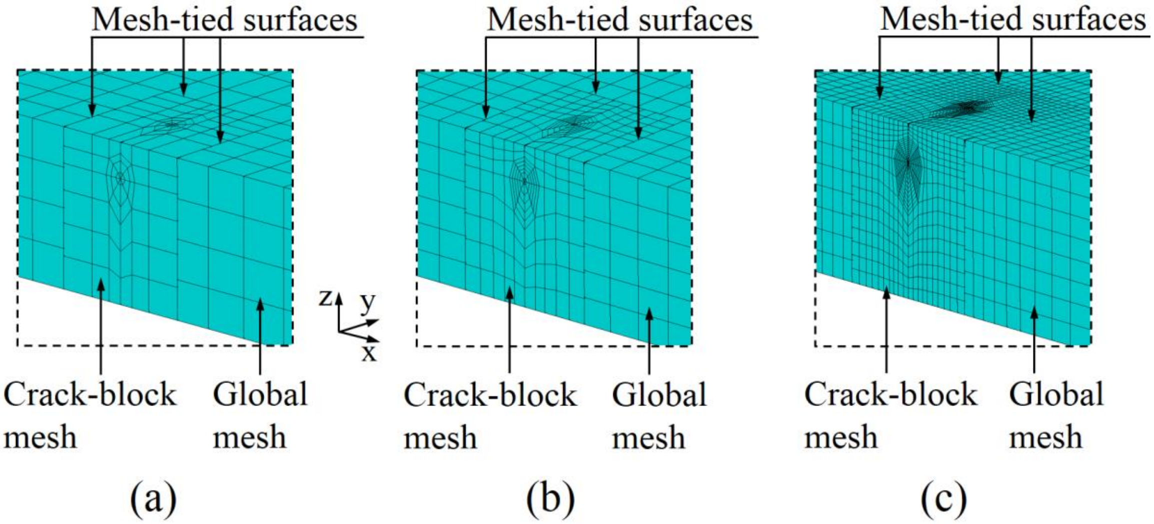

Fig. 4.4 Close-up view of the connected crack-block mesh to global mesh using the mesh-tying technique. (a) coarse crack-block mesh, (b) intermediate crack-block mesh, (c) fine crack-block mesh.

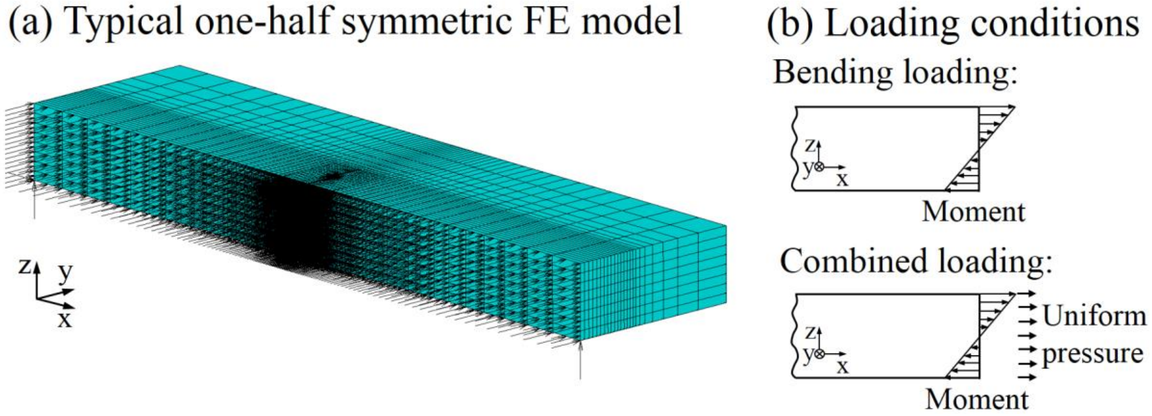

Fig. 4.5 FE flat plate model using fine crack-block mesh and the boundary conditions.

The superposition method was applied in order to validate the calculated CFT-solutions for each crack-block with those given by external loading. To implement the superposition method, the WARP3D code was employed. This code offers two SIF evaluation techniques, namely, the DI method and the IIM. In this study, the WARP3D-IIM was utilized. The CFT-integral was included in the CFT-solutions for the different crack-block meshes. The implementation procedure of the superposition method mentioned in section 3.1.2 and summarized again in this section as follows (based on Fig. 1.6):

1) calculation of SIF solutions (K_I-values) using external loading configuration (Fig. 1.6(a)). The calculated SIF solution in this step called "external loading solution",
2) stress field that arises over the crack face calculated by applying the same external loading configuration to a geometrically identical uncracked model (Fig. 1.6(b)). Further details on how the calculated stress field is extracted are explained in section 4.2.4; and
3) calculated stress field in step 2 is applied as tractions over the crack face with an opposite sign in order to calculate the SIF solutions for a geometrically identical cracked model (Fig. 1.6(c)). The calculated SIF solution in this step called "CFT-solution".

4.2.3 Analysis results

The stress distribution through thickness at the model mid-length (i.e. at the crack location) for the two loading conditions is plotted in Fig. 4.6. The results shown in Fig. 4.6 are obtained by the FE flat plate model using fine crack-block mesh, Fig. 4.5(a) that represents an example of the applied FE flat plate models. Figure 4.6 shows a non-uniform stress distribution at the location of the crack which is used as non-uniform tractions over the crack face. On the other hand, the solution for each step of the superposition method was verified using Eqns. 1.8 and 1.9. Moreover, Fig. 4.7 shows the percentage difference between $U_{(a)}$ and $U_{(b)} + U_{(c)}$ as well as the percentage difference between $CMOD_{(a)}$ and $CMOD_{(c)}$ for each crack-block mesh density. It is observed that, from Fig. 4.7, by increasing the mesh density of the crack-block the percentage difference of the terms of Eqns. 1.8 and 1.9 decreases. This means that, the accuracy of the calculated CFT-solution improves as discussed later.

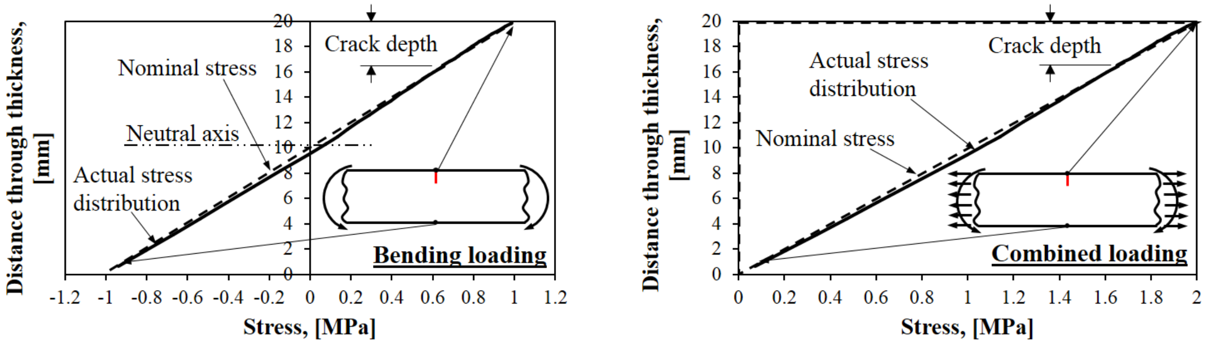

Fig. 4.6 Uncracked stress distribution through thickness at the model mid-length for a flat plate model using fine crack-block mesh under different loading conditions.

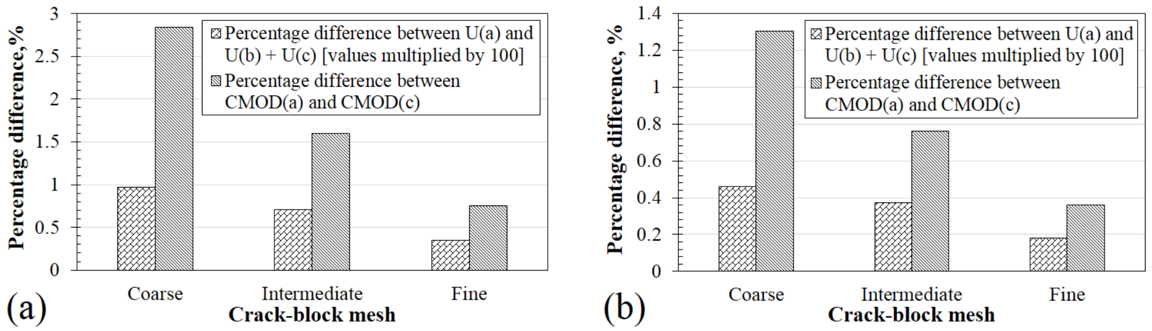

Fig. 4.7 Validation of the solutions for the superposition method steps using WARP3D-IIM. (a) bending loading condition and (b) combined loading condition.

The SIF solutions computed by external loading (bending loading/combined loading) were validated with those obtained by Newman-Raju[65], as shown in Figs. 4.8(a) and 4.9(a). Note that, the crack mouth and crack deepest point are represented at $(2\varphi/\pi = 0)$ and $(2\varphi/\pi = 1)$, respectively. From the results shown in Figs. 4.8(a) and 4.9(a), it was observed that external loading solutions obtained by the different crack-block meshes under bending and combined loading conditions show no big difference along the crack front. Only the smoothness of the SIF solution becomes more accurate when the density of the crack-block mesh be fine enough.

The influence of the crack-block mesh density on the CFT-solutions was then examined by comparing the CFT-solutions with those given by external loading for each loading condition, as shown in Figs. 4.8(b–d) and 4.9(b–d). It was noticed that the density of the crack-block mesh has a considerable influence in improving the accuracy of the calculated CFT-solutions. For example, the fine crack-block mesh gave an excellent matching between the CFT-solution and external loading solution along the crack front, as shown in Figs. 4.8(d) and 4.9(d). As well, a difference of less than 1% was obtained at the crack deepest point between the CFT-solution and that given by external loading for the two loading conditions. On the other hand, the coarse and intermediate crack-block meshes showed a clear difference in the obtained CFT-solutions with those given by external loading along the crack front, especially for the coarse crack-block mesh (see Figs. 4.8(b) and 4.9(b)).

The results shown in Figs. 4.8 and 4.9 reveal that the density of the crack-block mesh plays a significant role in improving the accuracy of the calculated CFT-solution. Where the stress field that arises over the crack face calculated at the center of each element over the crack face; and then applied as tractions to the center of each element face over the crack face. Therefore by reducing the size of crack-block elements (i.e. increase crack mesh density), the difference that results from applying the stress calculated at element center to the element face center becomes small and can be neglected. Based on that, considerable improvement in the accuracy of the CFT-solutions that obtained by flat plate model using fine crack-block mesh was observed (Figs. 4.8(d) and 4.9(d)).

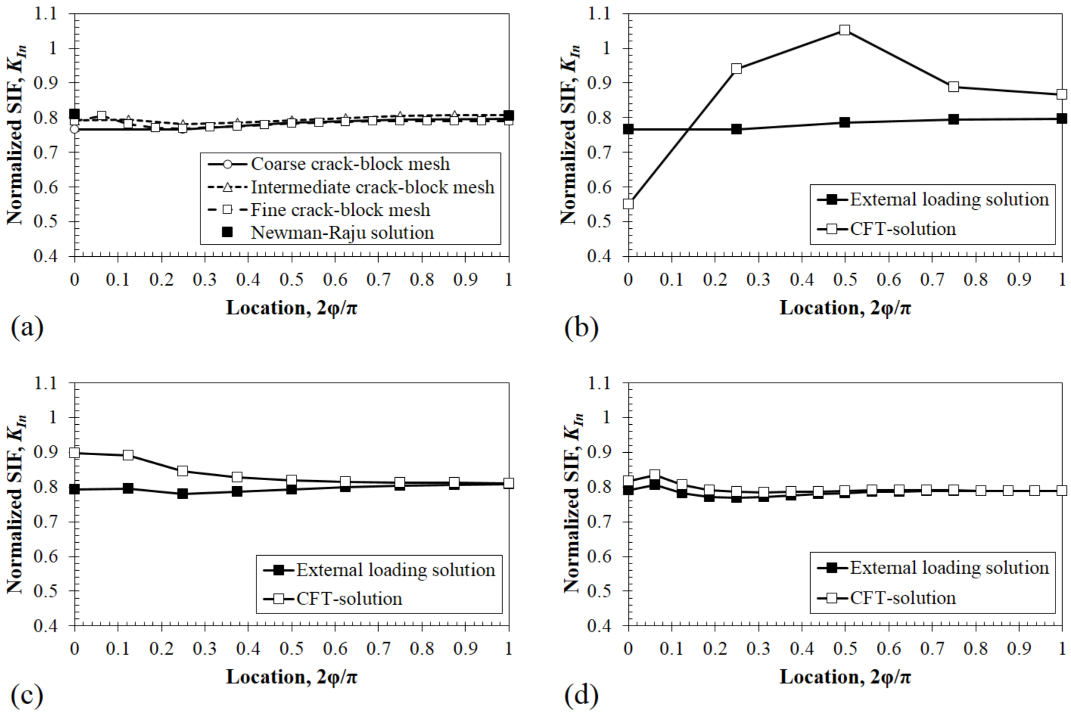

Fig. 4.8 Influence of the crack-block mesh density on the calculated SIF for a flat plate model under bending loading. (a) validation of external loading solutions, (b) coarse crack-block mesh, (c) intermediate crack-block mesh; (d) fine crack-block mesh.

4.2.4 Validation of the proposed technique

In section 4.2.3, excellent CFT-solutions were obtained when the fine crack-block mesh was adopted. To examine the effectiveness of the crack-block mesh density as well as the CFT-integral (i.e. the proposed technique) on the accuracy of the CFT-solutions in depth, the MSC Marc-DI, that represents a commercial FE code, was employed. The MSC Marc solver does not provide the CFT-integral in the DI solution. The same flat plate model with fine crack-block mesh that used in section 4.2.3 was utilized in this section. The same loading conditions that were applied in section 4.2.3 were also adopted in this section. However, in case of MSC Marc, the bending loading condition was applied as moments enforced on reference nodes using the Rigid Body Elements (RBE2) option. RBE2 is a type of rigid body elements, and a tying relation can be constructed between a reference node and tied nodes. The RBE2 option was used in Ref.[68]. The reference nodes located at the center of the model boundary (y–z plane) and the other nodes on y–

z plane are tied nodes, see Fig. 4.10(a). For the combined loading condition, a bending load using the same procedure described for the bending loading condition as well as a uniform stress that used as tension load were applied to the model boundary. The loading conditions are shown in Fig. 4.10(b). The crack-block mesh connected to the global mesh using the glue contact option that is available in MSC Marc solver. The glue contact option suppresses all relative motions between bodies through tying or boundary conditions applying them to all displacement degrees of freedom of the nodes in contact. The same displacement boundary conditions that applied in section 4.2.3 were used in the MSC Marc-DI analyses.

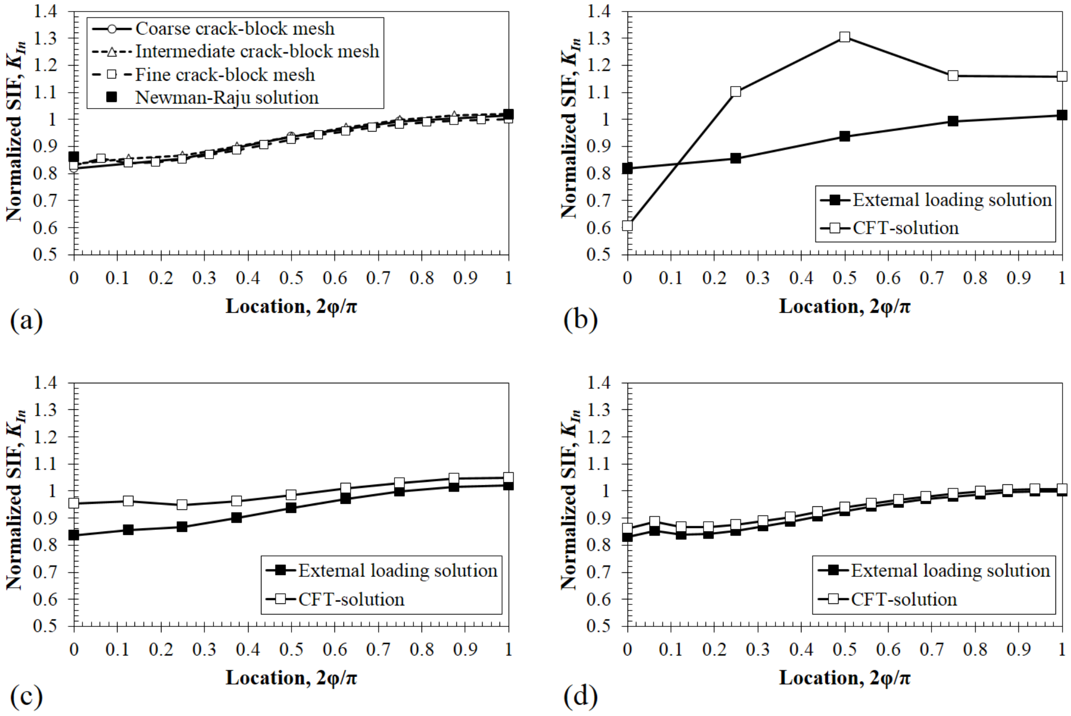

Fig. 4.9 Influence of the crack-block mesh density on the calculated SIF for a flat plate model under combined loading. (a) validation of remote loading solutions, (b) coarse crack-block mesh, (c) intermediate crack-block mesh; (d) fine crack-block mesh.

The superposition method was implemented also using the MSC Marc-DI following the same steps mentioned in section 4.2.2. For WARP3D code, the stress field that arises over the crack face due to the application of external loading to the uncracked model was calculated as stress at the element center for each element over the crack face. The calculated stress field was then used as tractions over the crack face with an opposite sign. However, for MSC Marc solver, the stress field was computed as equivalent nodal forces over the crack face nodes. So in case of MSC Marc solver, the stress field was processed using the same FORTRAN program developed in section 3.2.1. The processed stress field was then applied to the crack face nodes as CNT with an opposite sign. Based on that, SIF was calculated using MSC Marc-DI including the influence of stress field.

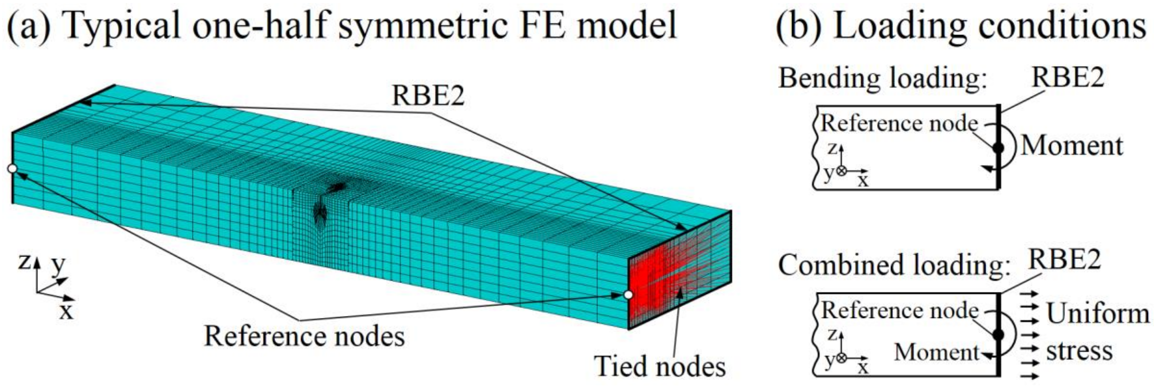

Fig. 4.10 FE flat plate model and the applied loading conditions.

The SIF calculated by external loading using MSC Marc-DI was validated with those obtained by Newman-Raju[65] and WARP3D-IIM for the two loading conditions, as shown in Fig. 4.11. Figure 4.11 also shows a comparison between the CFT-solutions and external loading solutions calculated by WARP3D-IIM as well as a comparison between the CNT-solutions and external loading solutions obtained by MSC Marc-DI. A difference between the solutions given by MSC Marc-DI along the crack front was observed. This difference is due to the absence of the CFT-integral in the DI solutions, as mentioned previously in section 3.2.1. On the other hand, it is clear that when the CFT-integral is included in the IIM, an excellent agreement along the crack front was obtained between the CFT-solutions and those given by external loading (WARP3D-IIM). For example, the percentage difference between the CFT-solution and that obtained by external loading (WARP3D-IIM) at the crack deepest point (at $2\varphi/\pi = 1$) is 0.16% for the bending loading and 0.83% for the combined loading. However, the percentage difference between the CNT-solution and that obtained by external loading (MSC Marc-DI) at the crack deepest point is 2.95% for the bending loading and 3.65% for the combined loading.

It was observed that when the CFT-integral is included in the WARP3D-IIM, the accuracy of the SIF calculated by CFT is considerably improved when compared with that obtained by CNT using the MSC Marc-DI. Additionally, the percentage difference between the solutions at the crack deepest point under different loading conditions was found to be less than 1% when the WARP3D-IIM as well as a fine crack-block mesh density were utilized (i.e. the proposed technique).

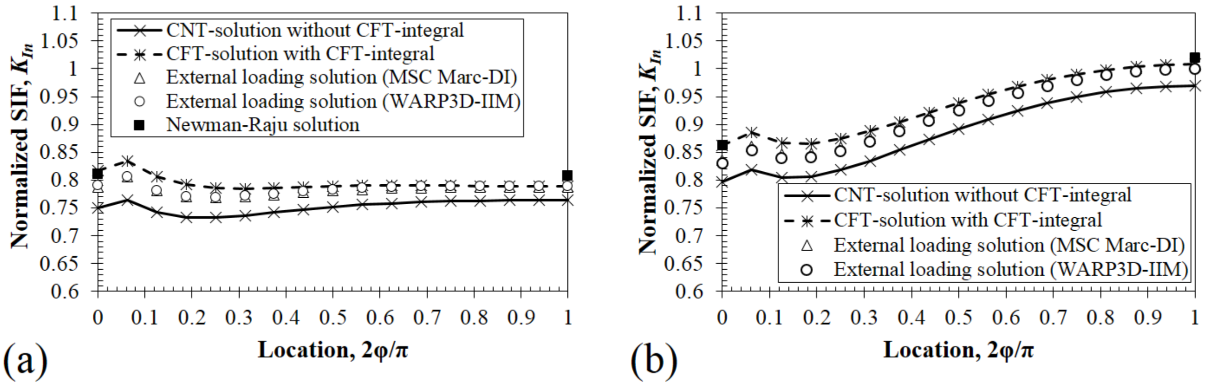

Fig. 4.11 Distribution of the normalized SIF along the crack front calculated by the MSC Marc-DI and WARP3D-IIM for a flat plate model with fine crack-block mesh. (a) bending loading condition, (b) combined loading condition.

From the results shown in sections 4.2.3 and 4.2.4, the SIF calculated by CFT using the WARP3D-IIM is highly influenced by the crack-block mesh density. As well, when the CFT-integral is included in the WARP3D-IIM the accuracy of the CFT-solutions is considerably improved. This shows that the proposed technique can be employed to evaluate the SIF for surface cracks in non-uniform stress fields for complicated FE models. Based on that, the fine crack-block mesh was adopted to be used in sections 4.3 and 4.4 that examine the proposed technique for different welded joints.

4.3 Numerical examples of welded joints

Welded joints are widely used in the field of shipbuilding and offshore structures. For surface cracks at weld toes of butt or T-butt welded joints, the situation is very complicated when compared with flat plates. The influence of the geometry of the welded joint becomes also complicated. Owing to geometrical parameters such as the shape of the weld bead and weld toe angle, a stress concentration and therefore large values of RS are induced at weld toes. This leads to a very complicated distribution of the RS that caused by service loading. Thus, a non-uniform stress field arises over the crack face. It is therefore necessary to include the influence of this non-uniform stress field in the calculated SIF to obtain accurate solutions. As well, such welded joints are good examples to examine the effectiveness of the proposed technique.

In this section, two welded joints, namely, butt-welded joint and T-butt welded joint were employed based on the superposition method. In addition, the proposed technique was examined for a butt-welded joint based on calculated welding RS.

4.3.1 Butt-welded model

4.3.1.1 FE model definition

The geometry of the surface cracked butt-welded joint is shown in Fig. 4.12. The FE model corresponding to the butt-welded joint is shown in Fig. 4.13. Symmetry about the x-axis permits use of a one-half model. The crack-block mesh and global mesh generated by the same procedures mentioned in sections 4.2.1 and 4.2.2. The crack-block generated with a fine mesh and has a semi-elliptical surface crack with aspect ratios of a/c = 0.39 and a/t = 0.175. The crack-block mesh was connected to the global mesh using the mesh-tying option that available in WARP3D code, and using the glue contact option that offered by MSC Marc solver. Three loading conditions were utilized for the MSC Marc and WARP3D analyses, as shown in Fig. 4.14. The loading conditions assigned in this section follow the same procedures that described in sections 4.2.2 and 4.2.4. Due to the geometry of the butt-welded joint (e.g. weld toe) as well as the applied loading condition, a non-uniform stress field was introduced over the crack face. Young's modulus and Poisson's ratio employed in the analyses have values of 210 GPa and 0.3 respectively, which represent typical properties for steel materials. The rigid body motion of the models was prevented by applying the minimum displacement constraints, as shown in Fig. 4.13. The superposition method was applied using the WARP3D-IIM and MSC Marc-DI, following the steps mentioned in section 4.2.2, to evaluate the SIF solutions under the different loading conditions.

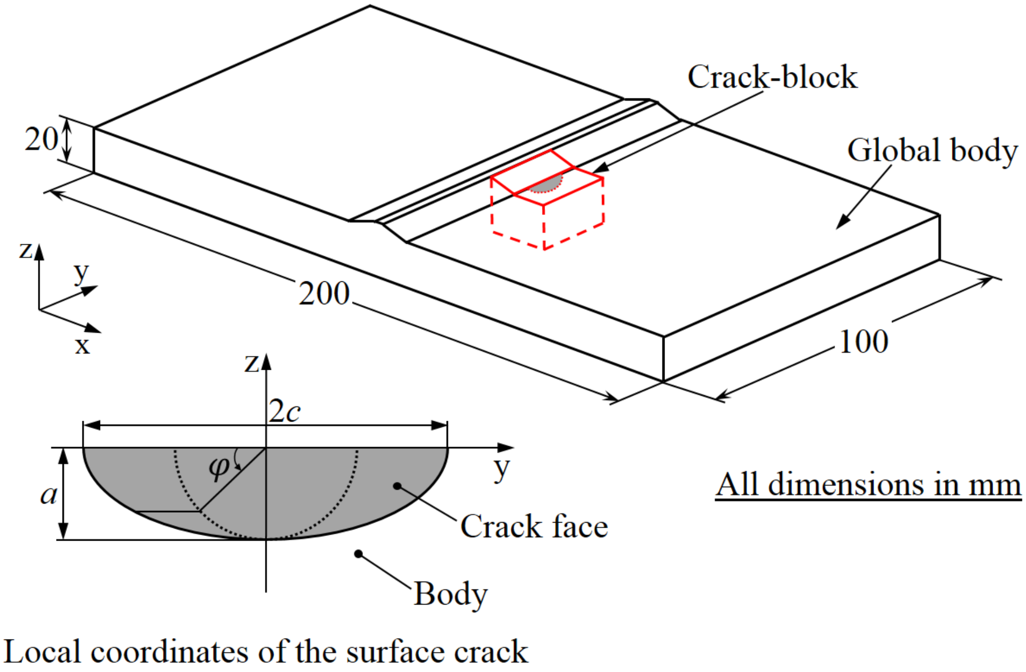

Fig. 4.12 Geometry of the surface cracked butt-welded joint.

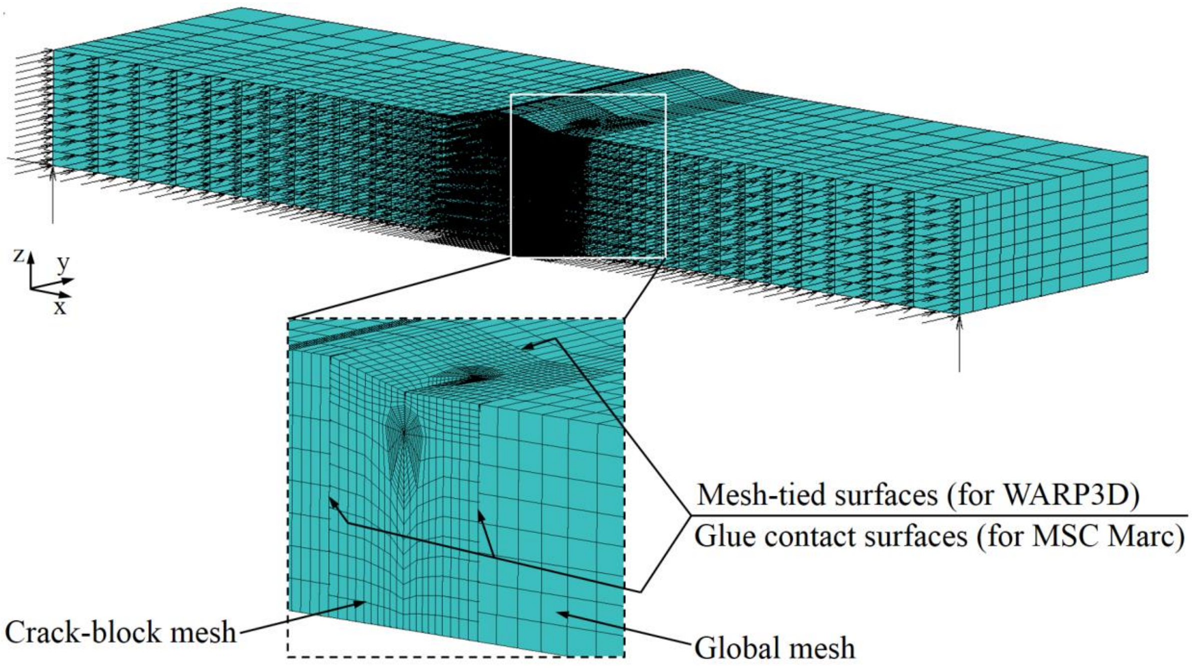

Fig. 4.13 Typical one-half symmetric FE butt-welded model with the boundary conditions.

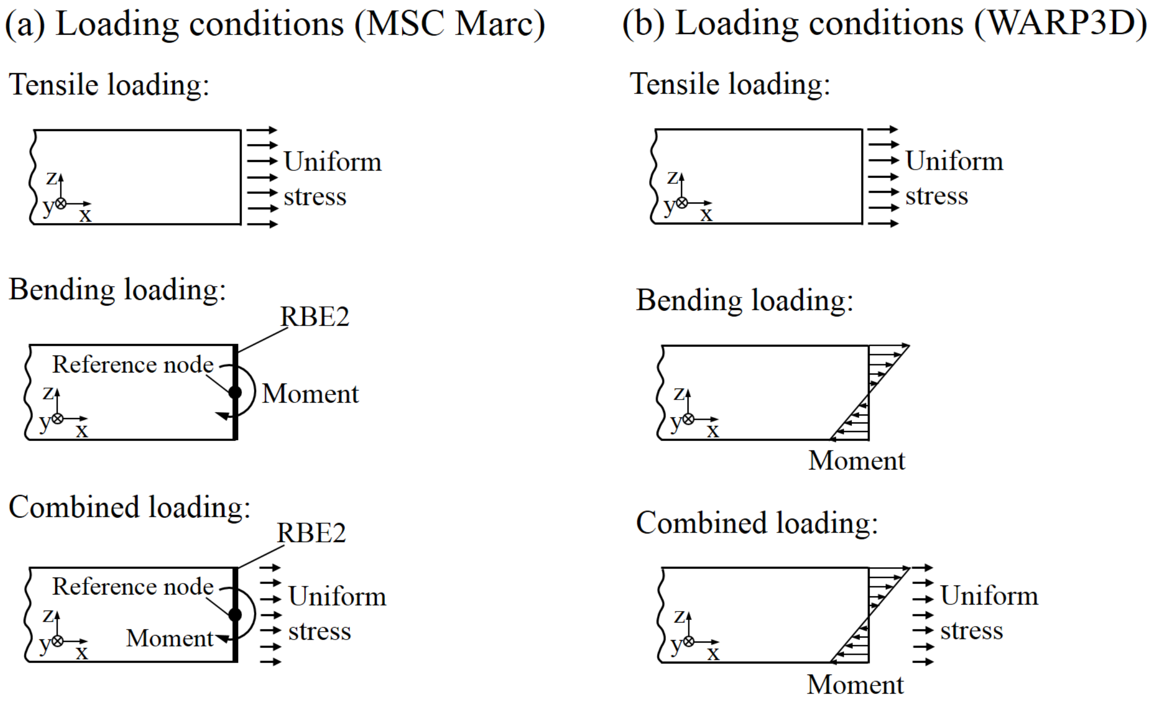

Fig. 4.14 Applied loading conditions for the butt-welded model.

4.3.1.2 Analysis results

To show the effectiveness of the proposed technique for the butt-welded model, the stress distribution through thickness at the weld toe induced by the different loading conditions for the uncracked model is plotted in Fig. 4.15. Figure 4.15 illustrates that the surface stress increases (singular stress) due to the effect of the geometry of the weld bead (i.e. weld toe) as well as a reduction in the stress is introduced through the thickness. This means that the crack face subjected to a non-uniform stress field.

Since the accuracy of the SIF solutions obtained by CFT (WARP3D-IIM) and CNT (MSC Marc-DI) are validated through comparisons with those given by external loading; hence, the external loading solutions must be first verified for each loading condition. The external loading solutions were calculated by three different numerical integration methods, namely, MSC Marc-DI, WARP3D-IIM, in addition to WARP3D domain integral method (WARP3D-DI) for each loading condition. Figure 4.16 shows the validation of the external loading solutions computed by the different SIF evaluation methods. An excellent agreement among the three solutions for the three loading conditions was obtained along the crack front except at the crack mouth (at $2\varphi/\pi = 0$). The reason why WARP3D-IIM gave a larger K_I-value at the crack mouth location is because the IIM implements a simplified assumption that does not include the stress singularity at notches (notches due to model geometry). Thus in order to make simple comparisons between the external loading solutions and those given by CFT and CNT, the SIF at the crack mouth location for the three loading conditions was omitted.

To show the significance of the CFT-integral on the accuracy of the calculated SIF, the SIF solutions given by CNT and CFT were compared with those obtained by external loading for the different loading conditions, as shown in Fig. 4.17. The CFT-solutions showed an excellent matching with those obtained by external loading (WARP3D-IIM) along the crack front especially at the crack deepest point (at $2\varphi/\pi = 1$) for the different loading conditions. On the other hand, a fairly good agreement between the CNT-solutions and external loading solutions (MSC Marc-DI) was obtained for the different loading conditions. The difference between the CNT-solutions and those given by external loading along the crack front obtained due to the absence of the CFT-integral in MSC Marc-DI method. The percentage difference between the CNT-solutions and those given by external loading (MSC Marc-DI) at the crack deepest point for the tensile, bending and combined loading conditions are 3.47%, 2.65% and 3.23%, respectively. However, when the CFT-integral is included in the CFT-solutions, the percentage difference between the CFT-solutions and those computed by external loading (WARP3D-IIM) at the crack deepest point for the tensile, bending and combined loading conditions are decreased significantly to be 0.16%, 0.89% and 0.14%, respectively. It is clear that the CFT-integral considerably improves the accuracy of the CFT-solutions where a percentage difference of less than 1% was obtained between the solutions (CFT and external loading solutions) at the crack deepest point.

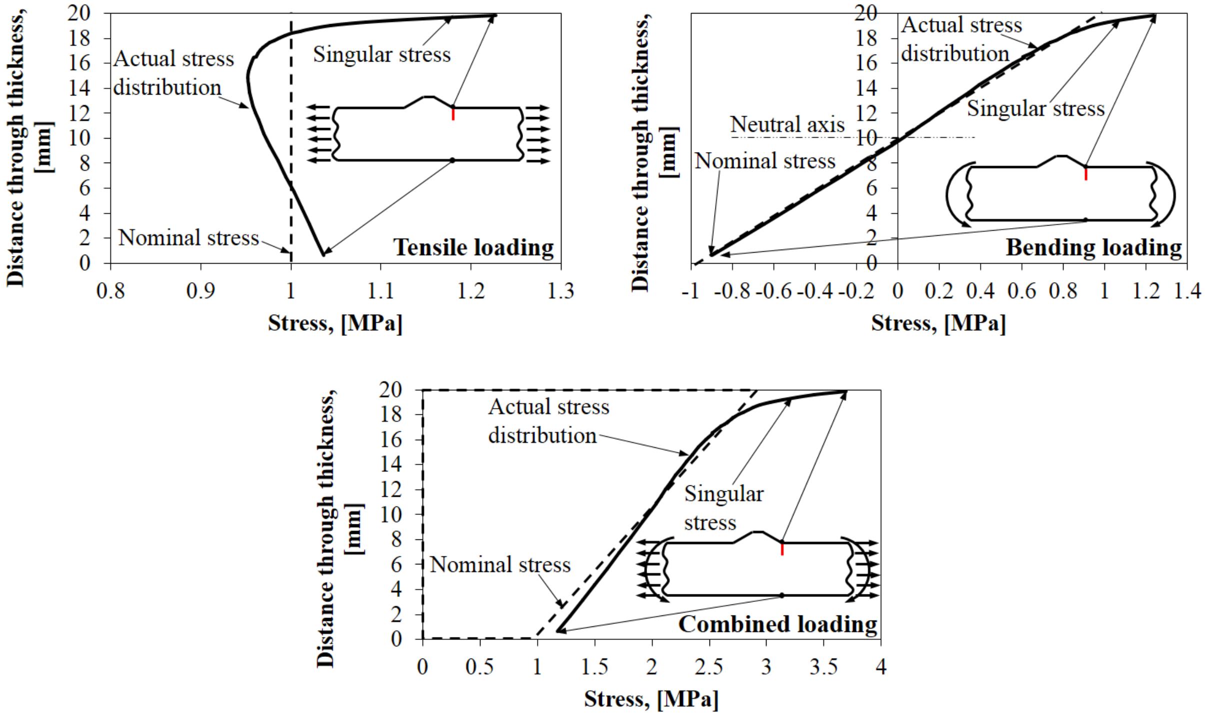

Fig. 4.15 Uncracked stress distribution through thickness at the weld toe for a butt-welded model under different loading conditions.

4.3.2 T-butt welded model

4.3.2.1 FE model definition

In the field of shipbuilding and offshore structures, the stiffened welded panels that mainly consist of many T-butt welded joints are widely used. SIF was evaluated for a semi-elliptical surface cracked T-butt welded joint using different SIF evaluation methods[68][73]. It is therefore necessary to examine the adequacy of the proposed technique for such welded joints.

The geometry of the surface cracked T-butt welded joint was presented in chapter 3 and is shown again in this section in Fig. 4.18. The cracked T-butt welded joint consists of a one-sided weld with a radiused weld toe as used by Bowness and Lee[61]. The FE model of the cracked T-butt welded joint is shown in Fig. 4.19. A FORTRAN program was developed to automatically

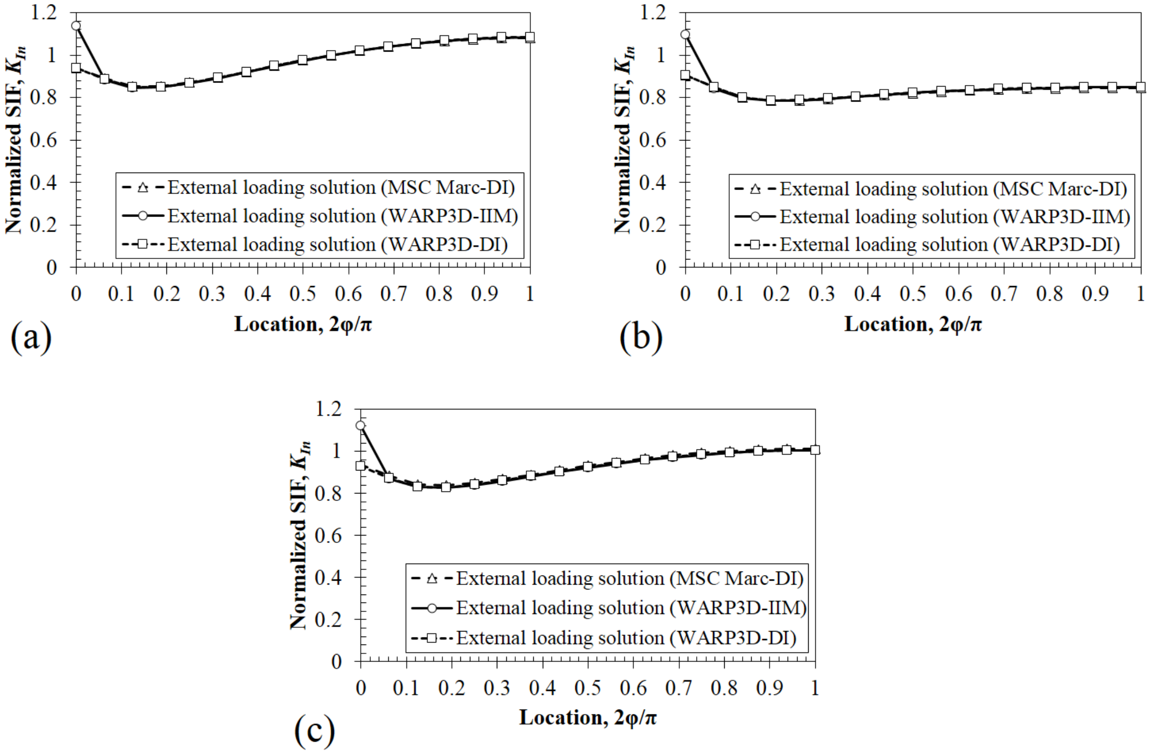

Fig. 4.16 Validation of external loading solutions obtained by different SIF evaluation methods for a butt-welded model subjected to: (a) tensile loading condition, (b) bending loading condition; and (c) combined loading condition.

generate the radiused weld toe. The crack-block and global meshes generated by the same procedures introduced in sections 4.2.1 and 4.2.2. The crack-block generated using a fine mesh and has a semi-elliptical surface crack with aspect ratios of a/c = 0.33 and a/t = 0.09. The crack-block mesh linked with the global mesh by the glue contact option offered by MSC Marc solver, and by the mesh-tying option that is available in WARP3D code. The same loading conditions that employed in section 4.3.1 were applied to the T-butt welded model (see Fig. 4.20). One-half FE model was employed in the analysis because of the symmetry about the x- axis. Young's modulus of 210 GPa and Poisson's ratio of 0.3 were assigned in the analyses. Minimum displacement constraints were applied to prevent the rigid body motion, as shown in Fig. 4.19.

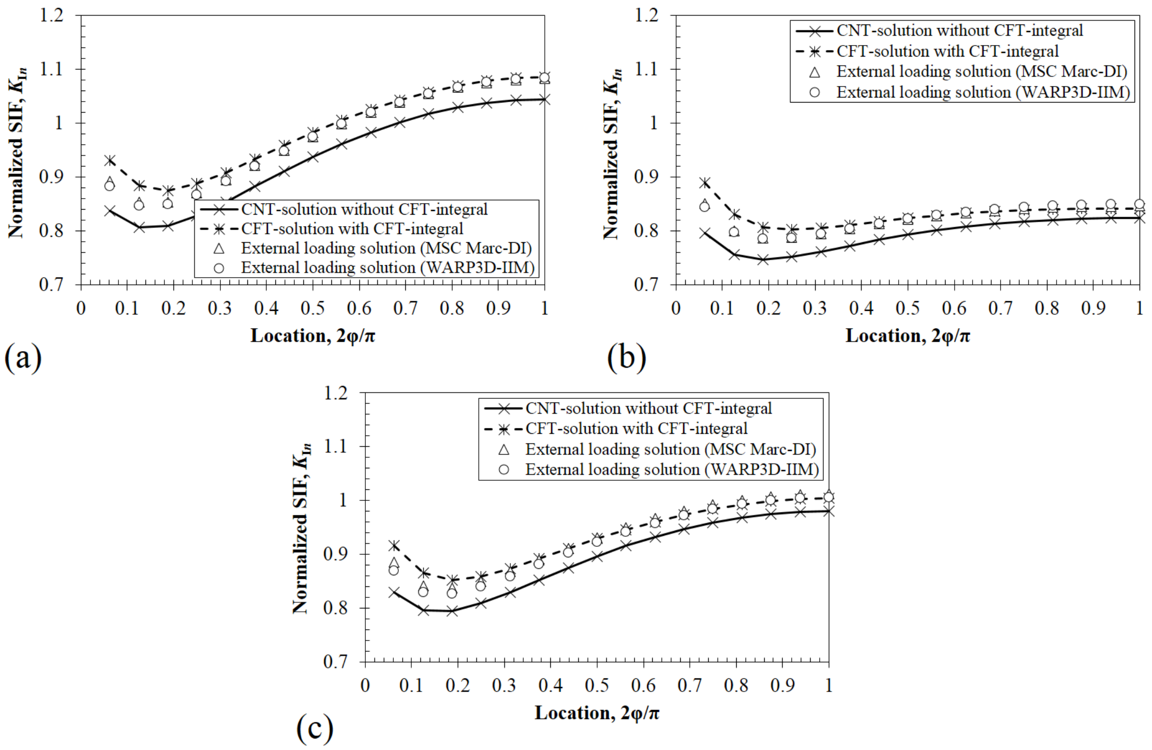

Fig. 4.17 Distribution of the normalized SIF along the crack front calculated by the MSC Marc-DI and WARP3D-IIM for a butt-welded model. (a) tensile loading condition, (b) bending loading condition, (c) combined loading condition. (Note: SIF at the crack mouth location, at $2\varphi/\pi = 0$, was omitted).

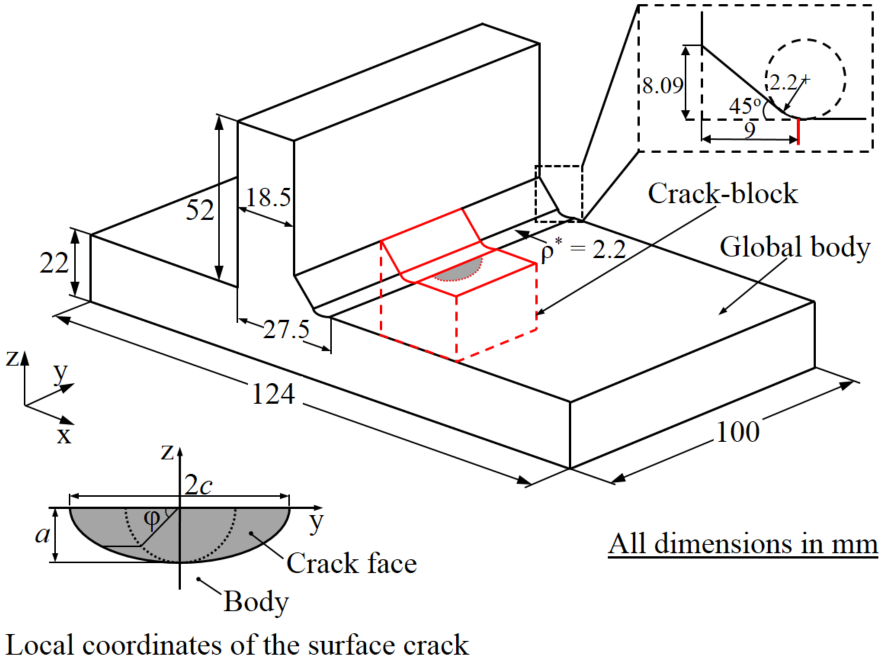

Fig. 4.18 Geometry of the surface cracked T-butt welded joint.

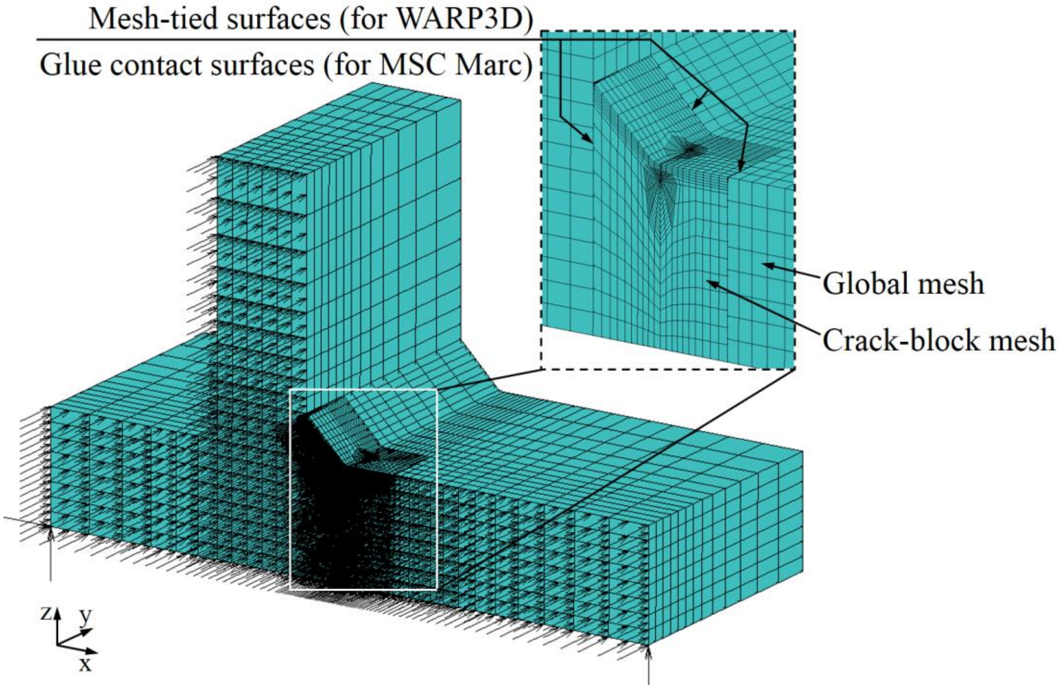

Fig. 4.19 Typical one-half symmetric FE T-butt welded model with the boundary conditions.

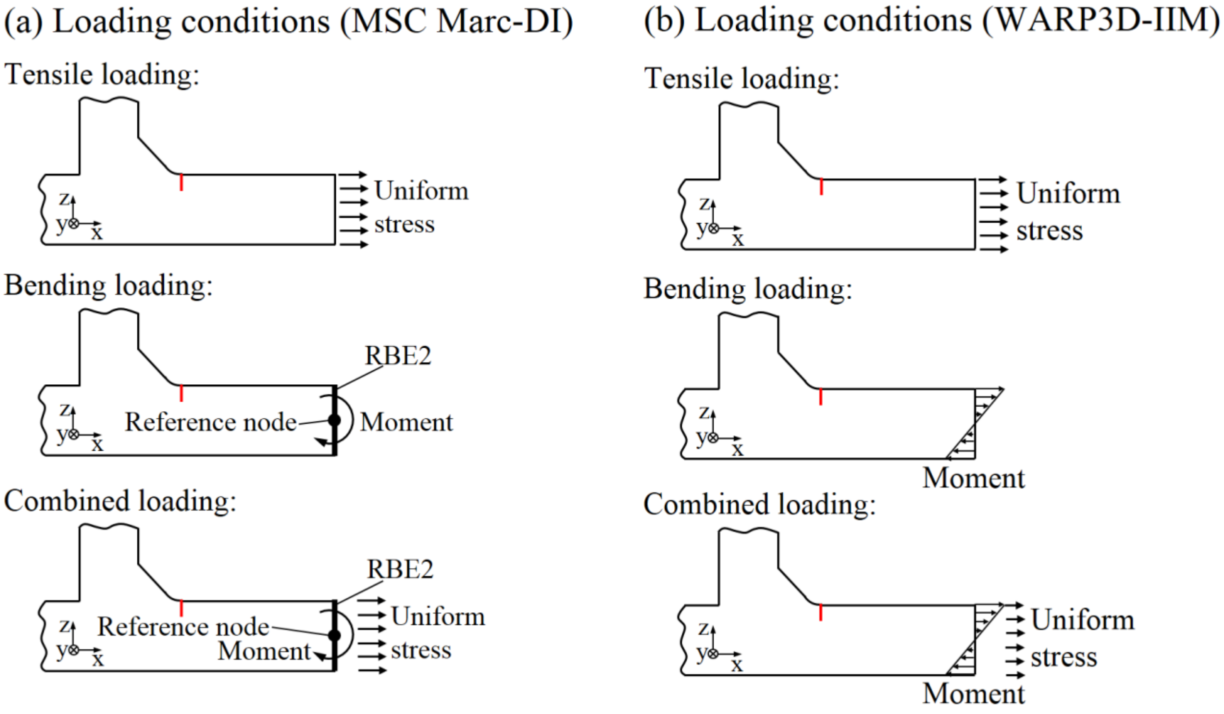

Fig. 4.20 Applied loading conditions for the T-butt welded model.

4.3.2.2 Analysis results

The uncracked stress distribution through thickness at the weld toe for the different applied loading conditions is shown in Fig. 4.21. Due to the influence of the weld toe, the stress at the upper surface of the main plate of the T-butt welded model noticeably increases (singular stress). This singular stress forms a non-uniform stress field over the crack face. On the other hand, through the thickness of the main plate at the weld toe a reduction in the stress was obtained as reported by Bowness and Lee[74].

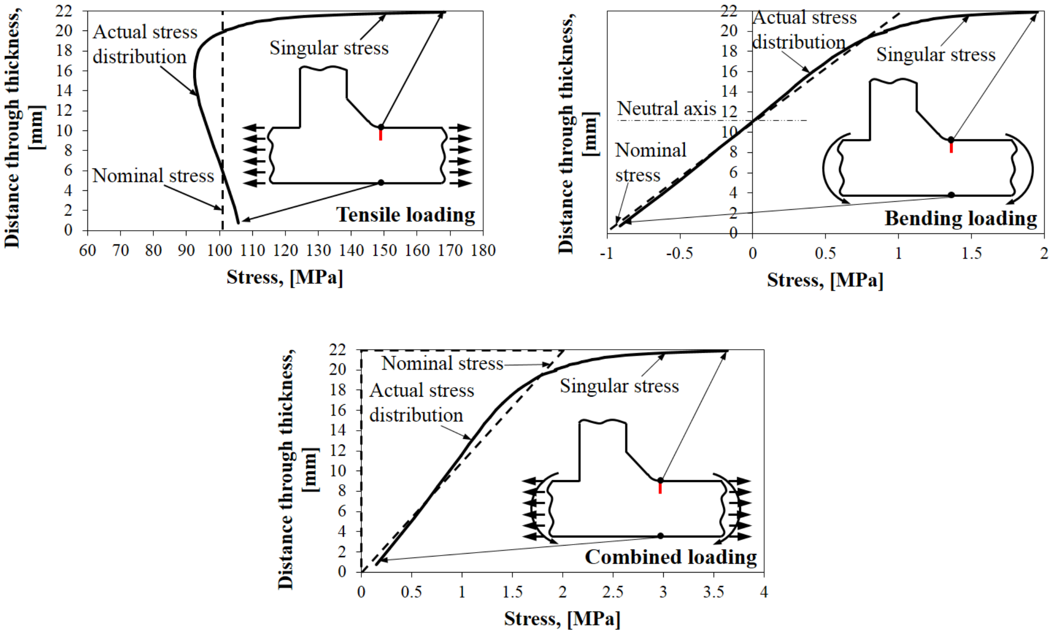

Fig. 4.21 Uncracked stress distribution through thickness at the weld toe for a T-butt welded model under different loading conditions.

The superposition method was then used to evaluate the SIF solutions due to the application of the CFT and CNT. The solutions given by external loading were first verified to be a reliable reference for those obtained due to the application of CFT and CNT. The external loading solution for each loading condition was calculated using the same SIF evaluation methods that employed in section 4.3.1. The external loading solutions were then validated for each loading condition, as shown in Fig. 4.22. A very good matching among the three solutions was obtained along the crack front for each loading condition, excluding the SIF at the crack mouth (at $2\varphi/\pi = 0$). The difference obtained at the crack mouth is due to the same reason mentioned in section 4.3.1.2 in addition to the restraining effect of the attachment that reduced the singularity from $r^{0.5}$to about $r^{0.4}$, as discussed by Bowness and Lee[61]. Thus, the IIM results were in error at the crack mouth location because this technique is based on the initial assumption of a $r^{0.5}$ singularity. Consequently, stress singularities obtained due to the mentioned reasons were superposed and gave this difference between the IIM and DI solutions at the crack mouth location. Based on that, the SIF at the crack mouth was omitted when the CFT-solutions and CNT-solutions compared with those calculated by external loading.

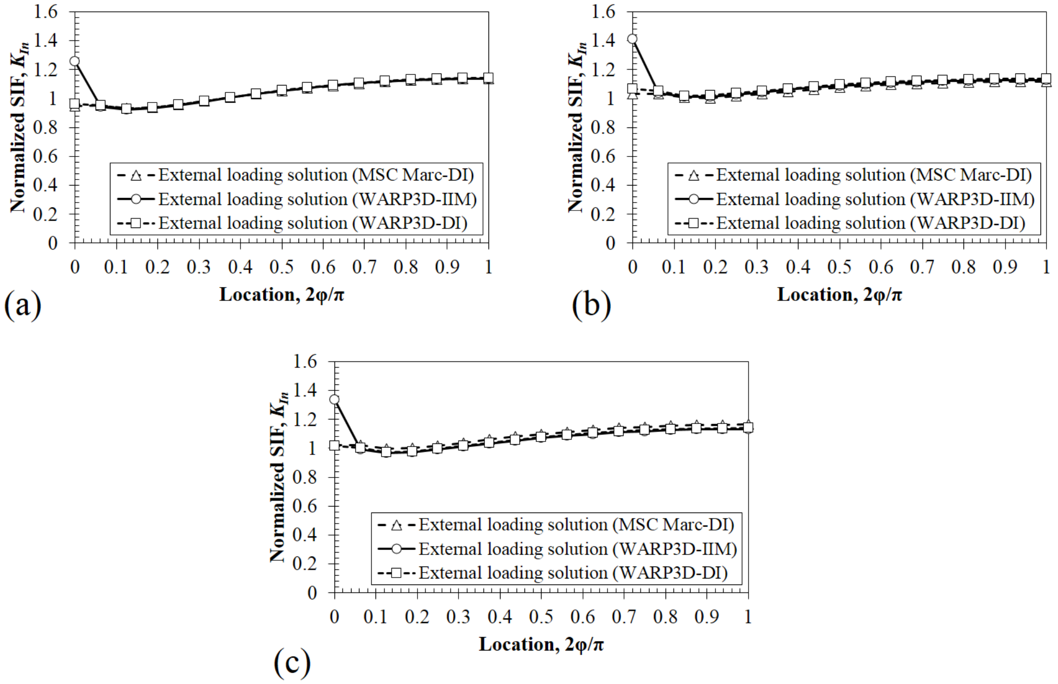

Fig. 4.22 Validation of external loading solutions obtained by different SIF evaluation methods for a T-butt welded model subjected to: (a) tensile loading condition, (b) bending loading condition; and (c) combined loading condition.

In order to demonstrate the significance of the CFT-integral on the accuracy of the calculated SIF, comparisons between the SIF solutions obtained by CFT and CNT and those given by external loading (MSC Marc-DI and WARP3D-IIM) under different loading conditions are plotted in Fig. 4.23. An excellent agreement was obtained between the CFT-solutions and those calculated by external loading (WARP3D-IIM) along the crack front for each loading condition particularly at the crack deepest point (at $2\varphi/\pi = 1$). On the other hand, a fairly good matching was observed between the CNT-solutions and those given by external loading (MSC Marc-DI). Since the CFT-integral is not included in the CNT-solutions, a difference between the CNT-solutions and those calculated by external loading (MSC Marc-DI) was noticed along the crack front. To clearly show the significance of the CFT-integral on the accuracy of the computed SIF, the percentage difference between the solutions calculated by MSC Marc-DI as well as those computed by WARP3D-IIM at the crack deepest point was examined. For example, the percentage difference obtained at the crack deepest point between the solutions given by CNT and those calculated by external loading (MSC Marc-DI) for the tensile, bending and combined loading conditions is 3.67%, 3.32% and 3.45%, respectively. However, by considering the CFT-integral in the CFT-solutions, the percentage difference between the CFT-solutions and those given by external loading (WARP3D-IIM) at the crack deepest point for the tensile, bending and combined loading conditions is considerably decreased to be 0.19%, 0.28% and 0.06%, respectively. As it is clear when the CFT-integral is considered in the solutions, a percentage difference of less than 1% was obtained at the crack deepest point.

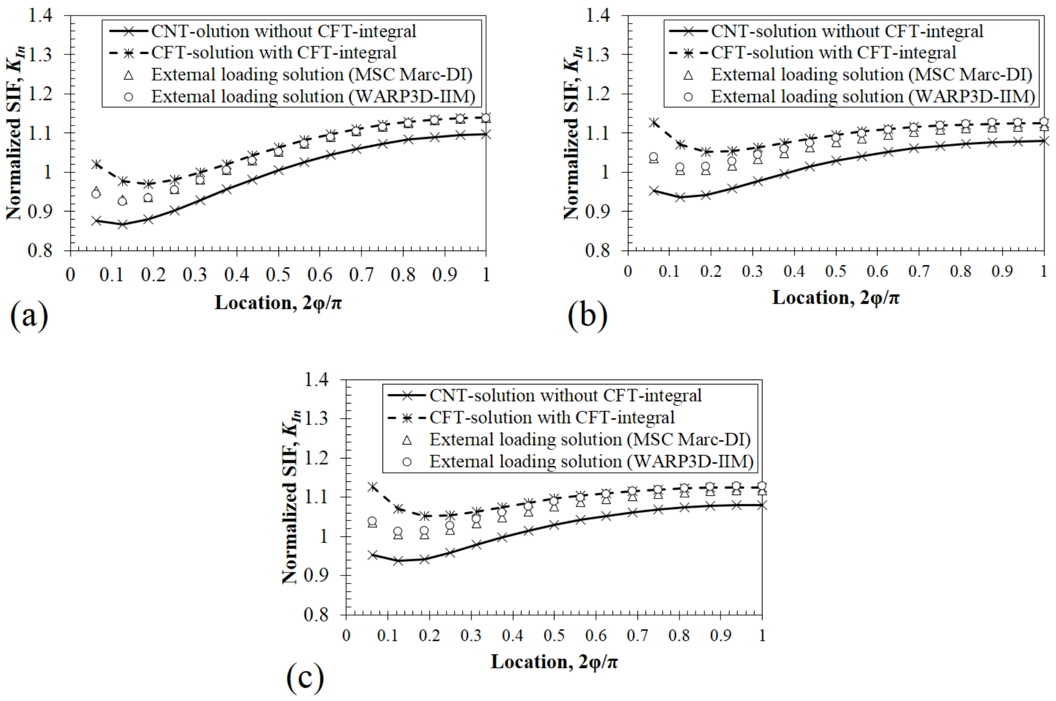

Fig. 4.23 Distribution of the normalized SIF along the crack front calculated by the MSC Marc-DI and WARP3D-IIM for a T-butt welded model. (a) tensile loading condition, (b) bending loading condition, (c) combined loading condition. (Note: SIF at the crack mouth location, at $2\varphi/\pi = 0$, was omitted).

4.3.3 Butt-welded model including welding RS

In sections 4.3.1 and 4.3.2, the non-uniform stress field was introduced based on the model geometry and applied loading conditions. In this section, a problem that includes a welding RS was examined. For this purpose, a butt welded joint with a semi-elliptical surface crack was utilized as shown in Fig. 4.24(a). The FE models used in this section followed the same procedures that mentioned in section 4.2.2 and shown in Fig. 4.5. Two cases were studied in this section using different crack aspect ratios as *a*/*t* = *a*/*c* = 0.2 and *a*/*t* = *a*/*c* = 0.6. Shiratori et al.[75] formulated an equation to calculate the welding RS for a butt welded joint, as follows:

$$\frac{\sigma_x}{\sigma_o} = 3\left(\frac{y}{c}\right)^3 - \frac{9}{2}\left(\frac{y}{c}\right)^2 + 1, \qquad 0 \le y \le c \tag{4.1}$$

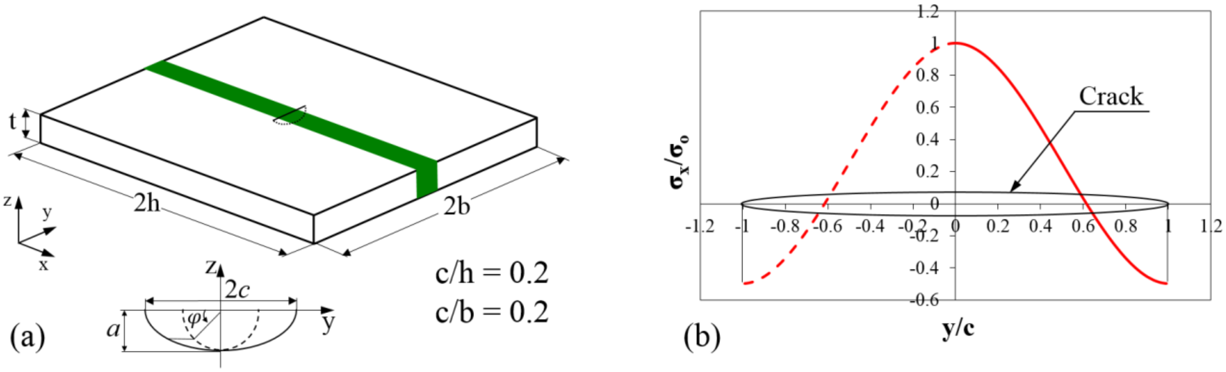

Fig. 24 Details of the butt-welded joint. (a) geometry of the surface cracked butt-welded joint, and (b) distribution of the calculated welding RS.

The distribution of the calculated welding RS using Eq. 4.1 is shown in Fig. 4.24(b). The welding RS was calculated at the center of each element over the crack face. To calculate the RS (σ_x), a maximum stress (σ_o) of 300 MPa was utilized. The calculated welding RS was then applied as tractions over the crack face using the proposed technique in order to calculate the SIF solutions. Due to the symmetry of the cracked body about the x-axis, one-half symmetric FE models were used in the analyses. Young's modulus of 206 GPa and Poisson's ratio of 0.3 were assigned in the analyses.

The applied welding RS field over the crack face opened the crack and the SIF was calculated using the proposed technique. Fig. 4.25 shows a comparison between the solutions given by the proposed technique and those obtained by Shiratori et al.[75] for a semi-elliptical surface crack in a welding RS field. An excellent agreement obtained between the solutions along the crack front for the different crack aspect ratios. The difference obtained between the solutions for the problem with crack aspect ratios of *a*/*t* = *a*/*c* = 0.2 may be due to two reasons. The first reason is the applied crack mesh density. Shiratori et al. used a coarse crack block mesh in their work; however, in the present proposed technique a fine crack mesh density was employed. The other reason is the applied SIF estimation method. Shiratori's solution based on direct method using the displacement extrapolation method. however, the solution calculated by the proposed technique based on the IIM that considered a robust and effective method for evaluating SIF. Therefore, by employing the IIM that includes the CFT-integral using a fine crack mesh, an SIF solution with high accuracy can be obtained. Although a slight difference was observed between the proposed solution and that given by Shiratori, the matching between the solutions is very good, in general. Further, the excellent agreement between the solutions, shown in Fig. 4.25, demonstrates the adequacy of the proposed technique as well as supports the proposed technique to be applied for surface cracks in a real welding RS field.

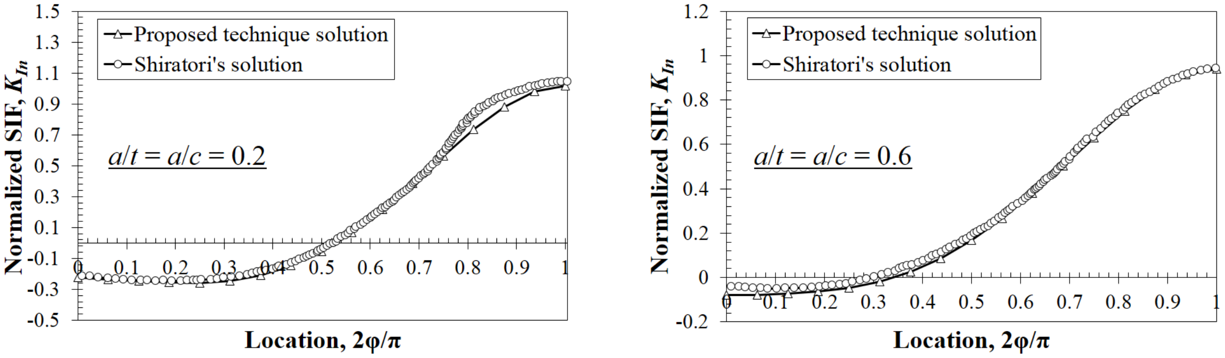

Fig. 4.25 Validation of the proposed technique solution with Shiratori's solution for a semi-elliptical surface crack in a welding RS field.

4.3.4 Discussion

For the butt and T-butt welded models discussed in sections 4.3.1 and 4.3.2, the solutions obtained by the CNT for the different loading conditions were observed to be less than those given by external loading (MSC-MARC-DI). To obtain CNT-solutions with a high accuracy, the CFT-integral is needed to be implemented in the DI method[22][37]. However, although the CFT-integral is not taken into account in the MSC Marc-DI, the results given by MSC Marc-DI showed a good accuracy. It was found that, for the different loading conditions, the percentage difference between the CNT-solutions and those calculated by external loading (MSC Marc-DI) at the crack deepest point was less than 4% for the two welded models even when the CFT-integral is not considered in the CNT-solutions. This shows that commercial FE packages that neglect the CFT-integral, such as MSC Marc, can be used to roughly estimate SIF for surface cracks in non-uniform stress fields for engineering problems under the conditions examined in this study.

On the other hand, from the presented numerical examples, it was noticed that the implementation of the numerical analyses using the proposed technique is not time consuming and simple for application. This implies that the proposed technique can be readily used for more complicated welded joints. It was also observed that the non-uniform stress distributions shown in Figs. 15, 21 and 24(b) demonstrate that the proposed technique is effective when a local stress concentration is applied to the crack face. The excellent accuracy (i.e. percentage difference < 1% between external loading solutions given by WARP3D-IIM and CFT-solutions at the crack deepest point) supports the adequacy of the proposed technique for the butt and T-butt welded joints. As well, the excellent agreement obtained between the proposed technique solution and Shiratori's solution suggests that the proposed technique can be used to evaluate the SIF for a surface crack in a real welding RS field.

4.4 Evaluation of SIF based on real welding RS

4.4.1 Introduction

In this section, the proposed technique was employed to evaluate SIF solutions for a semi-elliptical surface crack based on real welding RS. The welding RS used in this section was measured by the contour method that gives a 2-D map of RS distribution on the cutting surface. Gadallah et al.[76] measured welding RS produced due to the application of conventional and low transformation temperature (LTT) welds using the contour method. The 2-D maps of the longitudinal welding RS are shown in Fig. 4.26. In their work, Gadallah et al. used two different LTT wires. The first wire (LTT-1), see Fig. 4.26(b), has a martensitic transformation start temperature (T_{MS}) of 200–250 ^{o}C. The other LTT wire (LTT-2), see Fig. 4.26(c), has a T_{MS} of 150–200 ^{o}C. The welding RS measured by Gadallah et al. was employed in order to evaluate SIF based on real welding RS. The 2-D RS maps shown in Fig. 4.26 was taken at the cutting plane. From the 2-D RS map shown in Fig. 4.26(a), a tensile RS was introduced at the middle of the specimen including the welding zone and heat affected zone while a compressive stress was obtained at the specimen edges. This 2-D RS map represents a typical example of a welding RS distribution. On the other hand, the 2-D RS maps presented in Fig. 4.26(b) and 4.26(c) give a compressive RS in the welding zone that reveals the effectiveness of the LTT wires in reducing the tensile RS and introducing compressive RS. By placing a surface crack in this welding RS field, SIF can be evaluated in which the influence of the RS field is included in the SIF solutions by using the proposed technique.

4.4.2 FE model definition

The geometry of the butt welded joint used by Gadallah et al.[76] is shown in Fig. 4.27(a). The FE butt-welded model generated using the same dimensions of the welded joint in which a surface crack placed at the same location of the cutting plane, as shown in Fig. 4.27(b). The same procedures mentioned in sections 4.2.1 and 4.2.2 were followed when the FE model was generated. The crack-block generated using a fine mesh with a semi-elliptical surface crack with aspect ratios of a/c = 0.3 and a/t = 0.15. The crack-block then connected to the global mesh by the mesh tying option that available in WARP3D code. The surface crack placed at the welding zone (see Fig. 4.27(c)) in which the RS due to welding was applied to the crack face. Young's modulus, Poisson's ratio, and maximum stress (σ_o) employed in the analyses have values of 206 GPa, 0.291, and 300 MPa respectively, which represent typical properties for steel materials. The material properties used in the analyses are the same as those utilized by Gadallah et al.[76]. The rigid body motion of the FE cracked model was prevented by applying the minimum displacement constraints, as shown in Fig. 4.27(b).

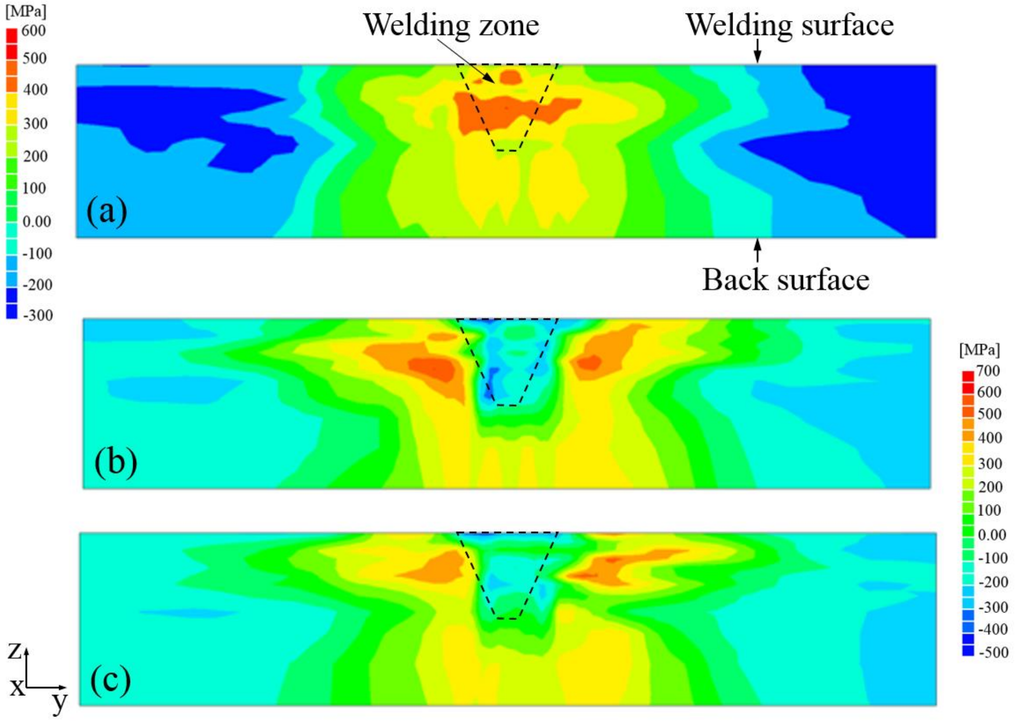

Fig. 4.26 Measured welding RS 2-D maps using the contour method[76]. (a) conventional weld wire, (b) LTT-1 weld wire, and (c) LTT-2 weld wire.

For the calculated welding RS, as discussed in section 4.3.3, the RS gave a smooth distribution over the crack face. However, for the case of real welding RS a dispersion of the RS distribution was obtained especially at the welding zone as shown in Fig. 4.26. To examine the influence of simplifying welding RS on the behavior of SIF, two cases for each weld wire were employed to evaluate SIF solutions based on: 1) actual welding RS, and 2) simplified welding RS. The technique used for simplifying the actual welding RS is discussed in more details in section 4.4.3. As well, to examine the SIF solutions obtained based on welding RS, SIF using mechanical loading (i.e. without welding RS) was calculated.

4.4.3 Welding RS data processing

There are numerous methods that used for simplifying (i.e. smoothing) data such as moving averages, weighted moving averages, centered moving averages and exponential smoothing. In

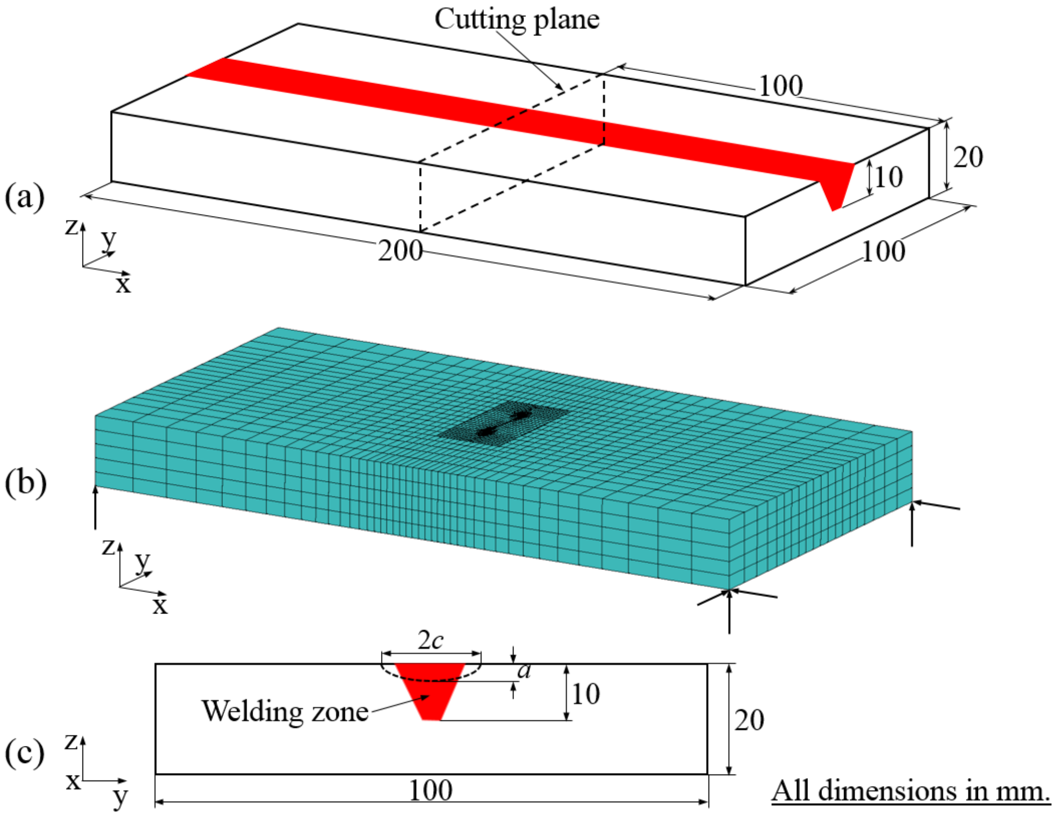

Fig. 4.27 Surface cracked butt-welded joint. (a) geometry of the butt welded joint used by Gadallah et al.[76], (b) FE butt-welded model with the boundary conditions, and (c) location of the surface crack in the welded joint. (Note: Fig. 4.27(c) taken at the cutting plane).

this study the exponential smoothing method was employed. The exponential smoothing methods are the most widely used forecasting methods due to its simplicity, its reasonable accuracy, its computational efficiency, and the ease of adjusting its responsiveness to changes in the process being forecast[77]. Exponential smoothing uses a simple average calculation to assign exponentially decreasing weights starting with the most recent observations. The simplest method of exponential smoothing is called the simple exponential smoothing that is appropriate for a series of data that moves randomly above and below a constant mean. The formal equation that used for the simple exponential smoothing takes the form of[77]:

$$F_{T+1} = \alpha q_T + (1-\alpha)F_T, \qquad T > 0 \tag{4.2}$$

where q_T is the actual, known series value at the time T ; F_T is the forecast value of the variable Q at the time T ; F_{T+1} is the forecast value at the time $T + 1$; α is the smoothing constant. In this study, a smoothing constant of 0.1 was utilized.

Since the simple exponential smoothing method is used for smoothing data with no trend and no seasonal pattern[77], the welding RS was only simplified for the dispersed regions (i.e. at the middle of the specimen), as shown in Figs. 4.28–4.30. Figures 4.28–4.30 show a comparison between the actual and simplified welding RS for the conventional weld wire, LTT-1 weld wire and LTT-2 weld wire, respectively. Each figure in Figs. 4.28–4.30 represents two RS line plots through the specimen thickness; one at the welding surface and the other at 3 mm from the welding surface. It is clear from Figs. 4.28–4.30 that the simple exponential smoothing method well simplified the actual welding RS at the middle region of the specimen.

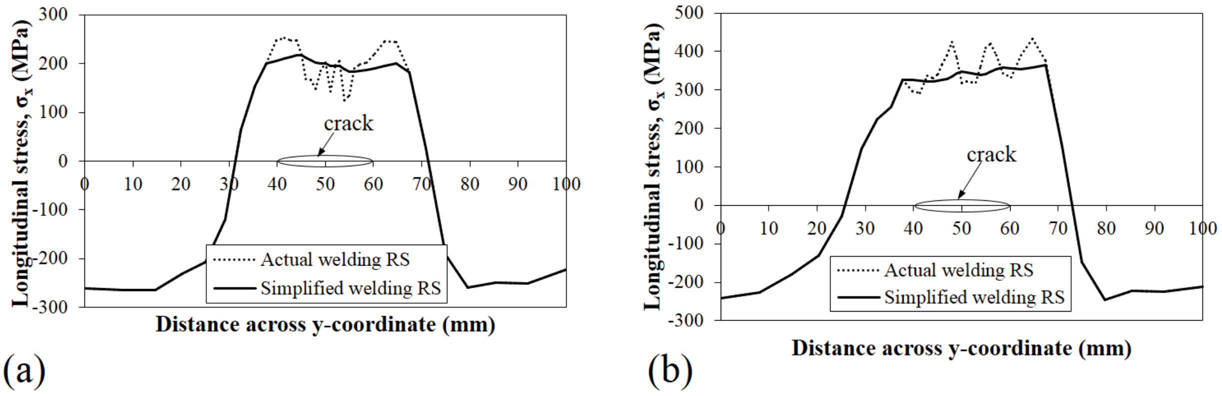

Fig. 4.28 Comparison of actual and simplified welding RS produced by conventional weld wire: (a) at welding surface and (b) at 3 mm from the welding surface.

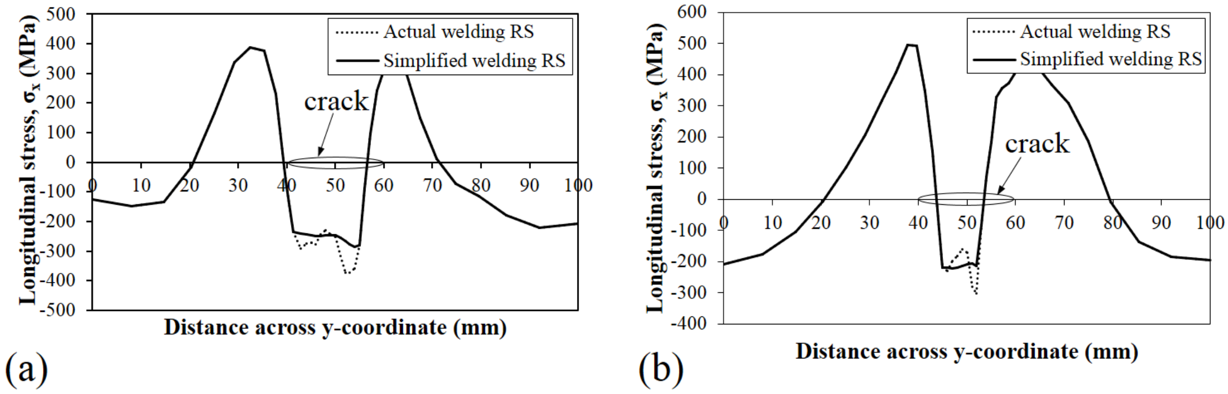

Fig. 4.29 Comparison of actual and simplified welding RS produced by LTT-1 weld wire: (a) at welding surface and (b) at 3 mm from the welding surface.

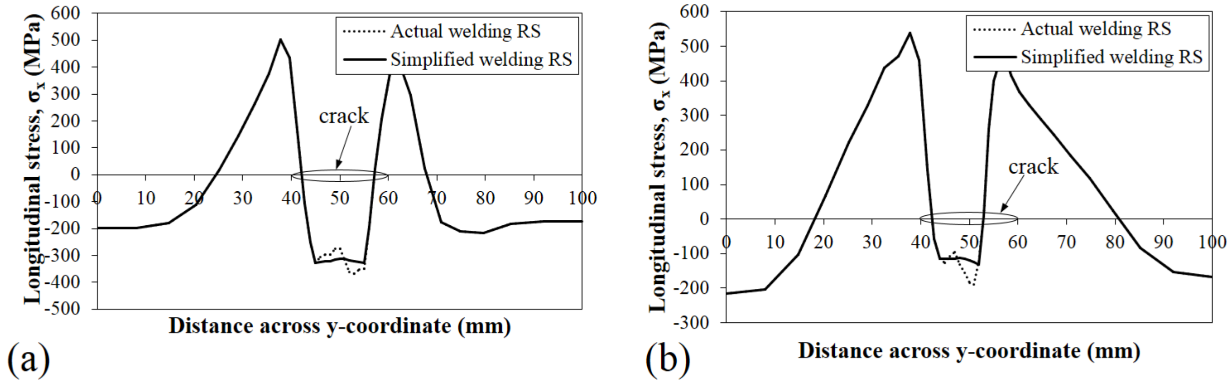

Fig. 4.30 Comparison of actual and simplified welding RS produced by LTT-2 weld wire: (a) at welding surface and (b) at 3 mm from the welding surface.

The actual welding RS, shown in Figs. 4.28–4.30, obtained by using the contour method at the cutting surface nodes[76]. However, in the proposed technique, the welding RS field should be applied to the center of each element face over the crack face not at nodes. Since the element size that faces the cutting surface is small enough (~0.1 mm) as well as the mesh of the cutting surface has a uniform element shape[76], thus stress can be directly calculated at the center of each element face over the cutting surface by taking the average of the stresses at corner nodes of each element face. Based on that, the actual and simplified welding RS were calculated at the center of each element face over the cutting surface by using the actual and simplified welding RS at nodes, respectively.

The welding RS (actual and simplified) at each element face over the region of the cutting surface, that corresponds to the crack face, was applied to each element face over the crack face. The distribution of welding RS over the crack face using the actual and simplified RS for each weld wire is shown in Figs. 4.31–4.33. It is clear from Figs. 4.31(a), 4.32(a) and 4.33(a) how the actual welding RS is randomly distributed over the crack face. However, Figs. 4.31(b), 4.32(b) and 4.33(b) give a simplified RS distribution over the crack face. The RS distributions shown in Figs. 4.31–4.33 reveal the adequacy of the simple exponential smoothing method in simplifying the actual RS in the dispersed regions. Figures 4.31–4.33 also reveal that the RS increases towards the crack front. The actual and simplified welding RS distributions shown in Figs. 4.31–4.33 were then utilized to evaluate the SIF based on the proposed technique, as discussed in section 4.4.4.

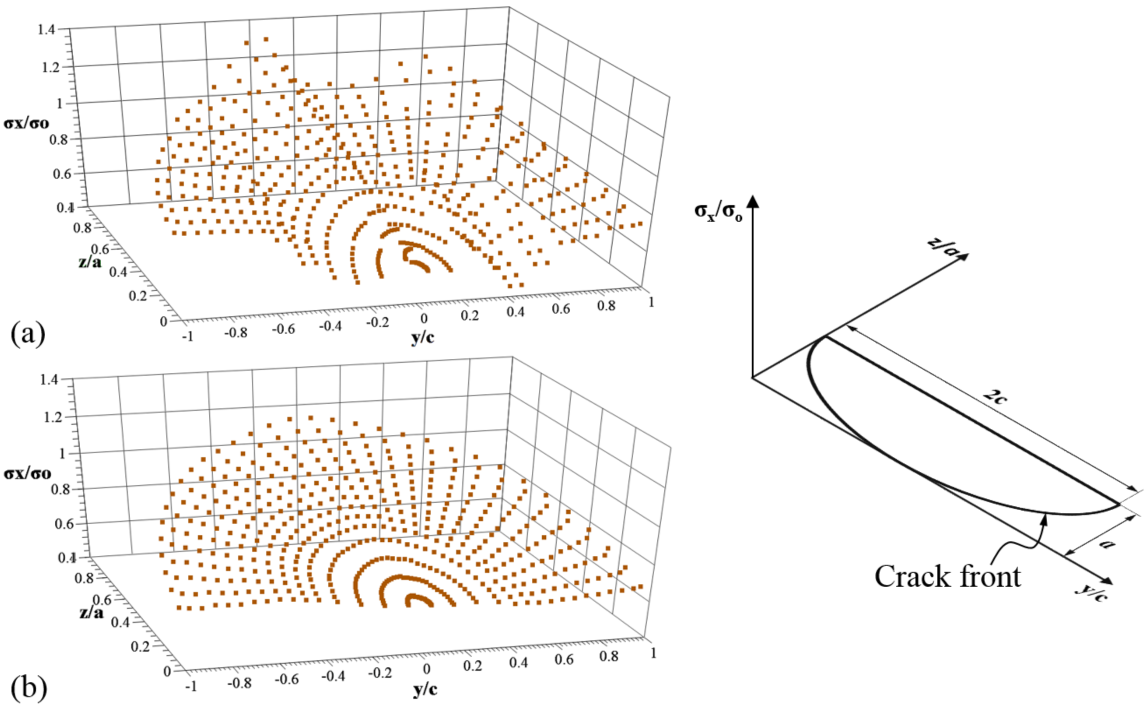

Fig.4.31 Welding RS distribution over the crack face produced by conventional weld wire. (a) actual welding RS, and (b) simplified welding RS.

4.4.4 Results and discussion

Although the adequacy of the proposed technique was validated in section 4.3.3 by using the calculated welding RS; however, it is needed to verify the distribution of the calculated SIF solutions when a real welding RS is employed. Thus, SIF was calculated without considering welding RS (i.e. external mechanical loading applied at the model boundary) for the conventional weld wire case using the same FE butt welded model with the same displacement boundary conditions as shown in Fig. 4.27(b). The SIF was calculated under external mechanical loading in order to evaluate the deviation (i.e. accuracy) of the SIF solution obtained by welding RS as tractions over the crack face. The same procedures that applied in section 4.3 in order to obtain SIF under external loading were followed in this section to calculate the SIF due to mechanical loading. The mechanical loading has a value of 300 MPa (maximum stress,σ_o); and applied as uniform external tensile loading at the model boundary. On the other hand, the proposed technique was employed to evaluate SIF solutions based on the real welding RS (actual and simplified) for the different weld wires.

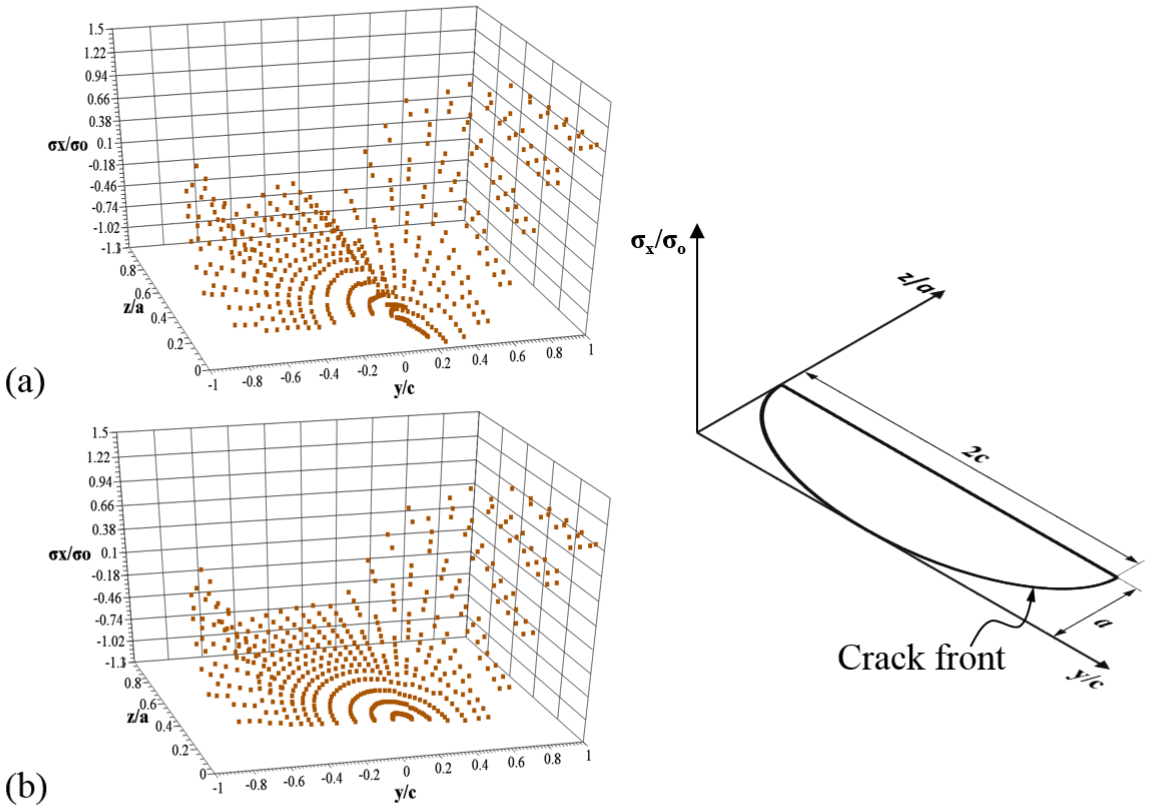

Fig.4.32 Welding RS distribution over the crack face produced by LTT-1 weld wire. (a) actual welding RS, and (b) simplified welding RS.

The distributions of SIF solutions of the conventional weld wire along the crack front that obtained by the actual and simplified welding RS as well as mechanical loading (i.e. without welding RS) are shown in Fig. 4.34. Note that the crack mouth is represented at $2\varphi/\pi = 0$ and 2 while the crack deepest point is represented at $2\varphi/\pi = 1$. The SIF solutions obtained by welding RS show a reasonable agreement with the solution given by mechanical loading. It is clear from Fig. 4.34 that a large SIF was obtained at the crack deepest point and small one was given at the crack mouth locations. As it is observed from Fig. 4.26(a), the tensile RS increases when move away from the welding surface towards the specimen thickness direction (in the region of the crack face). The same trend was also noticed in Fig. 4.31. And since the surface crack placed at the weld line (see Fig. 4.27(c)), so it is clear that the RS field that applied to the region close to the crack front (crack deepest point) is larger than that applied to the crack mouth locations (see Fig. 4.31). Based on that, the distributions of the SIF solutions obtained by welding RS, shown in Fig. 4.34, agree well with the distribution of the measured RS stress. In other words, a small SIF was given at the crack mouth locations; however, a large one was obtained at the crack deepest point and this matches well with the distribution of welding RS (Fig. 4.31). As well, the distribution of the SIF solution given by the mechanical loading followed the same behavior of the SIF solutions obtained by the welding RS.

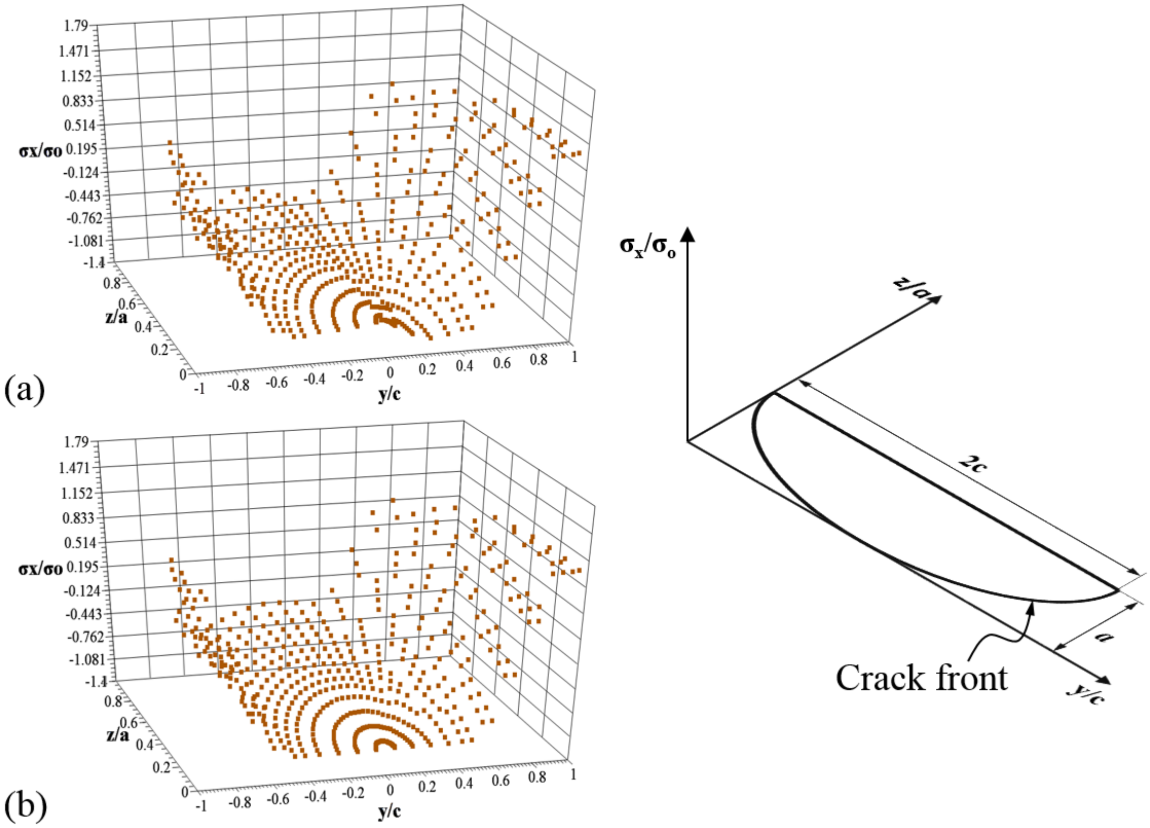

Fig.4.33 Welding RS distribution over the crack face produced by LTT-2 weld wire. (a) actual welding RS, and (b) simplified welding RS.

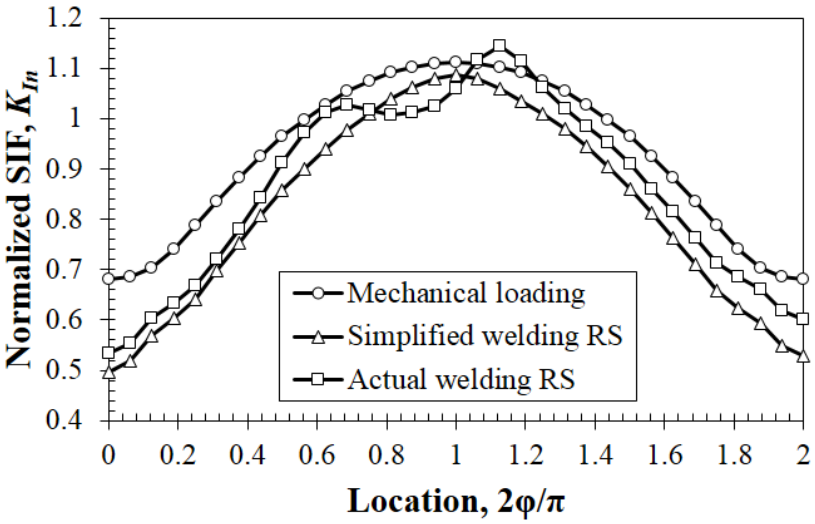

Fig. 4.34 Distribution of the normalized SIF along the crack front calculated based on real welding RS and mechanical loading (without welding RS) for a butt-welded joint using a conventional weld wire.

The SIF solution given by the simplified welding RS showed a smooth distribution along the crack front as well as a slight asymmetry was observed at the crack mouth locations. This demonstrates the efficiency of the applied smoothing method on the calculated SIF. On the other hand, the SIF solution obtained due to the application of the actual welding RS showed a clear asymmetry especially around the crack deepest point. This asymmetry is due to the dispersion of the RS distribution at and close to the crack front, as shown in Fig. 4.31(a). This asymmetry also reveals that some regions of the crack front may propagate faster than others. This solution (i.e. SIF due to actual welding RS) gave a realistic distribution of the SIF and showed the critical regions along the crack front that may propagate faster. In addition, the SIF solution obtained by the simplified welding RS showed that the crack will propagate starting from the deepest point. However, for the case of the actual welding RS, the crack will not propagate exactly from the deepest point but from a point close to the deepest point. As well, the distribution of SIF given by the actual welding RS revealed that the crack will propagate in an irregular form especially around the deepest point.

Furthermore, the SIF obtained by the simplified welding RS at the crack deepest point showed a good agreement with that given by the mechanical loading in which a percentage difference of 2.32% was obtained between the two solutions. However, the percentage difference between the SIF solutions given by the actual welding RS and mechanical loading at the deepest point increased to be 4.80%. This difference may be due to the irregular SIF distribution obtained by the actual welding RS around the crack deepest point. On the other hand, the SIF solutions calculated due to the application of the actual and simplified welding RS gave a percentage difference of 2.52% at the crack deepest point. In general, a good agreement was obtained between the SIF solutions at the crack deepest point, as shown in Fig. 4.34.

On the other hand, the SIF distribution along the crack front for the two LTT weld wires is shown in Fig. 4.35. Note that the crack mouth is defined at $2\varphi/\pi = 0$ and 2 while the crack deepest point is defined at $2\varphi/\pi = 1$. It is clear from Fig. 4.35 that a negative SIF was obtained at the weld zone. The results given in Fig. 4.35 agree well with the welding RS distributions shown in Fig. 4.26(b) and (c) in which compressive RS that produced due to the application of LTT weld wires introduced negative SIF. Further, due to simplification of welding RS smooth SIF solutions were obtained; however, the actual welding RS gave irregular SIF distributions. The SIF solutions did not show a clear difference between the actual and simplified welding RS in the outer regions (i.e. $1.2 \leq 2\varphi/\pi \leq 0.8$) of the crack front and this agrees well with Figs. 29, 30, 32 and 33. For the LTT weld wires, the simplified welding RS regions are smaller than those of the conventional weld wire. So that, no big change in the SIF solutions that obtained by the actual and simplified welding RS was observed at the outer regions of the crack front. From Fig. 4.35, it is clear that some regions of the crack front subjected to positive SIF and others subjected to negative one. This means that, the crack in this situation will propagate with an irregular shape where some regions will propagate faster than others. In addition, the SIF solutions obtained by the actual welding RS show that the crack will not propagate starting from the crack deepest but from another point that has a larger SIF magnitude. For example, the crack may propagate starting from the region close to crack mouth at $2\varphi/\pi = 0$. From the results shown in Fig. 4.35, some regions of the crack will be closed due to the negative SIF and this may improve the fatigue life of the cracked component. Where the negative SIF will play the role of minimizing the driving force to deaccelerate the crack propagation.

To show the influence of the welding RS on the calculated SIF behavior, Fig. 4.36 shows a comparison of the SIF distribution along the crack front for the conventional, LTT-1 and LTT-2 weld wires. Figure 4.36 illustrates the influence of the simplification of welding RS on the SIF behavior. It is found that by simplifying welding RS, the behavior of SIF changes that may influence the accuracy of fatigue life evaluation, which relies on the calculated SIF. Therefore, the actual welding RS distribution is highly recommended to be used to obtain accurate and realistic SIF solution that may improve the accuracy of fatigue crack propagation evaluation. Moreover, the LTT weld wires demonstrate that negative SIF may be obtained because of the induced compressive RS. As well, the influence of the induced welding RS (i.e. tensile or compressive) was demonstrated in which, for the same crack size, the crack may propagate (i.e. for tensile RS) or close (i.e. for compressive RS) at some regions along the crack front.

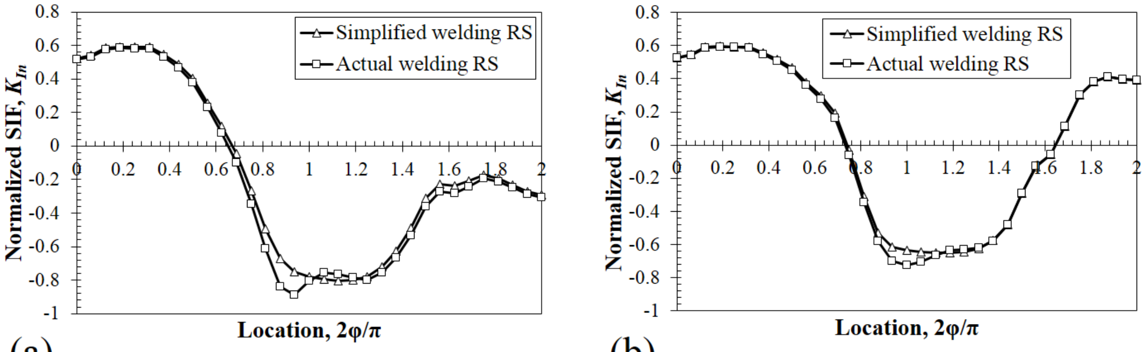

(a) (b)

Fig. 4.35 Distribution of the normalized SIF along the crack front calculated based on real welding RS for a butt-welded joint. (a) LTT-1 weld wire and (b) LTT-2 weld wire.

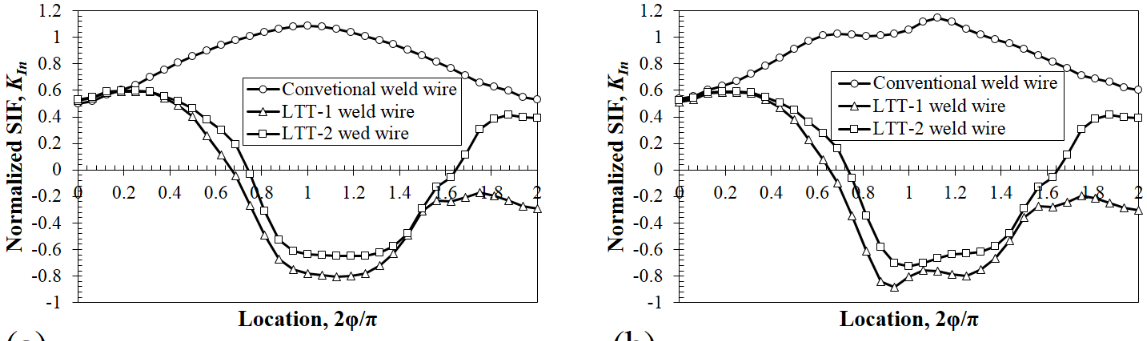

(a) (b)

Fig. 4.36 Comparison of the normalized SIF along the crack front. (a) simplified welding RS and (b) actual welding RS.

4.5 Summary

In this chapter, a technique was proposed to evaluate SIF for semi-elliptical surface cracks in welding RS fields based on WARP3D-IIM. The influence of the crack-block mesh density on the accuracy of the SIF solutions was examined under different loading conditions. The proposed technique was then validated using different numerical FE examples under different loading conditions. The SIF was thereafter evaluated for a surface cracked butt-welded joint based on real welding RS. Based on the analyses results, the following conclusions can be drawn:

1) The proposed technique mainly based on two main points: a) utilizing the CFT-integral implemented in WARP3D-IIM, and b) using a particular crack-block mesh density.

2) The crack-block mesh density showed a significant influence on the calculated CFT-solutions along the crack front under different loading conditions. It was observed that when the crack-block mesh becomes fine enough (e.g. $a_1/a \leq 0.06$), the smoothness and accuracy of the CFT-solutions are improved. Thus to take the advantage of the CFT-integral implemented in WARP3D-IIM and to improve the accuracy of the CFT-solutions, a fine crack-block mesh must be utilized in the FE cracked models.

3) Although the CFT-integral that implemented in WARP3D-IIM is limited only for a uniform distributed stress field; however, when a fine crack-block mesh is used the same CFT-integral can be utilized to evaluate SIF for surface cracks in non-uniform stress fields.

4) The results of the different FE examples examined in this chapter showed an excellent agreement between the CFT-solutions and those given by external loading along the crack front especially at the crack deepest point based on the proposed technique.

5) By using the proposed technique, a percentage difference of less than 1% was obtained at the crack deepest point between the CFT-solution and that given by external loading for all the numerical examples studied in this chapter.

6) The proposed technique was validated for a butt-welded joint using a calculated welding RS. The SIF solutions calculated by the proposed technique gave excellent agreement along the crack front with those obtained by the reference solution (Shiratori's solution).

7) The proposed technique was employed to calculate SIF along the crack front for a surface cracked butt-welded joint based on real welding RS. The SIF solutions calculated by real welding RS showed a good agreement with the solution obtained by mechanical loading. As well, negative SIF solutions were obtained when a compressive welding RS was used.

8) Simplification of welding RS has a clear influence on the behavior of SIF. Therefore, actual welding RS distribution is highly recommended to be used in order to obtain accurate and realistic SIF solutions.

9) The SIF solution obtained by actual welding RS gave an interesting distribution especially around the crack deepest point. This distribution introduced a realistic SIF behavior and showed that some regions of the crack front may propagate faster than others.

10) A percentage difference of less than 4% was obtained at the crack deepest point between the CNT-solutions and those calculated by external loading using MSC Marc-DI for the studied numerical examples under different loading conditions. Thus, commercial FE codes that omit the CFT-integral can be utilized for rough estimation of SIF for surface cracks in non-uniform stress fields for engineering problems under the conditions examined in this chapter.

CHAPTER 5

Application to fatigue life evaluation based on the proposed technique

5.1 Introduction

Many of welded structures subject to external cyclic loadings, therefore the presence of welding RS in these structures can considerably deteriorate the fatigue life. So that, the prediction of welding RS is a vital task. However, due to the complexity of welding process that includes localized heat, non-uniform temperature distributions, moving heat source and temperature dependence material properties, accurate and effective methods are needed to predict welding RS. Therefore, the FEM has emerged a robust tool for the prediction of welding RS[78]. A large number of thermo-mechanical FE simulations, until now, have been conducted to predict welding RS for different welded joints[79][80][81][82].

Recently, some researchers studied the fatigue crack propagation (FCP) behavior of welded joints considering welding RS. Tra et al.[83] discussed the behavior of FCP in friction stir welded joint including the roles of RS and microstructure. Lee et al.[78] investigated the behavior of high cycle fatigue of T-welded joint including welding RS based on continuum damage mechanics. They reported that welding RS cannot be neglected in an estimation of fatigue life of welded joints. The influence of the initial crack orientation and the distance of the notch tip on FCP in a welding RS field was studied by Vaidya et al[84]. In addition, Mikkola et al.[85] assessed the fatigue life of high-frequency mechanical impact treated welded joints subjected to high mean stresses and spectrum loadings. Furthermore, Ngoula et al.[81] and Rettenmeier et al.[82] addressed the influence of welding RS on FCP of different welded joints. They found that the influence of welding RS can be disregarded for large load amplitudes. On the other hand, Hemmesi et al.[80] estimated the torsional fatigue of tubular joint considering the influence of welding RS using the critical plane approach. Although these research works studied the role of welding RS on the FCP behavior; however, the influence of the change in welding heat input (HI) on the behavior of SIF and FCP has not well studied. It is therefore necessary to study the impact of the change in welding HI on the behavior of SIF and FCP. This may give a good understanding to the relation between welding HI and welding RS and their influence on the behavior of SIF and fatigue life of welded joints.

This chapter aimed to investigate the influence of the change in welding HI and the induced welding RS on the behavior of SIF and FCP for a bead-on-plate (BOP) model. For the sake of comparison, additional case without welding is utilized to reveal the influence of both the change in welding HI and welding RS on the behavior of SIF and FCP. To simulate the welding process, a thermal-elastic-plastic (TEP) FEA is conducted firstly to examine the impact of the change in welding HI on the induced welding RS. The proposed technique in chapter 4, thereafter, is employed to calculate SIF solutions considering welding RS resulting from the applied welding HI cases under different constant stress amplitude loadings. Moreover, measured semi-elliptical surface cracks are used in which the surface cracks are placed at the weld toe. The estimated SIF solutions are then employed in calculating fatigue lives considering the change in welding HI represented in welding RS. On the other hand, to verify the adequacy of the applied welding simulations as well as the effectiveness of the proposed technique, the calculated fatigue lives are compared with simulated and experimental data.

5.2 Thermal-elastic-plastic analysis

5.2.1 Problem definition

Different welding HI cases were applied, in this study, using a BOP FE model in order to examine the influence of the change in welding HI on the behavior of welding RS, SIF and FCP. As well, one additional case without welding was adopted to investigate the influence of welding RS on the behavior of SIF and FCP. Therefore, three welding cases as well as one case without welding were discussed in this chapter. The details of the studied cases are shown in Table 5.1. The high welding HI case based on the welding conditions that used in experiments by Kusuba[86]. Welding conditions used in experiments are as follows: welding current = 120 A, arc voltage = 23 V and welding speed = 150 mm/min using shielded metal arc welding process. The low and moderate welding HI cases were conducted to study the influence of the change in welding HI on the behavior of SIF and FCP. Note that, one-half of the welding HI given in Table 5.1 was used in the analysis because only one-half FE model was employed.

5.2.2 FE model definition

The BOP FE model employed in this study was adopted as used by Kusuba[86]. In Kusuba's work, various BOP specimen types (type A, B and C) were conducted. In this chapter, however, only one specimen type (type B) was employed. Due to symmetry about the longitudinal axis of the BOP specimen, only one-half FE model was utilized. In the present study, two different FE models were employed; the first model used for TEP analysis which is called TEP FE model and the other one used for fracture analysis which is called cracked FE model. A very fine mesh used in TEP FE model in the region from the weld toe to 2 mm in depth to overcome singularity when applying the simulated welding RS obtained by the TEP FE model to the cracked FE model. The BOP geometry details and TEP FE model are shown in Figs. 5.1 and 5.2, respectively. The bead height and length are 3.74 mm and 100 mm, respectively. The TEP FE mesh generated by Patran software using 8-noded hexahedral elements. The boundary conditions used for welding simulation are represented by arrows in Fig. 5.2 in addition to the plane of symmetry is fixed in y-direction. These boundary conditions were only employed to prevent the rigid body motion.

Table 5.1 Studied cases and their heat inputs and average temperatures.

Case	Welding HI[a)] (KJ/mm)	Average temperature (°C)
No welding	--	--
Low welding HI	0.44	276.2
Moderate welding HI	0.58	345.6
High welding HI	0.72	415.8

[a)] Welding heat inputs given in this table are for one-half FE model.

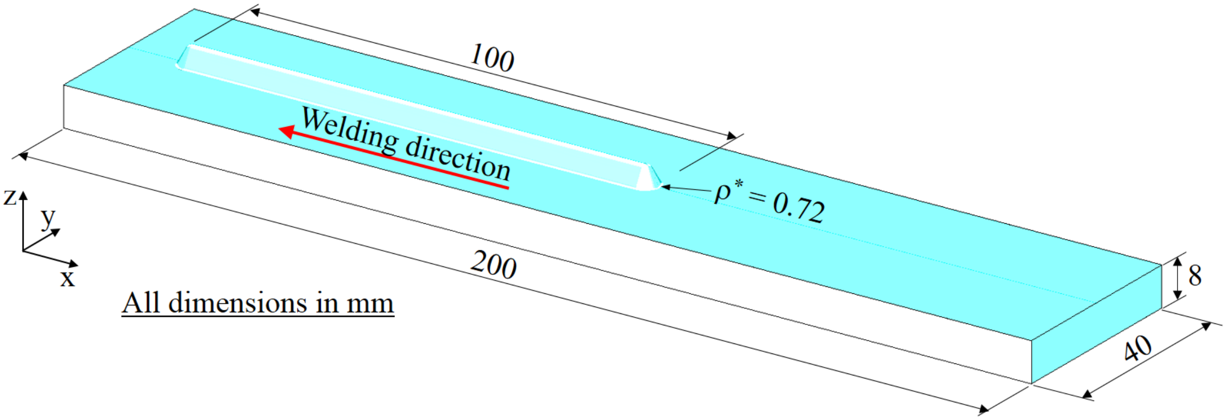

Fig. 5.1 Geometry of the applied BOP specimen.

5.2.3 Welding simulation

To perform TEP analysis for the three welding cases mentioned in Table 5.1, a sequentially coupled thermal and mechanical FEA was conducted using an in-house TEP FE program (JWRIAN)[87][88][89]. JWRIAN employs the iterative substructure method[90]. This approach aims to reduce the computation time by dividing the model into regions which are linear or weakly non-linear and those which are highly non-linear[89] where the temperature is higher than 300 °C, for example. JWRIAN also employs an iterative approach that used to ensure the continuity of tractions between linear and nonlinear regions. The TEP behavior is simulated using a sequentially coupled formulation in which thermal analysis is performed firstly to solve for thermal profiles. Subsequently, stress analysis is conducted which uses temperature profiles and solves for displacement, strain and stress. The temperature dependent thermal-physical properties as well as temperature dependent mechanical properties used in the TEP analysis are shown in Fig. 5.3.

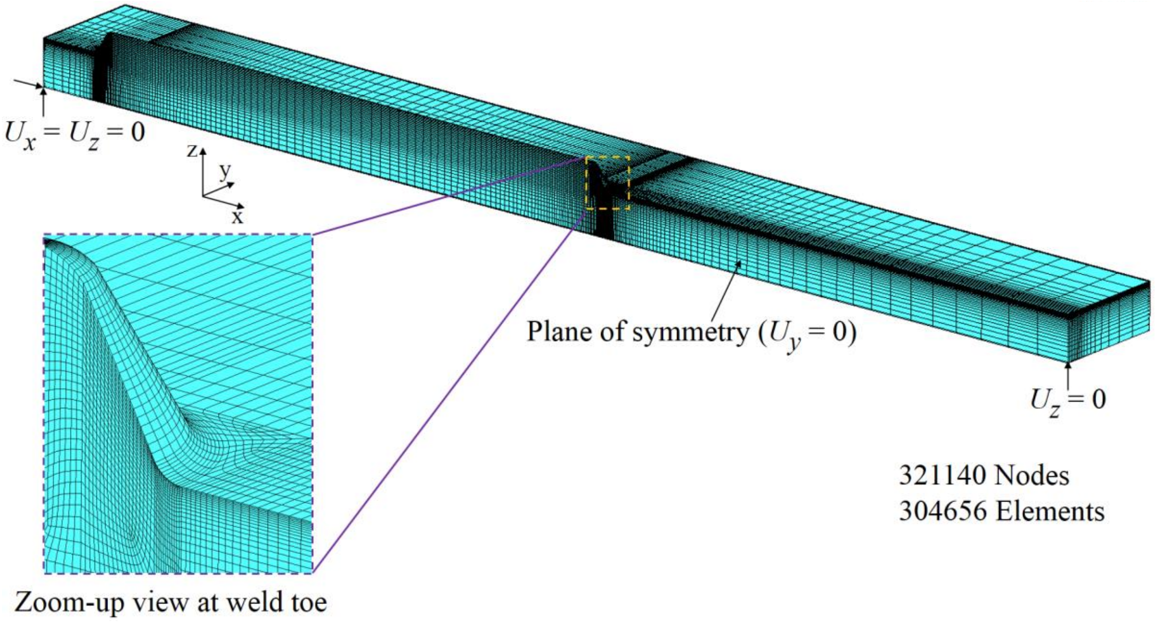

Fig. 5.2 Typical one-half symmetric TEP FE model with the boundary conditions.

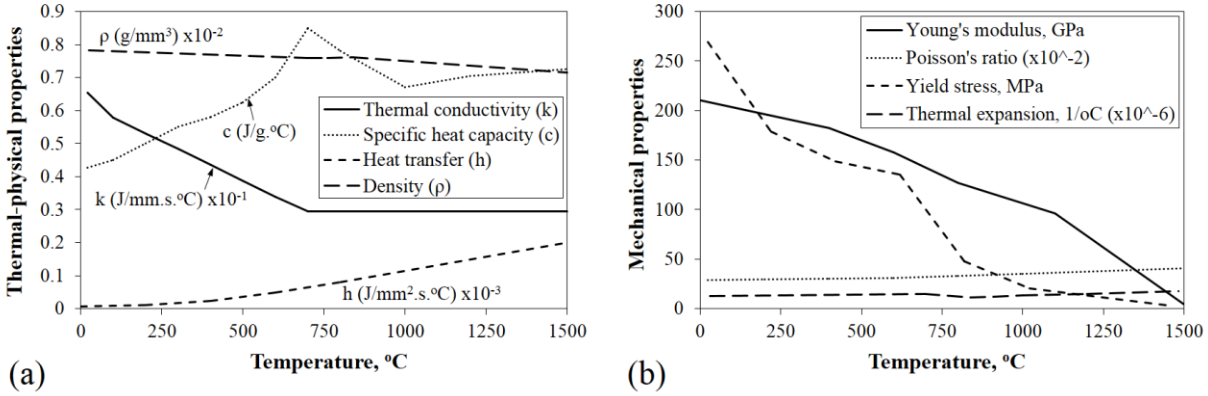

Fig. 5.3 (a) Temperature-dependent thermal-physical properties used in TEP analysis. (b) Temperature-dependent mechanical properties used in TEP analysis.

5.2.4 Influence of the change in welding HI on welding simulation results

The influence of the change in welding HI on welding penetration is shown in Fig. 5.4. The case without welding (Fig. 5.4(a)) was used only for the sake of comparison. From the results shown in Fig. 5.4, it is clear that by increasing the welding HI the welding penetration also increases. Note that the dotted line in Fig. 5.4 represents the fusion line.

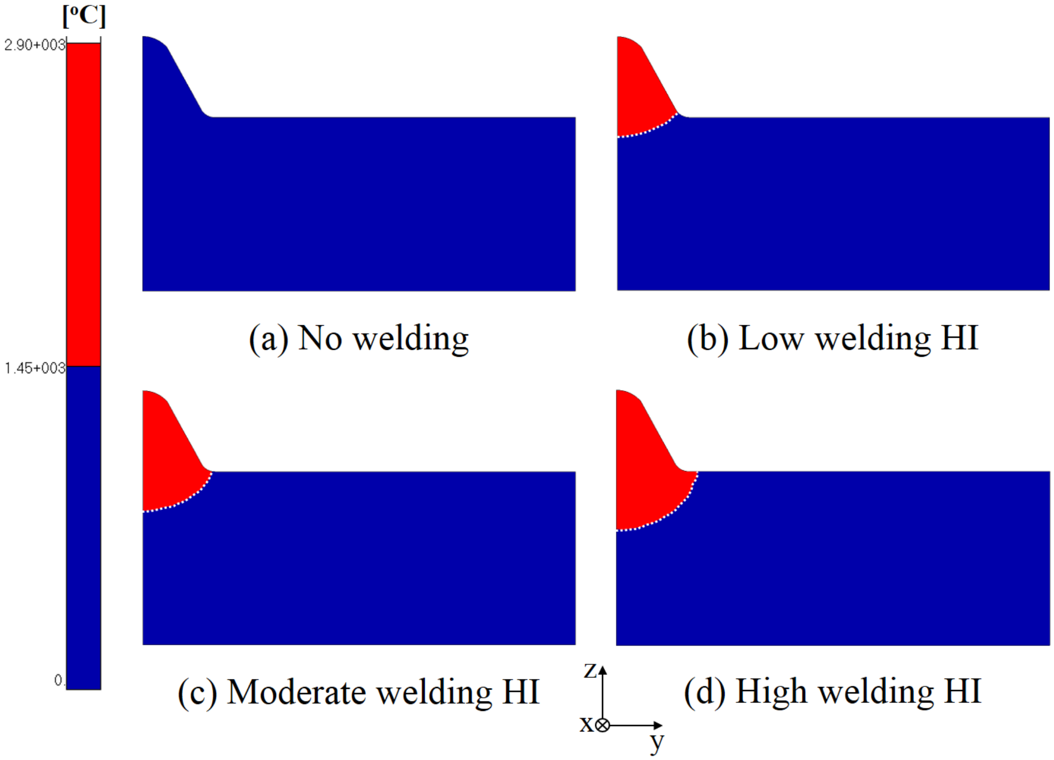

(a) No welding

(b) Low welding HI

(c) Moderate welding HI

(d) High welding HI

Fig. 5.4 Influence of the change in welding HI on welding penetration. Note that the welding penetration profiles taken at the mid-length of the weld bead. In addition, the case of no welding is presented for the sake of comparison in which the temperature of this case represents the room temperature.

The average temperature for each welding HI case is given in Table 5.1. Since the size of the FE model is small (i.e. width direction), so the obtained average temperature is high, in general. Furthermore, by increasing the welding HI the produced average temperature increases as well, where the cross-section of the FE model (y-z plane) is fixed. In addition, the change in welding HI reveals a clear influence on the resulting distortion. The magnitude of welding distortion obtained by low, moderate and high welding HI cases is 0.81 mm, 1.09 mm and 1.27 mm, respectively. It is clear that as the welding HI increases the produced distortion increases as well. The distortion obtained by high welding HI case is larger than that given by low welding HI case by 36.5% and the distortion produced by high welding HI case is larger than that given by moderate welding HI case by 14.2%. The distortion distribution of the three welding cases is shown in Fig. 5.5.

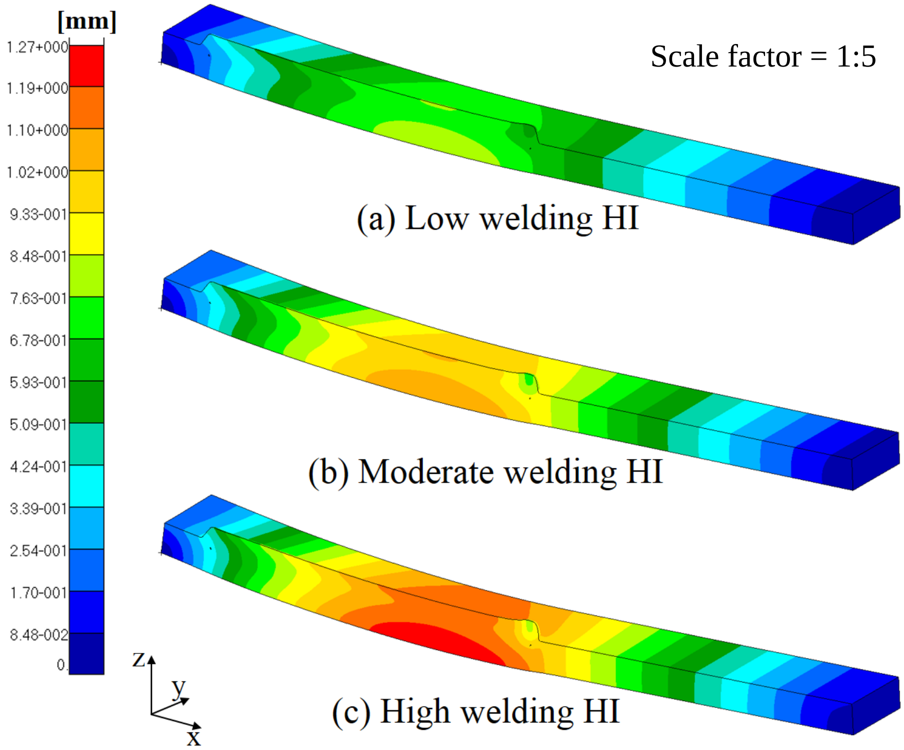

Fig. 5.5 Welding distortion distribution of the three welding cases.

On the other hand, Figs. 5.6 and 5.7 show the variation in von Mises stress distribution and stress distribution in longitudinal direction, respectively, due to the change in welding HI. From Figs. 5.6 and 5.7, it is clear that when the welding HI increases the induced welding RS decreases especially around the weld toe. The reason why this occurs is due to the average temperature of each welding HI case. When the average temperature becomes higher, the restraint of the model becomes smaller; and this leads to obtain smaller welding RS. Therefore, the predicted welding RS for each welding HI case agrees well with the calculated average temperature. It is observed that the welding RS obtained by the low welding HI case (see Fig. 5.6(a) and Fig. 5.7(a)) that gives the lowest average temperature is larger than that computed by the high welding HI case (see Fig. 5.6(c) and Fig. 5.7(c)) that shows the highest average temperature. Moreover, Fig. 5.6 describes that maximum welding RS located at the weld toe (as stress concentration region). As well, the welding RS shown in Fig. 5.7 gives a typical RS distribution in which a large tensile RS obtained at the weld toe and compressive one at the model’s edge.

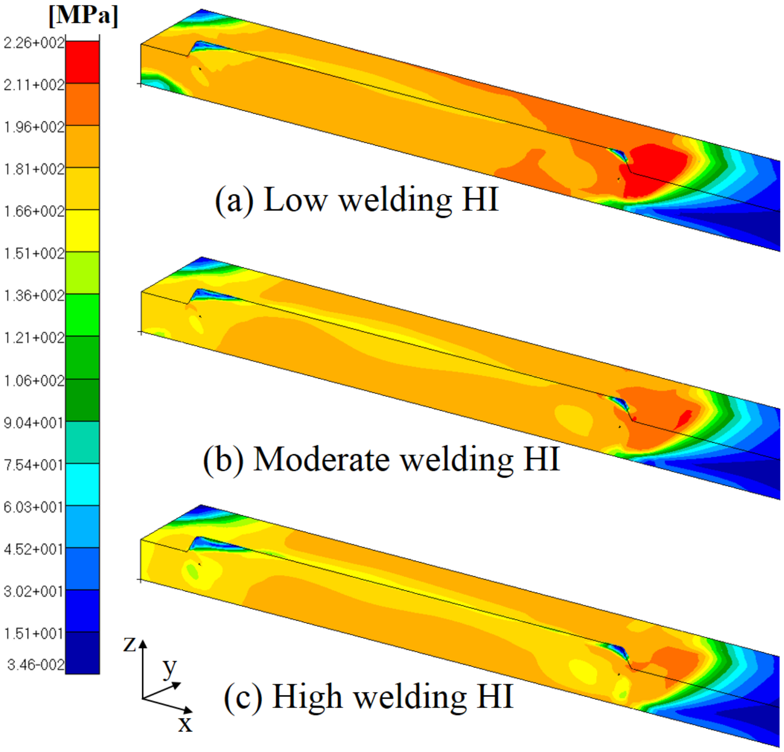

Fig. 5.6 Influence of the change in welding HI on von Mises stress distribution.

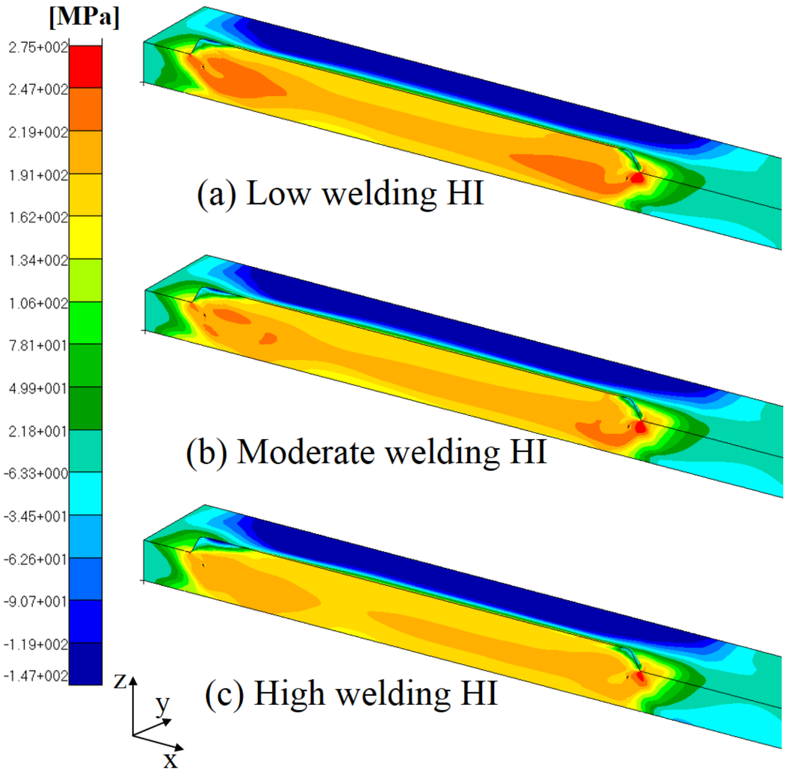

Fig. 5.7 Influence of the change in welding HI on the longitudinal RS distribution.

In this study, surface cracks were placed at the weld toe in order to study the influence of the change in welding HI on the behavior of SIF and FCP. It is therefore necessary to examine the welding RS distribution for each welding HI case where surface cracks exist. Figure 5.8 shows 2-D maps of the welding RS in the longitudinal direction taken at the weld toe where this is the location of the surface cracks as shown in Fig. 5.8(d). Results presented in Fig. 5.8(a–c) show how welding RS distribution is influenced significantly by the change in welding HI. The four dotted lines in Fig. 5.8(a–c) represent semi-elliptical surface cracks with the actual size placed at the weld toe. The four surface cracks are measured cracks and taken from Kusuba[86], further details on the measured cracks are given in the fracture analysis section. The purpose of plotting the four surface cracks on the welding RS 2-D maps is to show the variation of the welding RS field over each crack face for each welding HI case.

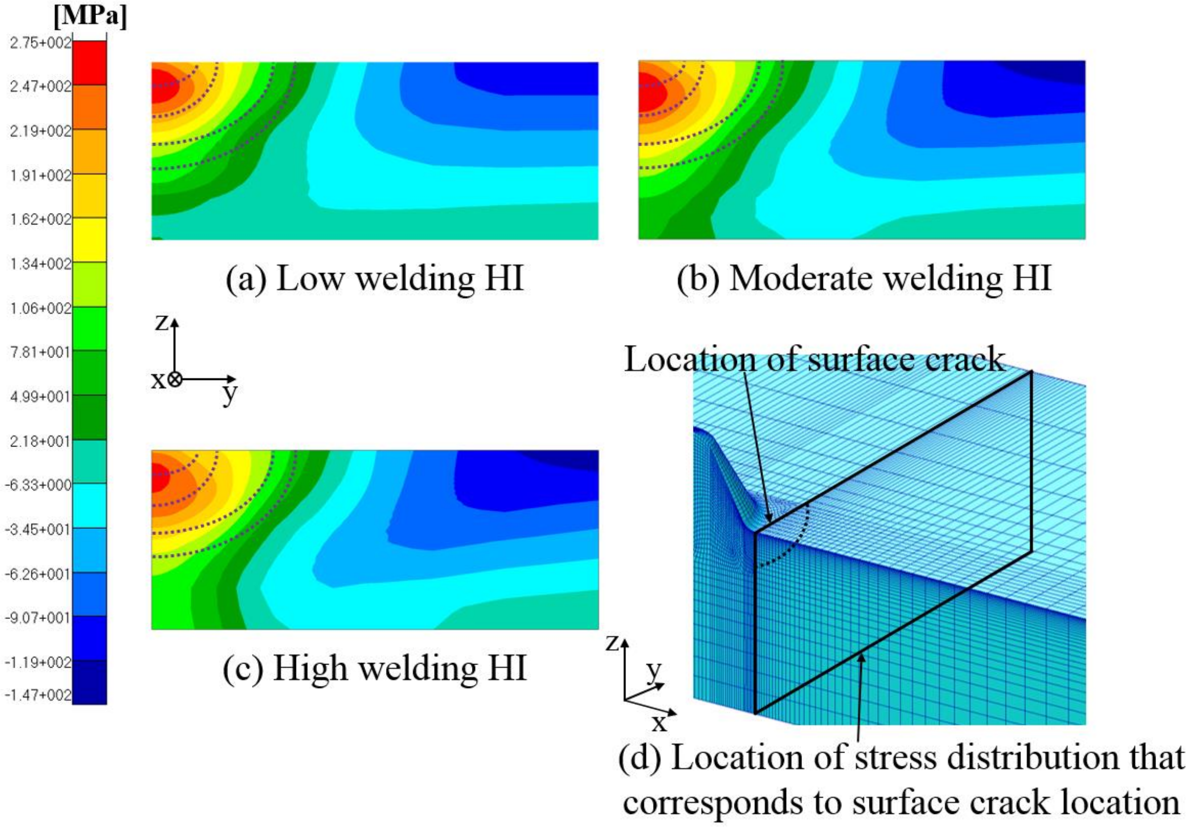

(a) Low welding HI

(b) Moderate welding HI

(c) High welding HI

(d) Location of stress distribution that corresponds to surface crack location

Fig. 5.8 Influence of the change in welding HI on 2-D maps of longitudinal RS distribution including measured semi-elliptical surface cracks. Note that the 2-D maps are taken at the weld toe.

From the results shown in Figs. 5.4–5.8, it is observed that the change in welding HI has a significant impact on welding penetration, average temperature, welding distortion and welding RS distribution.

5.3 Fracture analysis

In this section, the influence of the change in welding HI as well as the influence of welding RS on the behavior of SIF solutions is discussed. For this purpose, semi-elliptical surface cracks were placed at the weld toe. To analyze a surface crack in a welding RS field, the influence of welding RS field can be included in SIF solution by applying RS as tractions over the crack face according to the superposition principle. The proposed technique presented in chapter 4 was employed to evaluate the SIF solutions for the three welding cases as well as the case without welding under constant amplitude loading conditions.

5.3.1 Cracked FE model definition

As mentioned previously, two FE models were employed one for TEP analysis and the other for fracture analysis. The cracked FE model used in fracture analysis is shown in Fig. 5.9(a) and it consists of two parts, namely, crack-block mesh and global mesh. One-half FE model was used in the analysis because of the symmetry about the longitudinal axis. The crack-block mesh generated with a semi-elliptical surface crack with 20-noded isoparametric hexahedral brick elements. Generally, fatigue cracks in non-uniform stress fields (e.g. welding RS) propagate with an irregular shape[71]. However, for the sake of simplicity, semi-elliptical surface cracks were employed in this study. A fine crack-block mesh was utilized based on the information mentioned in chapter 4. To simulate the $1/\sqrt{r}$ singularity of the stress field near the crack tip, the 20-noded hexahedral elements are collapsed to quarter point wedge elements along the crack tip. The crack face FE mesh and crack tip of the crack-block mesh are shown in Fig. 5.9(b). On the other hand, the global mesh generated with 20-noded hexahedral elements using Patran software. The crack-block mesh then connected to the global mesh using the mesh-tying option available in WARP3D code in which the surface crack placed at the weld toe as shown in Fig. 5.9(a).

The SIF solutions were calculated for the four cases shown in Table 5.1 using ten semi-elliptical surface cracks. Four of the applied surface cracks (see the cracks plotted in Fig. 5.8(a–c)) were measured by Kusuba[86]. Further information on the measured cracks is shown in Table 5.2. The other cracks that used for fitting the FCP curve were linearly interpolated based on the measured cracks (i.e. based on aspect ratio of the measured cracks). The loading and boundary conditions that employed in fracture analysis are shown in Fig. 5.10. The loading and boundary conditions shown in Fig. 5.10 are the same as those used by Kusuba[86]. Note that, for the sake of simplicity, the influence of welding distortion was not included in the SIF and FCP estimation. However, in real situation (i.e. experiments); the influence of welding distortion is included in the measured FCP data. Young's modulus and Poisson's ratio employed in the analysis have values of 206 GPa and 0.3 respectively, which represent typical properties for steel materials. The material properties used in the analysis are the same as those adopted by Kusuba[86].

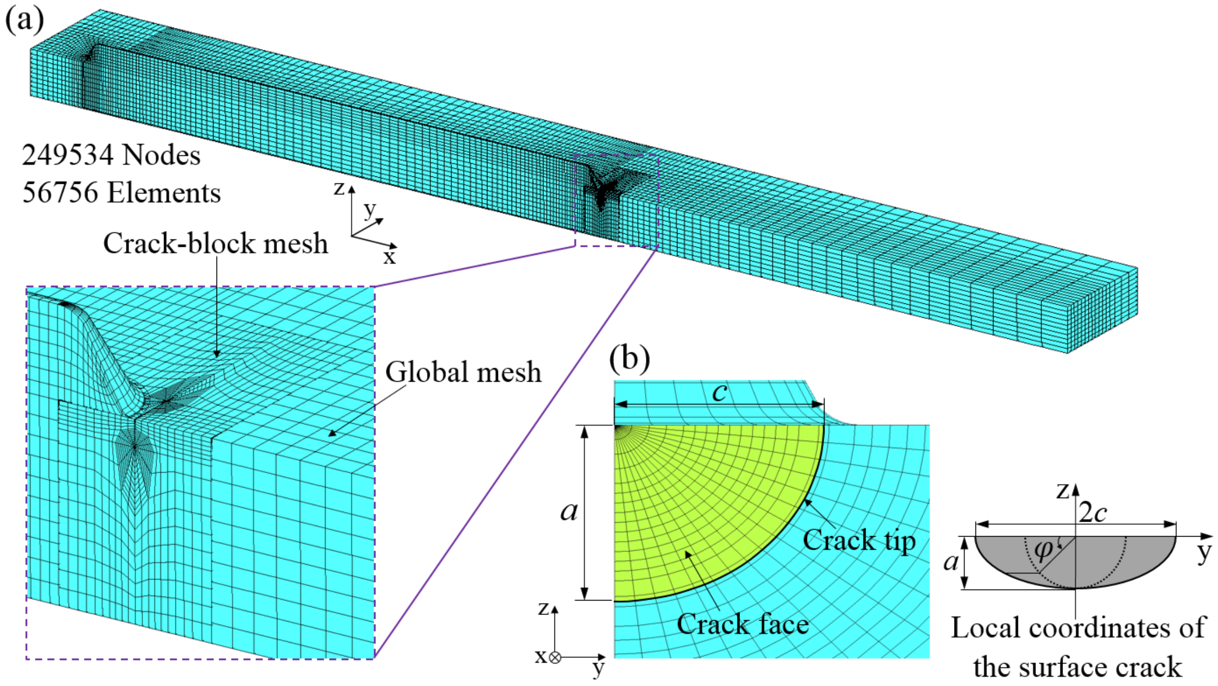

Fig. 5.9 (a) Typical one-half symmetric cracked FE model. (b) Crack face FE mesh and crack front.

Table 5.2 Details of the measured surface cracks used in the fracture analysis[a)].

Crack no.	Crack size		Aspect ratio	
	a (mm)	c (mm)	a/t	a/c
1	1.1	2.1	0.14	0.52
2	2.4	2.85	0.30	0.84
3	3.7	5.4	0.46	0.69
4	4.7	6.35	0.59	0.74

[a)] The measured cracks taken from Kusuba[86]

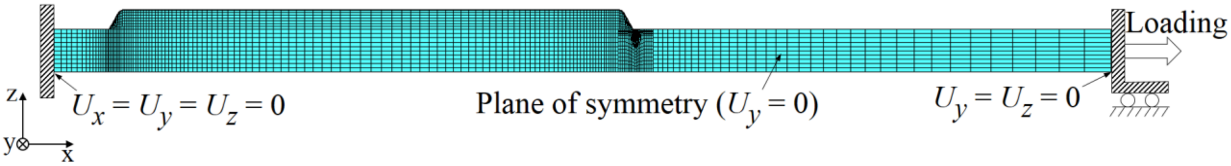

Fig. 5.10 Applied loading and boundary conditions used in calculation of SIF and FCP.

5.3.2 Influence of the change in welding HI and welding RS on the behavior of SIF

The SIF solutions for the four cases shown in Table 5.1 were calculated using three different constant amplitude stress loadings. More details on the applied cases, stress ranges, stress ratio and welding RS condition are given in Table 5.3. The required loading to compute SIF was calculated based on each stress range and stress ratio. For the no welding case, only external loading was applied. However, for the three welding HI cases welding RS was considered besides the external loading. The simulated welding RS obtained by the TEP FE model was mapped to the cracked FE model at the same location of the crack, where welding RS played as traction forces over the crack face. Welding RS that used in the calculation of SIF solutions represents as weld condition. Thereafter, the minimum and maximum SIF solutions (K_{Imin} and K_{Imax}) were calculated for each case based on the applied loadings and welding RS condition.

For the sake of simplicity, the calculated SIF solutions presented in this chapter are only for the measured cracks. Figures 5.11–5.14 show K_{Imin} and K_{Imax} for each stress range for each measured crack. Note that, the crack mouth and crack deepest point are given at $2\varphi/\pi = 0$ and $2\varphi/\pi = 1$, respectively. It is clear from the results shown in Figs. 5.11–5.14 that welding RS has a strong influence on the calculated SIF solutions along the crack front. The SIF solutions considerably increased when the welding RS is taken into account compared to those obtained by external loading only (i.e. no welding case). Further details on the influence of welding RS on the calculated SIF solutions are given in Table 5.4. From the data presented in Table 5.4, it can be observed that by increasing the stress range magnitude the ratio change in SIF solutions decreases. Furthermore, for the same stress range, it is noticed that crack no. 2 gives the largest ratio change in SIF solutions; however, crack no. 4 introduces the lowest ratio change. This may be due to the aspect ratios (*a*/*t* and *a*/*c*) of the measured cracks (see Fig. 5.8 and Table 5.2).

Table 5.3 Details of the applied cases and loading conditions used in the fracture and FCP analysis.

Case	Stress range, Δσ (MPa)	Stress ratio, R	Welding RS condition
No welding	140.6 168.8 196.9	0.1	Not considered
Low welding HI	140.6 168.8 196.9	0.1	Considered
Moderate welding HI	140.6 168.8 196.9	0.1	Considered
High welding HI	140.6 168.8 196.9	0.1	Considered

Table 5.4 Ratio change in SIF solutions with and without considering welding RS at the crack deepest point ($2\varphi/\pi = 1$).

Stress range, Δσ (MPa)	Measured crack no.	No–Low welding HI[a)		No–Moderate welding HI[b)		No–High welding HI[c)	
		K_{Imin}	K_{Imax}	K_{Imin}	K_{Imax}	K_{Imin}	K_{Imax}
140.6	1	2.17	12.74	2.13	12.26	2.10	12.04
	2	2.27	13.73	2.34	14.41	2.30	13.99
	3	2.03	11.28	2.18	12.78	2.21	13.07
	4	1.83	9.29	1.99	10.90	2.04	11.39
168.8	1	1.98	10.78	1.94	10.38	1.92	10.19
	2	2.06	11.60	2.12	12.16	2.08	11.81
	3	1.86	9.56	1.98	10.81	2.01	11.05
	4	1.69	7.90	1.82	9.24	1.87	9.65
196.9	1	1.84	9.38	1.80	9.04	1.79	8.88
	2	1.91	10.09	1.96	10.57	1.93	10.27
	3	1.73	8.34	1.84	9.41	1.86	9.62
	4	1.59	6.92	1.71	8.06	1.74	8.42

a) Ratio change calculated between SIF obtained by no welding case and that given by low welding HI case.

b) Ratio change calculated between SIF obtained by no welding case and that given by moderate welding HI case.

c) Ratio change calculated between SIF obtained by no welding case and that given by high welding HI case.

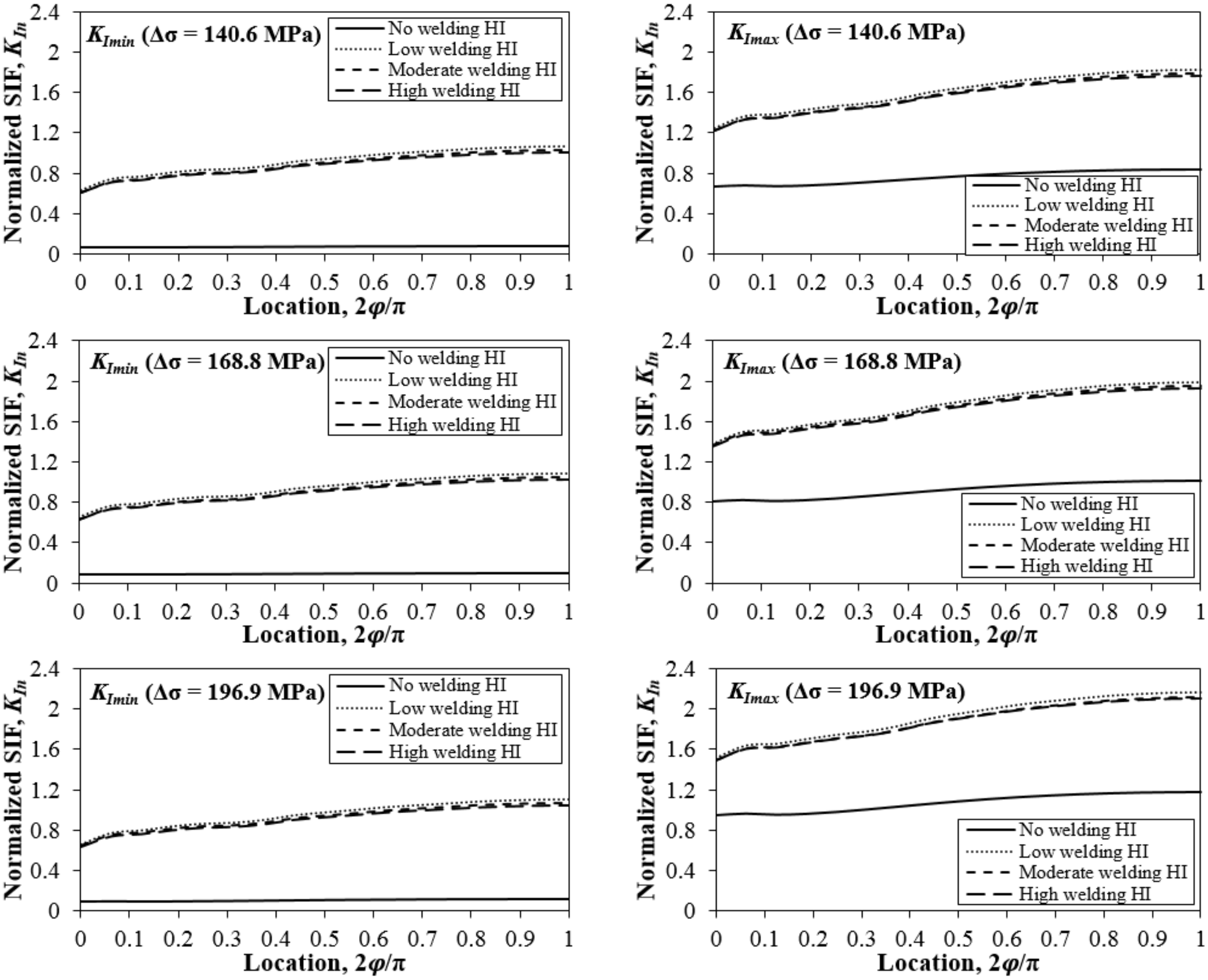

Fig. 5.11 Distribution of the normalized SIF solutions along the crack front under different stress amplitude loadings for crack no. 1.

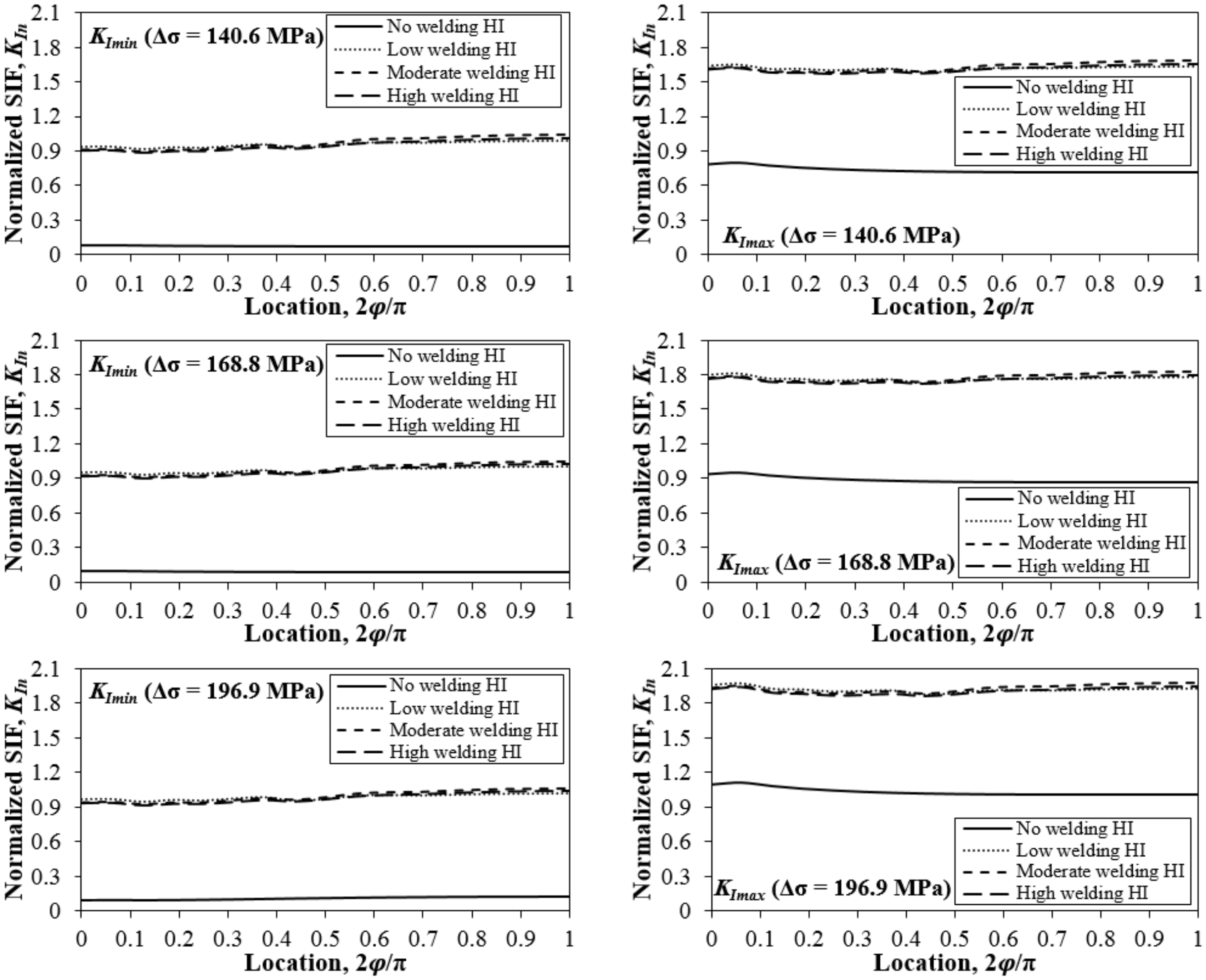

Fig. 5.12 Distribution of the normalized SIF solutions along the crack front under different stress amplitude loadings for crack no. 2.

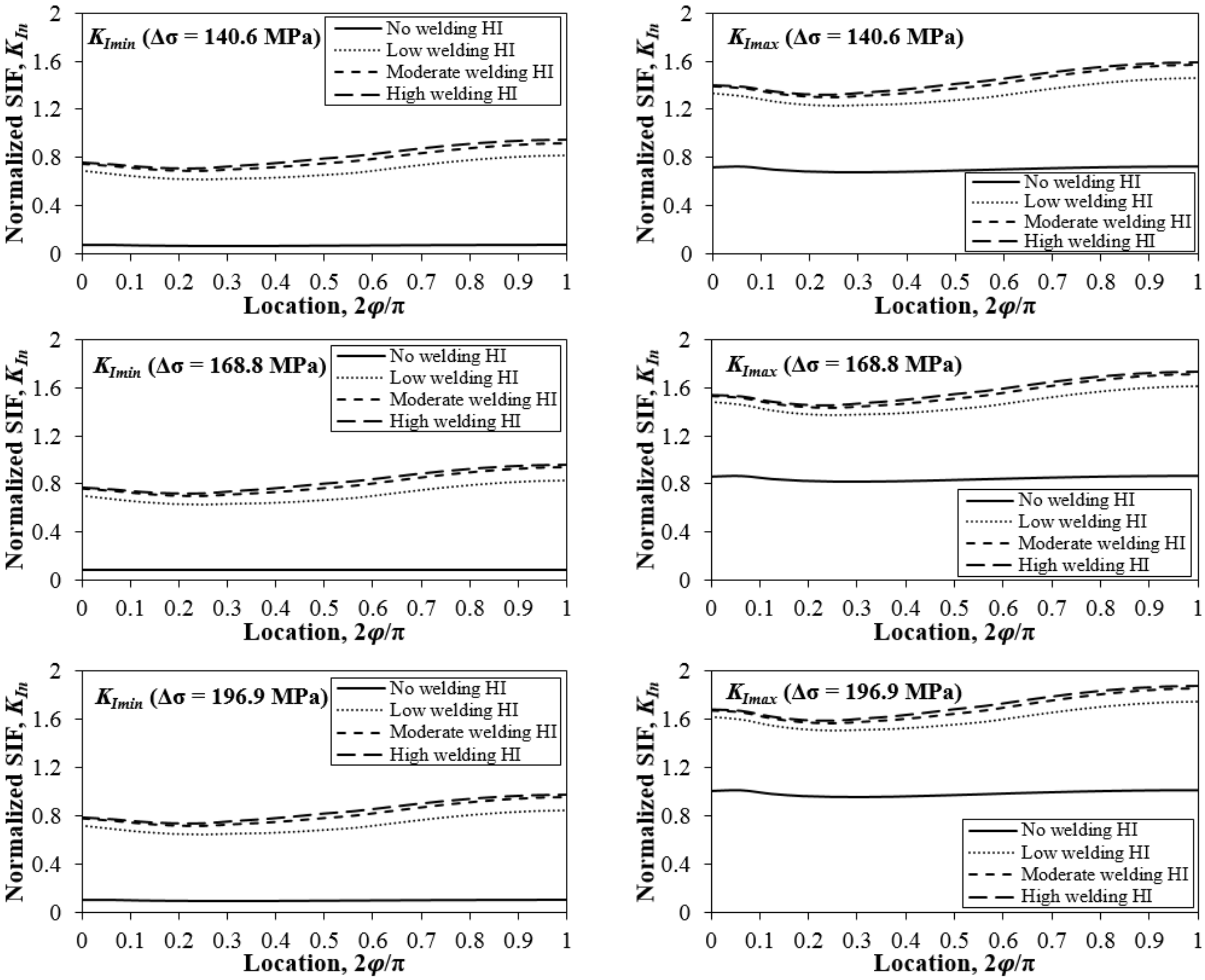

Fig. 5.13 Distribution of the normalized SIF solutions along the crack front under different stress amplitude loadings for crack no. 3.

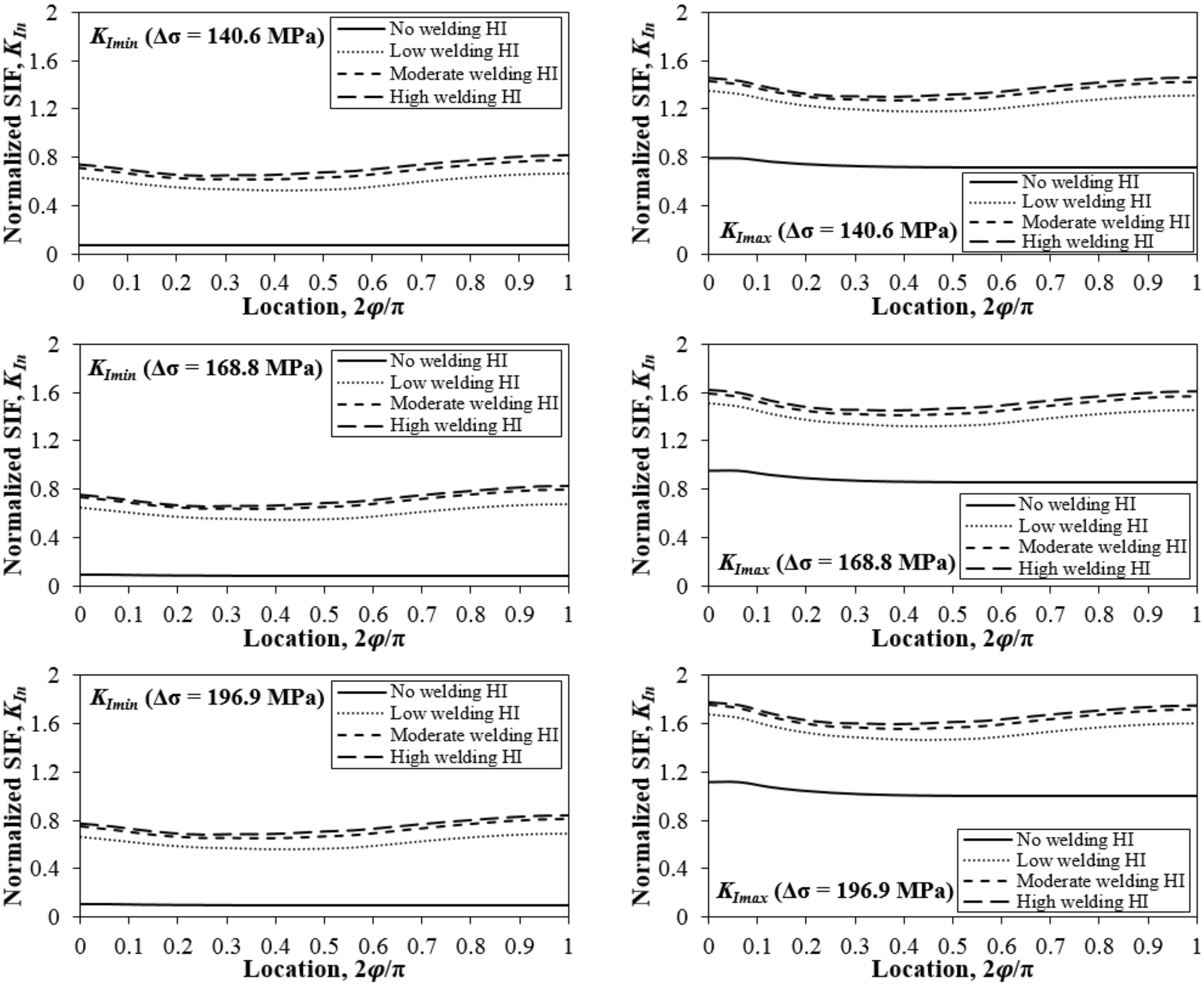

Fig. 5.14 Distribution of the normalized SIF solutions along the crack front under different stress amplitude loadings for crack no. 4.

On the other hand, it is observed that the change in welding HI did not reveal considerable influence on the behavior of SIF solutions for cracks no. 1 and 2 that represent small cracks (see Figs. 5.11 and 5.12). However, for the case of cracks no. 3 and 4 that represent larger cracks (see Figs. 5.13 and 5.14) a clear difference between the SIF solutions was noticed especially between SIF solutions obtained by the low welding HI case and the other welding HI cases (i.e. moderate and high). The reason why this occurred is that most of the crack propagation process takes place in the early stages when the crack size is small in which SIF is consumed in the propagation process. Therefore, a disregarded difference in SIF solutions was obtained for cracks no. 1 and 2 due to the change in welding HI. However, for larger cracks (i.e. cracks no. 3 and 4) the change in welding HI gave a clear difference in SIF solutions because the crack size became large enough in which

SIF was not consumed with the same amount as for smaller cracks. More information on this point is given in Table 5.4.

5.4 Evaluation of fatigue life considering the change in welding HI

For welded structures subjected to cyclic loads, it is necessary to examine the influence of welding RS on the fatigue life. As well, it is needed to investigate the influence of the change in welding HI on the behavior of FCP. For this purpose, the modified Paris law was utilized to evaluate the FCP where the effective SIF range, ΔK_{eff} was used instead of the SIF range, ΔK. The FCP equation that employed is defined as follows[91]:

$$\frac{da}{dN} = C\left[\left(\Delta K_{eff}\right)^m - (\Delta K_{th})^m\right] \qquad \text{for } \Delta K_{eff} > \Delta K_{th} \tag{5.1}$$

where *C* and *m* are FCP material constants, ΔK_{th} denotes threshold SIF range. Further, ΔK_{eff} is calculated as follows[92]:

$$\Delta K_{eff} = U^* \Delta K \tag{5.2}$$

where U^* represents stress range ratio and is defined as the ratio of effective stress range ($\Delta\sigma_{eff}$) to total stress range ($\Delta\sigma$), $U^* = \Delta\sigma_{eff}/\Delta\sigma$, U^* is influenced by various factors such as stress range, crack length, material properties and stress ratio *R*[92]. In this study, however, U^* is given to depend only on stress ratio *R* as reported by Elber[93]. U^* was applied using the following equation for structural steel[92]:

$$U^* = 0.722 + 0.278R^* \tag{5.3}$$

where R^* represents local stress ratio where it is a function of SIF solutions (i.e. K_{Imin} and K_{Imax}) for each crack size and defined as:

$$R^* = \frac{K_{Imin}}{K_{Imax}} \tag{5.4}$$

The FCP was calculated under constant stress amplitude loadings at the crack deepest point as experiments and simulations were conducted by Kusuba[86]. Therefore R^* was updated for each crack depth. As well, FCP was estimated starting with a specific initial crack size of a = 0.26 mm and c = 1.61 mm which was determined based on the aspect ratio of the employed measured cracks. on the other hand, many preliminary investigations regrading FCP material constants are available in literatures. Three FCP material constants for construction steel were adopted in this study (see Table 5.5). The selected FCP material constants are for base metal where welding RS is included in the calculated SIF. The FCP was calculated based on the three FCP material constants given in Table 5.5 using the SIF solutions obtained by the high welding HI case. The FCP was then validated with the experiments, see Fig. 5.15. From the results shown in Fig. 5.15, the calculated FCP for each stress range showed a good matching with the experiments. Some differences between the calculated and measured FCP were observed where these differences might be due to material chemical composition, mechanical properties and/or installation methods used in preparing and conducting tests for measuring FCP material constants. For the sake of comparison for the next FCP evaluation, only one FCP material constants was utilized. The FCP material constants reported by SIZ, 2001[94] was adopted, in order to examine the influence of the change in welding HI on the behavior of FCP, where they gave the closest agreement between the calculated and measured FCP for the applied stress ranges.

Table 5.5 Applied FCP material constants of base metal for construction steel from literature.

Literature	C (mm/cycle)	m (-)	ΔK_{th} (MPa$\sqrt{\text{mm}}$)	R (-)
Beden et al., 2008[95]	2.15e-14	3.43	63.25	> 0
SIZ, 2001[94]	4.51e-14	3.26	142.3	--
Blumenauer, 1993[94]	1.01e-14	3.50	158.1	--

Figure 5.16 shows the influence of the change in welding HI as well as welding RS on the behavior of FCP. From the results shown in Fig. 5.16, the change in welding HI has no clear impact on the calculated FCP. The difference obtained between the FCP solutions for the different welding HI cases is negligible. It is worth mentioning that this negligible difference is due to the influence of the local stress ratio, R^*. However, the difference in R^* for the different welding HI cases is also small which is not enough to give considerable difference in the calculated FCP. On the other hand, Fig. 5.16 reveals the significant influence of welding RS on the behavior of FCP. It is clear that when welding RS is included in the FCP calculation; the fatigue life is obviously reduced compared to that obtained by ignoring welding RS (i.e. no welding case). As it is discussed before, the welding RS revealed a strong influence on the computed SIF solutions, so the calculated

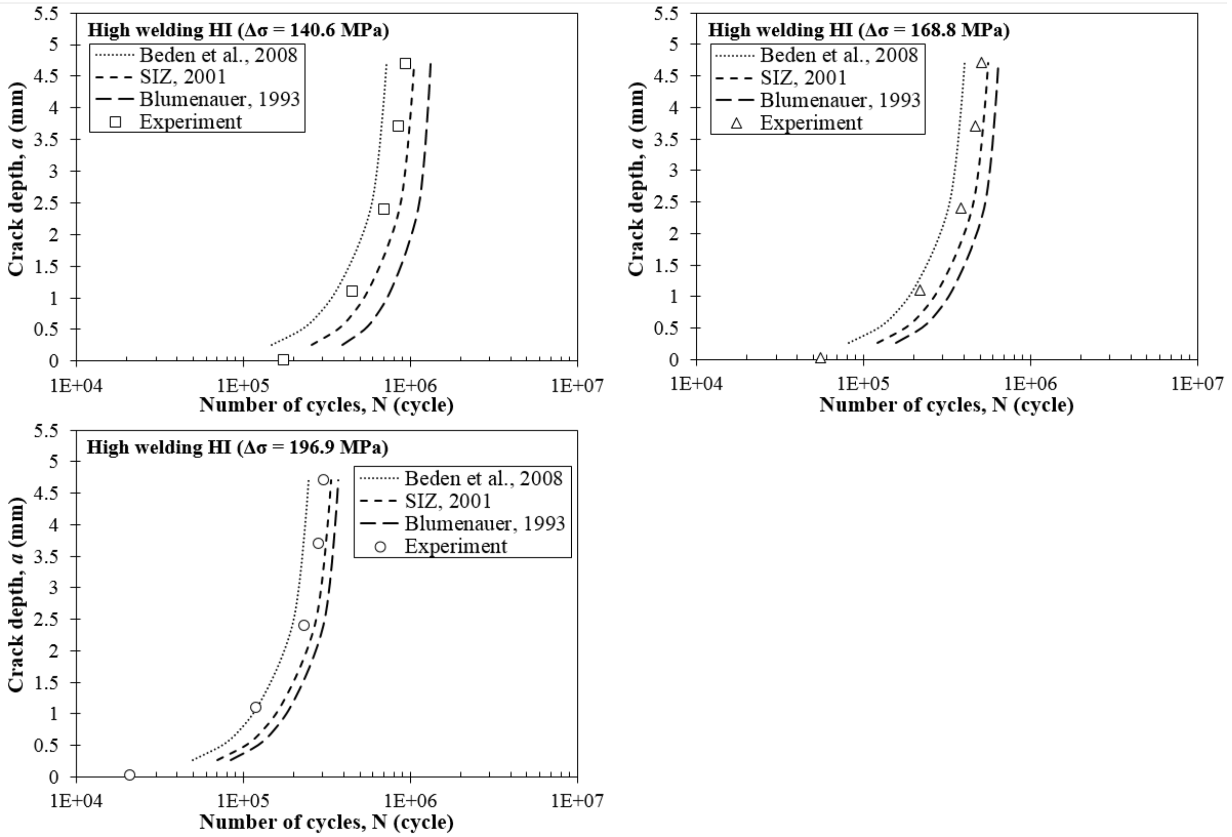

Fig. 5.15 Influence of FCP material constants on fatigue life under different stress amplitude loadings.

FCP influenced by the SIF solutions that considered welding RS. Moreover, Lee and Chang[79] reported that the reduction in fatigue life when including welding RS is because the longitudinal tensile welding RS which plays the role of the crack driving force that accelerates the FCP rate in conjunction with the applied external tensile stress. For further understanding, the reduction percentage in fatigue life when welding RS is considered obtained by the high welding HI case compared to that ignored welding RS which given by the no welding case is given in Table 5.6. Since the difference in the FCP obtained by the welding HI cases is negligible (see Fig. 5.16) and for the sake of simplicity, only one welding HI case (i.e. high welding HI) is used in Table 5.6 in addition to the no welding case. From Table 5.6, it is clear that when welding RS is included a large reduction in fatigue life is obtained. It is also observed that when the applied stress range increases the reduction percentage decreases. This is because in the case of large stress amplitude loading larger SIF solutions (K_{Imin} and K_{Imax}) are obtained (see Figs. 5.11–5.14) which make the crack propagates faster. As well, from the information given in Table 5.4, the difference obtained in SIF between the no welding and high welding HI cases for crack no. 4 reveals that by increasing the stress amplitude loading this difference decreases. This means that in case of very large stress amplitude loadings, the influence of welding RS on the FCP rate may not be significant compared to that obtained when welding RS is not considered[81][82].

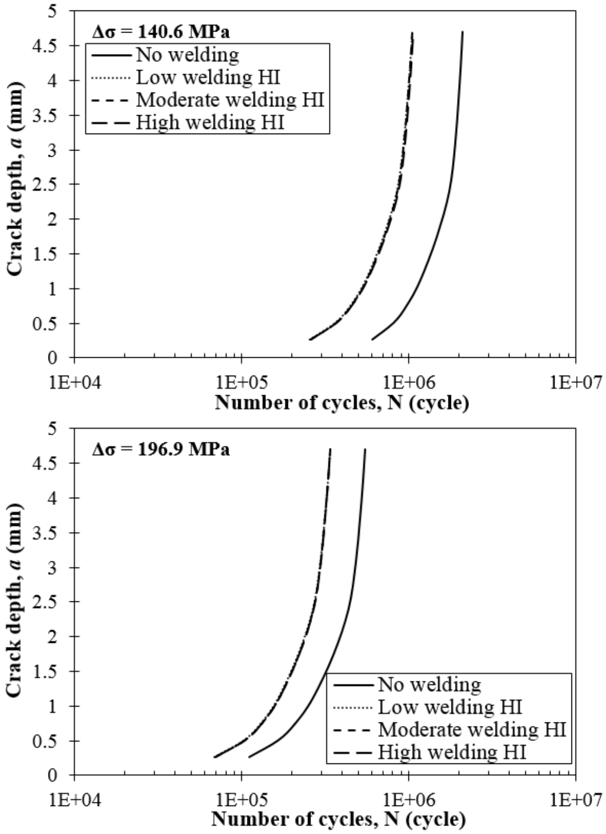

Fig. 5.16 Influence of the change in welding HI and welding RS on fatigue life under different stress amplitude loadings.

Table 5.6 Reduction percentage in fatigue life when considering welding RS under different stress ranges$^{a)}$.

Stress range, Δσ (MPa)	Reduction percentage (%)
140.6	49.3
168.8	41.7
196.9	37.8

$^{a)}$ Data taken for crack no. 4 (see Table 5.2) for no welding and high welding HI cases using SIZ, 2001[94] FCP material constants.

On the other hand, Fig. 5.17 shows a comparison between the FCP obtained by calculations and experiments. It is clear from Fig. 5.17 that the present solutions calculated based on SIF solutions including welding RS as well as utilizing FCP material constants of base metal show a very good agreement with experiments. As well, the comparison between the present solutions and Kusuba's solutions shows the accuracy of the present solutions. The results illustrated in Fig. 5.17 demonstrate the adequacy of the proposed technique, presented in chapter 4, that used to calculate SIF resulting from welding RS on the accuracy of the calculated FCP as well as the validity of the assumptions made for selecting FCP material constants and initial crack size. Therefore, for engineering problems, FCP material constants for base metal can be directly utilized when welding RS is considered in SIF solution.

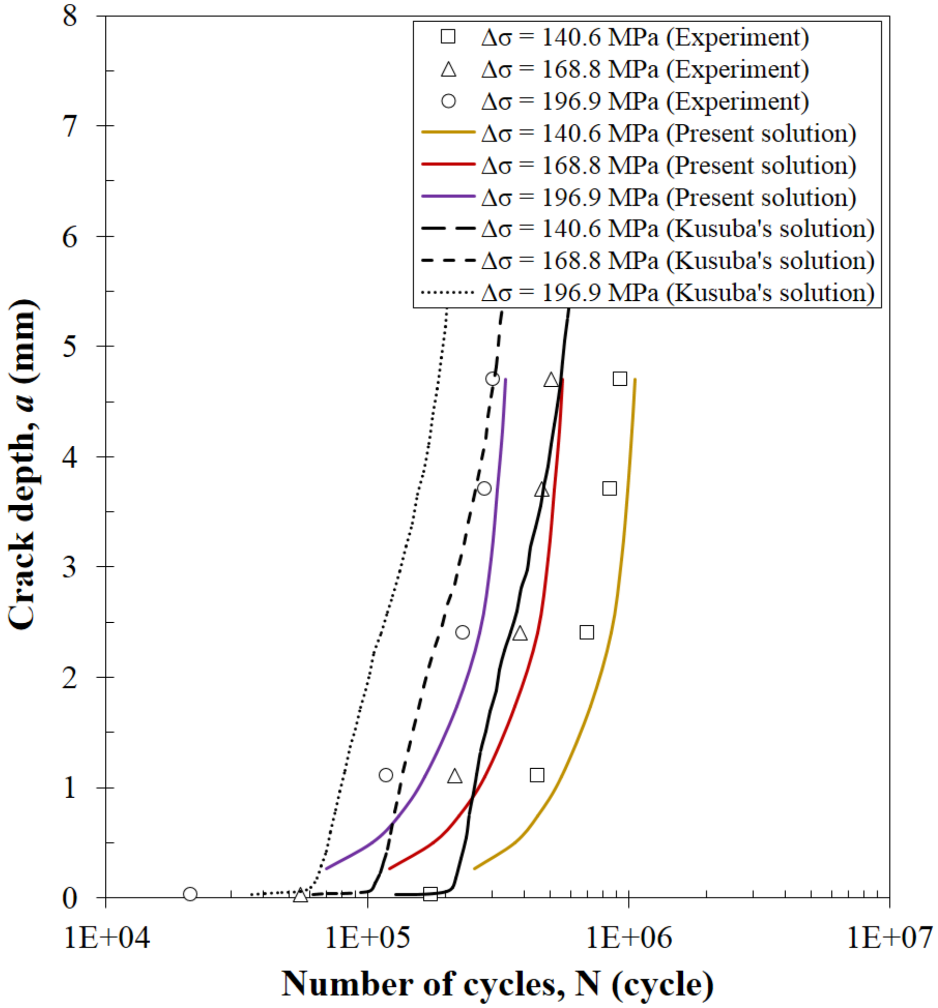

Fig. 5.17 Comparison of the calculated fatigue lives with simulations and experimental data. Note that: experiments and Kusuba's solutions are taken from Kusuba[86].

5.5 Discussion

5.5.1 Influence of the change in RS on the behavior of SIF and FCP

To understand why a negligible difference in the FCP results was obtained for the different welding HI cases, a fundamental study was conducted to examine the influence of the change in RS on the FCP behavior. In this fundamental study, two cases were investigated; the first case gives a small difference in the applied RS. The second one introduces a large difference in the applied RS. Each case includes three different RS fields. For this purpose, engineering equations were formulated to generate different RS fields over the crack face. The equations used for the case of small difference in RS are as follows:

Small RS
$$\frac{\sigma_x}{\sigma_Y} = -2.6754\left(\frac{y}{c}\right)^2 + 0.9 \tag{5.5}$$

Standard RS
$$\frac{\sigma_x}{\sigma_Y} = -2.9727\left(\frac{y}{c}\right)^2 + 1 \tag{5.6}$$

Large RS
$$\frac{\sigma_x}{\sigma_Y} = -3.2699\left(\frac{y}{c}\right)^2 + 1.1 \tag{5.7}$$

where σ_x is stress in longitudinal direction, σ_Y represents the yield stress, *y* denotes the location in y-direction and *c* is the crack half-length (see Fig. 5.9(b)). The small, standard and large RS represent the different RS fields. On the other hand, the employed equations for the case of large difference in RS are as follows:

Small RS
$$\frac{\sigma_x}{\sigma_Y} = -0.5945\left(\frac{y}{c}\right)^2 + 0.2 \tag{5.8}$$

Large RS
$$\frac{\sigma_x}{\sigma_Y} = -5.3508\left(\frac{y}{c}\right)^2 + 1.8 \tag{5.9}$$

Note that in the case of large difference in RS, Eq. 5.6 was also used as standard RS. The distribution of the calculated RS of the two studied cases (i.e. small and large difference in RS) is shown in Fig. 5.18. The RS distributions shown in Fig. 5.18 calculated based on Eqns. 5.5–5.9.

The analysis in this section was conducted using the same cracked FE model, boundary conditions and external stress amplitude loadings. The same procedures of calculating SIF and FCP, that mentioned previously, were followed in this section. The only difference is that the calculated RS replaced the simulated welding RS. The SIF solutions were firstly computed based on the calculated RS. The FCP was thereafter calculated for the two studied cases (i.e. small and large difference in RS).

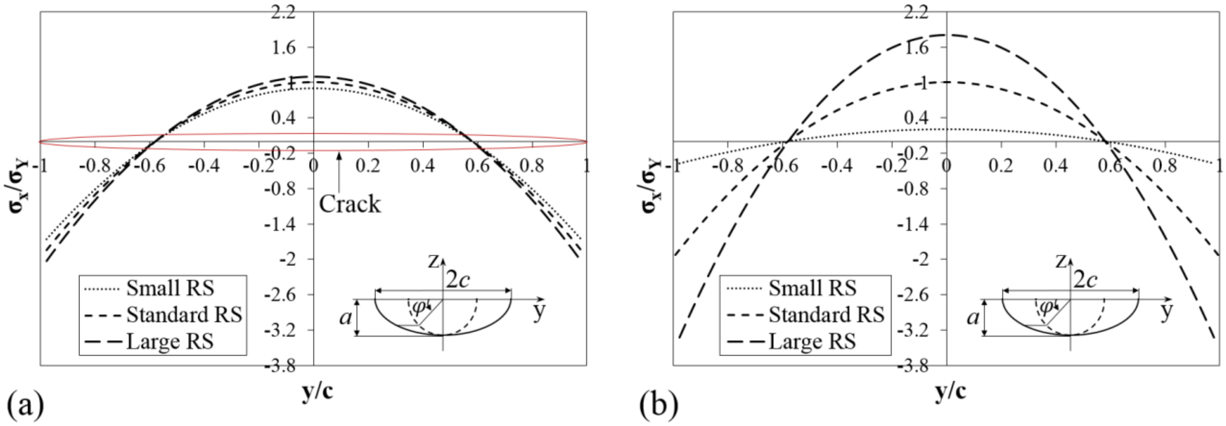

Fig. 5.18 Distribution of calculated RS over the crack face. (a) small difference in RS, and (b) large difference in RS.

The influence of the change in RS on the behavior of SIF is shown Figs. 5.19 and 5.20. For the sake of simplicity, the results shown in Figs 5.19 and 5.20 represent the maximum SIF obtained by one of the applied stress amplitude loadings (i.e. $\Delta\sigma$ = 140.6 MPa). It is observed that when the change in the applied RS is small (Fig. 5.18(a)) a small difference in the calculated SIF is obtained as shown in Fig. 5.19. However, for the case of large change in the applied RS (Fig. 5.18(b)) a clear difference in the computed SIF is observed as shown in Fig. 5.20. Furthermore, it is noticed that by increasing the crack size the difference in the SIF increases which agrees with the results presented in Figs. 5.11–5.14 and it is due to most of SIF is consumed in crack propagation process when the crack size is small that does not give clear difference with the other RS cases. However when the crack size increases during the propagation process, the SIF consumed in the propagation process with a small amount that gives a considerable difference in its behavior with the other RS cases.

On the other hand, the FCP results based on the small and large change in RS are shown in Figs. 5.21 and 5.22, respectively. For the sake of comparison, the case of no RS over the crack face is included. The behavior of the FCP shown in Figs. 5.21 and 5.22 agrees well with the behavior of the SIF illustrated in Figs. 5.19 and 5.20, respectively. From Fig. 5.21 it is clear that when the change in the applied RS is small (Fig. 5.18(a)), a trivial difference in the calculated FCP is obtained. However when the change in the applied RS is large (Fig. 5.18(b)), a clear difference is observed in the FCP behavior as shown in Fig. 5.22. For more details, Tables 5.7 and 5.8 give the percentage difference in the estimated fatigue lives when small and large difference in RS are employed under different stress ranges, respectively. It is clear from Table 5.7 that the percentage difference obtained between the low RS vs. moderate RS and moderate RS vs. large RS is less than 3% that represents a small percentage difference for the applied RS condition (i.e. small difference in RS). On the other hand, the percentage difference given in Table 5.8 clarifies that a large difference in fatigue life is obtained for the cases of low RS vs. moderate RS and moderate RS vs. large RS. The data given in Table 5.8 demonstrates that a significant influence in the behavior of FCP can be obtained when the difference in the applied RS is large.

The results shown in Figs. 5.19–5.22 and Tables 5.7 and 5.8 demonstrate that the change in the applied RS has a significant impact on the behavior of SIF and FCP. As well, this explains why a disregarded difference in the SIF results (Figs. 5.11–5.14) and FCP results (Fig. 5.16) was obtained for the applied welding HI cases.

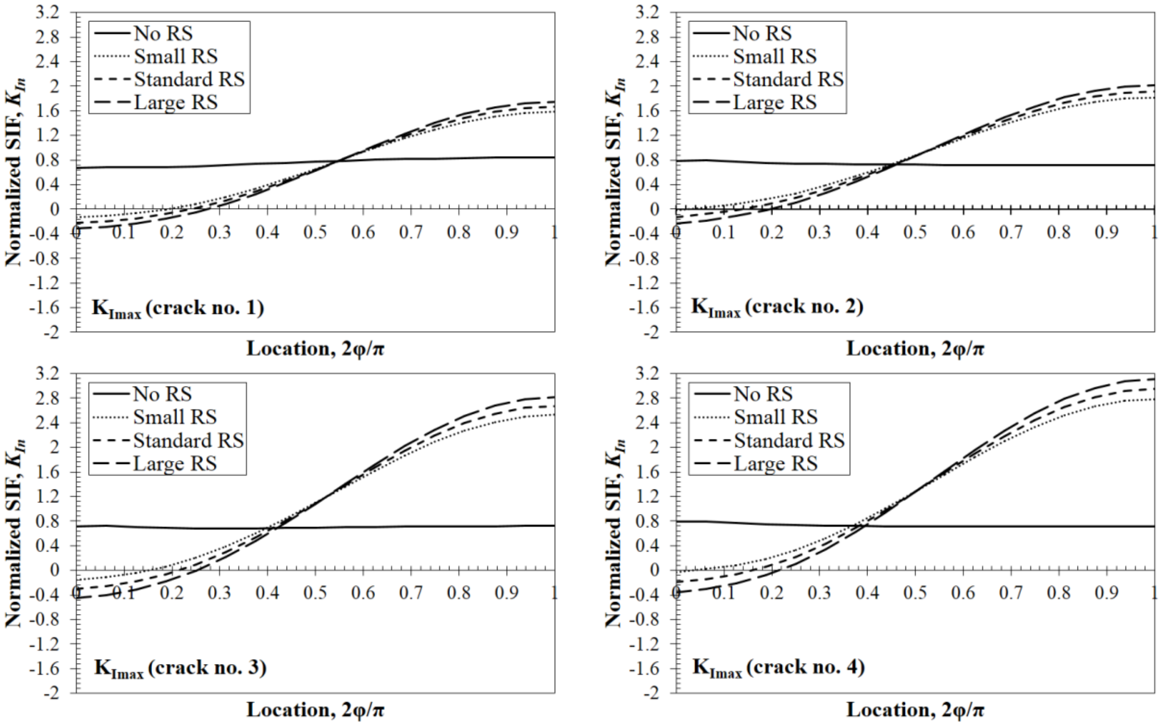

Fig. 5.19 Influence of the small difference in RS on the behavior of SIF.

Although the change in welding HI reveals a clear influence on the distribution of welding RS; however, the difference in the simulated welding RS obtained by the different welding HI cases is small and this led to give no considerable influence on the behavior of SIF and FCP. However, the results of the SIF and FCP obtained by the simulated welding RS represent special cases. In general, the difference in RS substantially influences the behavior of SIF and FCP. On the other hand, the FCP evaluated in this section based on the formulated engineering equations (Eqns. 5.5–5.9) give a macroscopic mean stress filed. However, for more accurate and precise evaluation of the FCP behavior for cracks in welding RS field, an efficient tool is need. Recently, the crack cohesive zone model [96][97][98][99] has been used in fracture problems and employed to evaluate the FCP behavior with high accuracy. One of the advantages of the crack cohesive zone model is that a local stress field (i.e. microscopic stress scale) can be employed at the crack front. Further, the FCP material constants used in this study were adopted to fit the experiments results. Therefore, the employed FCP material constants are valid for the chosen BOP FE model and welding conditions in which good agreement was obtained between the calculated fatigue lives and experiments. However, the adopted FCP material constants and engineering equations (Eqns. 5.5–5.9) may be not appropriate for other numerical problems. So that, proper FCP material constants and stress fields should be employed properly.

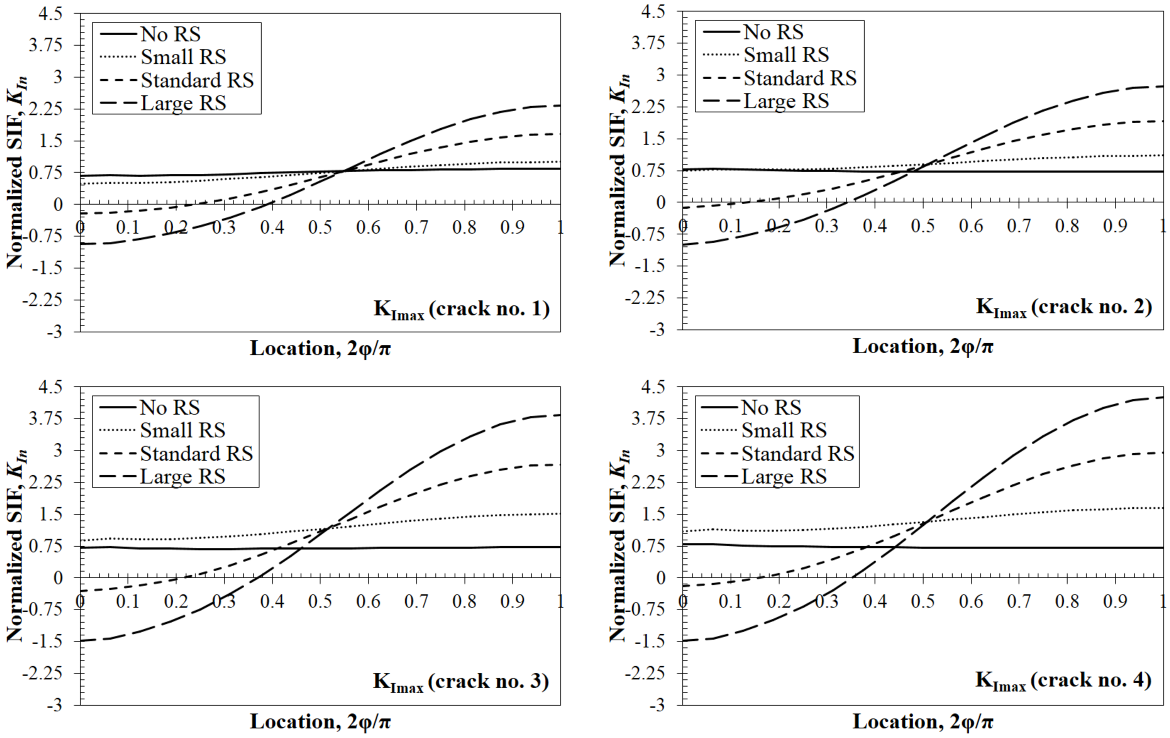

Fig. 5.20 Influence of the large difference in RS on the behavior of SIF.

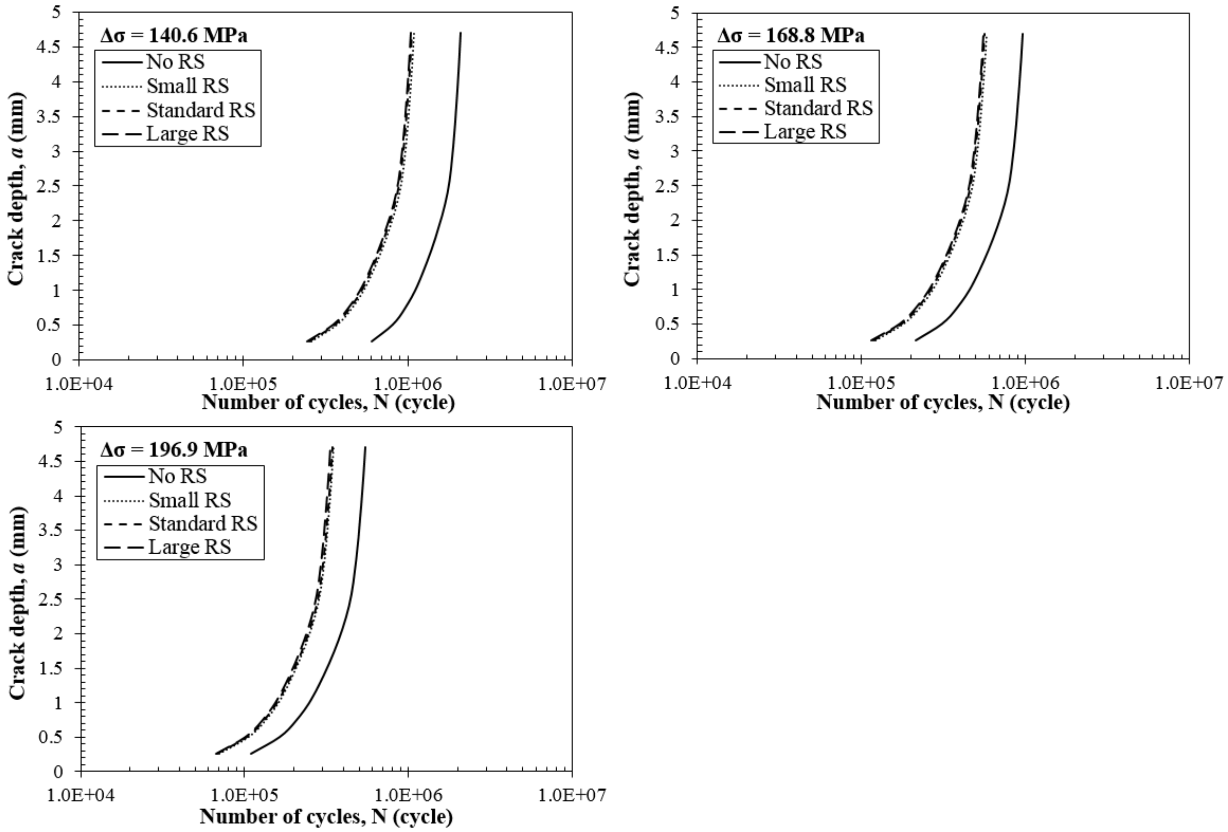

Fig. 5.21 Influence of the small difference in RS on the behavior of FCP.

5.5.2 Influence of clamping process on stress ratio and FCP

As it is mentioned previously, the change in welding HI not only influences the welding penetration and welding RS but also has a considerable impact on the welding distortion. In fatigue testing, test specimen is fixed by clamps where leads to straighten the distorted specimen. Clamping process introduces bending moment into the distorted specimen that induces tensile stress on the upper surface of the specimen. This tensile stress may be called clamping stress (σ_{cl}) which is defined as the required stress to straighten the distorted specimen and its magnitude depends on the amount of distortion produced by welding. As it is known, stress ratio (R) is the ratio of minimum stress (σ_{min}) to maximum stress (σ_{max}), $R = \sigma_{min}/\sigma_{max}$. However, in practical situation, σ_{cl} is introduced into test specimen after clamping. This means that the stress ratio should include the stress introduced due to clamping, σ_{cl}, so the stress ratio can be written in the following form:

$$R^+ = \frac{\sigma_{min} + \sigma_{cl}}{\sigma_{max} + \sigma_{cl}} \tag{5.10}$$

where R^+ is the stress ratio including clamping stress, σ_{cl}. From Eq. 5.10 it is clear that R^+ will influence due to the presence of σ_{cl}. In other words if the produced welding distortion is small, the applied moment to straighten the distorted specimen will be small and then the introduced σ_{cl} will be small as well and vice versa. Therefore, when σ_{cl} is small the amount of increase in R^+ will be small compared to the stress ratio R. However, if σ_{cl} is considerably large then the amount of increase in R^+ will be larger than R which will lead to an increase in the calculated SIF and thereafter may influence the calculated FCP rate. In general, further work using simulations is needed to verify the influence of the change in welding HI on σ_{cl} and then fatigue life.

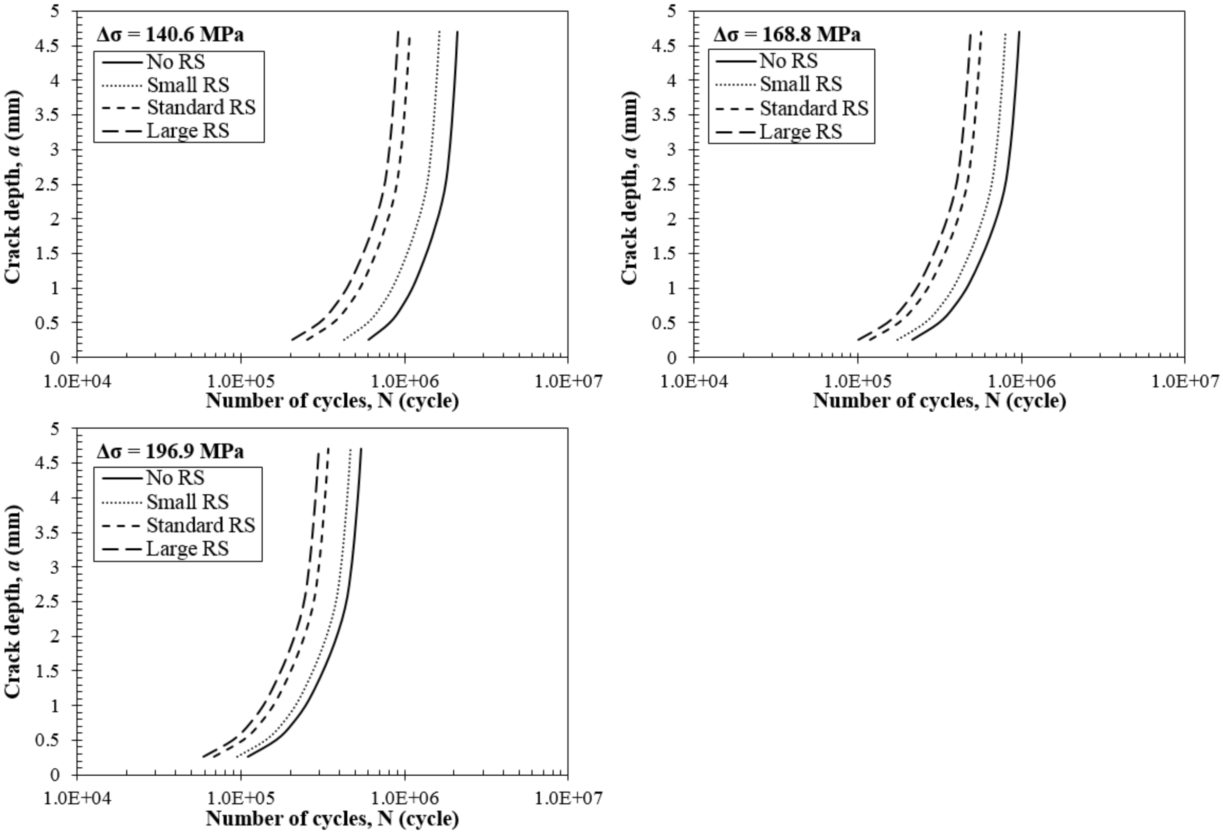

Fig. 5.22 Influence of the large difference in RS on the behavior of FCP.

Table 5.7 Percentage difference in fatigue life when a small difference in RS is employed under different stress ranges[a)].

Stress range	Percentage difference, %		
$\Delta\sigma$, MPa	no welding–low RS	low RS–moderate RS	moderate RS–large RS
140.6	47.32	2.94	2.63
168.8	39.48	2.68	2.42
196.9	35.47	2.55	2.32

[a)] Data given in the above table are taken for crack size of a = 4.7 mm and c = 6.35 mm.

Table 5.8 Percentage difference in fatigue life when a large difference in RS is employed under different stress ranges[a)].

Stress range	Percentage difference, %		
$\Delta\sigma$, MPa	no welding–low RS	low RS–moderate RS	moderate RS–large RS
140.6	22.35	34.16	14.35
168.8	16.51	29.46	13.62
196.9	13.85	27.01	13.35

[a)] Data given in the above table are taken for crack size of a = 4.7 mm and c = 6.35 mm.

5.6 Summary

The influence of the change in welding HI on welding RS distribution and the behavior of SIF and FCP was investigated using a BOP FE model. As well, the influence of welding RS on the behavior of SIF and FCP was discussed. The proposed technique that introduced in chapter 4 was employed to calculate SIF solutions resulting from welding RS as well as external loading for surface cracks placed at the weld toe. Based on the analyses results; the following conclusions can be drawn:

1) The change in welding HI has a clear influence on welding penetration, welding distortion and welding RS distribution. However, it did not give considerable impact on the behavior of SIF and FCP for the applied welding HI cases and selected FE model.
2) Based on the simulation results, an uncertainty in the applied welding conditions (i.e. welding HI) may influence the distribution of the induced welding RS. However, this uncertainty in welding conditions may have no considerable impact on the behavior of SIF and FCP.

3) A fundamental study was conducted to examine the influence of the change in RS on the behavior of SIF and FCP. For this purpose, engineering equations were formulated to generate different RS distributions over the crack face. It is observed that when the difference in the applied RS is small, the RS has a negligible influence on the behavior of SIF and FCP. However if the difference in the applied RS is large, the RS reveals a considerable impact on the behavior of SIF and FCP.

4) Welding RS has a significant influence on the behavior of SIF and FCP when compared with those neglect the influence of welding RS. When welding RS considered in SIF solutions, SIF magnitude significantly increased compared to the case of no welding RS. Therefore, a large reduction in the calculated fatigue lives was observed when welding RS taken into account. A reduction percentage of 37.8%–49.3% in fatigue lives was obtained for the applied stress amplitude loadings.

5) The calculated fatigue lives based on the proposed technique that adopted for computing SIF solutions considering welding RS were validated with experiments. As well, the accuracy of the calculated fatigue lives were verified with simulated data.

CHAPTER 6

Developed WARP3D-IIM for calculating mixed-mode SIFs for cracks in non-uniform stress fields

6.1 Evaluation of the CFT-integral in WARP3D code

As mentioned before, the CFT-integral is implemented in WARP3D-IIM; however, in the current version of WARP3D, this integral is valid only for a uniform distributed stress field over the crack face. Therefore in order to employ the WARP3D-IIM for solving problems that give mixed-mode SIFs (e.g. complex welded geometries), the WARP3D code must be modified. This section introduces some details on the steps for evaluating the CFT-integral (see Eq. 6.1) in WARP3D-IIM.

$$\int_{S^{+}+S^{-}} t_j u_{j,1}^{aux} q dS \tag{6.1}$$

Healy et al.[26] proposed that for elements adjacent to the crack front, the integrand of Eq. 6.1 generally contains an inverse square-root singularity which the standard Gaussian quadrature cannot integrate exactly. A change of variables permits the exact integration of Eq. 6.1 for elements with straight edges along the crack front (linear elements or quadratic elements with front nodes placed on a chordal approximation). For a 1-D function $f(r)$ with an inverse square-root singularity at one boundary of the domain of integration, the substitution $t = \sqrt{r}$, removes the singularity[100]:

$$\int_{a}^{b} f(r)dr = \int_{0}^{\sqrt{b-a}} 2tf(t^2+a)dt \qquad (b > a) \tag{6.2}$$

Healy et al.[26], for example, defined $f(r) = 1/\sqrt{r}$ and assigned the integration limits a and b as $r = 0$ and $r = L_e$, that represents the length of an element adjacent to the crack front. the relationship $r = t^2$ leads to $f(t^2 + a) = 1/t$, which gives the following relationship[26]:

$$\int_0^{L_e} \frac{1}{\sqrt{r}} dr = \int_0^{\sqrt{L_e}} 2t \frac{1}{t} dt = \int_0^{\sqrt{L_e}} 2dt = 2\sqrt{L_e} \tag{6.3}$$

Healy et al.[26] continued that to evaluate the CFT-integral (Eq. 6.1) over a planar 2-D surface where coordinate z is tangent to the crack front, $f(z,r)$includes traction values, t_j, auxiliary-displacement derivatives, $u_{j,1}^{aux}$, and q-function values. They also reported that integration in the z-direction does not require special treatment, and the standard Gauss quadrature in this direction can provide exact results.

To implement the above procedure numerically, Healy et al.[26] performed a change of variables in parent (natural, intrinsic) coordinates. From Eq. 6.1, the following equation can be obtained:

$$\int_{-1}^{1} \int_{-1}^{1} f(\xi,\eta) d\eta d\xi = \int_{-1}^{1} \int_{0}^{\sqrt{2}} 2t f(\xi, t^2 - 1) dt d\xi \tag{6.4}$$

where the inverse square-root singularity of $f(\xi,\eta)$ in the parent coordinates corresponds to the lower integration boundary $\eta = -1$. In Eq. 6.4 and in the following steps Healy et al.[26] assumed that parent coordinate, ξ, is tangent to the crack front, and that η corresponds to distance r from the crack front. Integrands in Eq. 6.4 include traction values, t_j, auxiliary-displacement derivatives, $u_{j,1}^{aux}$, q-function values, and the determinant of the coordinate Jacobian, det **J**.

Healy et al.[26] proceeded that in order to apply a Gaussian quadrature rule formulated for the interval $[-1,1]$, to the inner integral of Eq. 6.4 over interval $\left[0,\sqrt{2}\right]$, it is necessary to employ the standard transformation[101]:

$$t = \frac{b-a}{2}\eta + \frac{b+a}{2} \tag{6.5}$$

where a and b are the new limits of integration, 0 and $\sqrt{2}$, respectively. From Eq. 6.5, the following relationships obtained[26]:

$$t = \tfrac{1}{\sqrt{2}}(\eta + 1), \text{ and } \tfrac{dt}{d\eta} = \tfrac{1}{\sqrt{2}} \tag{6.6}$$

then the quadrature for Eq. 6.4 over one element face becomes[26]:

$$\frac{1}{\sqrt{2}}\sum_{p} 2tf(\xi, t^2 - 1)\, w_p \tag{6.7}$$

where the summation includes all Gaussian integration points at coordinates (ξ, t), where t is defined in Eq. 6.6. Weights w_p in Eq. 6.7 correspond to the standard Gauss-quadrature rule formulated over interval $\xi = \eta = [-1,1]$, and the Jacobian of the interval transformation represented by $1/\sqrt{2}$.

Healy et al.[26] prepared steps to describe the procedure for evaluating the CFT-integral (Eq. 6.1) using the details described above:

1) Collect data for element faces and nodes (coordinates, q-values, tractions etc.).
2) Loop over integration points. A 2×2 quadrature rule yields exact results for the constant face tractions employed in this study.
3) For the current integration point, obtain weight and parent coordinates (ξ, η) based on a standard rule for the interval $\xi = \eta = [-1,1]$.
4) Shift the value of η according to Eq. 6.6: $\eta_{new} = 1/\sqrt{2}(\eta + 1)$
5) Redefine η as in Eq. 6.4: $\eta = (\eta_{new})^2 - 1$.
6) Evaluate standard element shape functions, shape-function derivatives, the coordinate Jacobian matrix, and the determinant of the coordinate Jacobian matrix, det **J**, using ξ and η obtained from step 5.
7) Use element shape functions to determine the local coordinates, (X_1^p, X_2^p, X_3^p), of the current integration point, and the q-value and traction value at the integration point.
8) Calculate distance r and angle $\theta = \pm\pi$ from the crack front to the integration point based on the coordinates determined in step 7.
9) Evaluate the auxiliary-displacement derivative $u_{j,1}^{aux}$using $\mu(s)$, r and θ from the previous step, and 1.0 for the SIF.
10) Evaluate the integrand in Eq. 6.7 as: $w_p \times q(\xi, \eta) \times t_j(\xi, \eta) \times u_{j,1}^{aux}(\xi, \eta) \times \det\boldsymbol{J}$, where summation is implied by the repeated index.
11) Complete the quadrature in Eq. 6.7 by multiplying the result of step 10 by $1/\sqrt{2} \times 2t$.

12) Sum contribution from integration point, and cycle to next point.

The procedure steps described above calculate the CFT-integral based on a uniform distributed stress field over the crack face. In other words, the current WARP3D-IIM processes only traction forces normal to the crack face (i.e. 1-component of stress state). However, the other normal and shear traction forces are not included in the numerical implementation of the CFT-integral. In this chapter, the WARP3D-IIM was modified in order to process the normal and shear stress components of a stress field (i.e. 6-components of stress state) in the traction forces term in the CFT-integral. The WARP3D-IIM was modified based on Cauchy stress tensor:

$$T_j^{(n)} = \boldsymbol{\sigma}^T . n_i \tag{6.8}$$

where $\boldsymbol{\sigma}$ is stress tensor, n_i denotes unit-length direction vector (i.e. normal vector) and $T_j^{(n)}$ represents stress vector. Where the stress tensor, $\boldsymbol{\sigma}$, that includes the normal and shear stress components defined as:

$$\boldsymbol{\sigma}^T = \begin{bmatrix} \sigma_{xx} & \tau_{yx} & \tau_{zx} \\ \tau_{xy} & \sigma_{yy} & \tau_{zy} \\ \tau_{xz} & \tau_{yz} & \sigma_{zz} \end{bmatrix} \tag{6.9}$$

and the normal vector, n_i, given as:

$$n_i = \begin{Bmatrix} n_x \\ n_y \\ n_z \end{Bmatrix} \tag{6.10}$$

The stress vector, $T_j^{(n)}$, represents the traction forces (i.e. t_j) in 3-D manner, as following:

$$T_j^{(n)} = \begin{Bmatrix} t_x \\ t_y \\ t_z \end{Bmatrix} \tag{6.11}$$

where t_x, t_y and t_z are the traction forces implemented in x-, y- and z-direction, respectively. Using Eqns. 6.9–6.11 in Eq. 6.8, the traction forces including the normal and shear components of stress at an element over the crack face is defined as:

$$\begin{Bmatrix} t_x \\ t_y \\ t_z \end{Bmatrix} = \begin{bmatrix} \sigma_{xx} & \tau_{yx} & \tau_{zx} \\ \tau_{xy} & \sigma_{yy} & \tau_{zy} \\ \tau_{xz} & \tau_{yz} & \sigma_{zz} \end{bmatrix} . \begin{Bmatrix} n_x \\ n_y \\ n_z \end{Bmatrix} \tag{6.12}$$

The WARP3D-IIM was modified using Eq. 6.12. To verify the adequacy of the modified WARP3D-IIM, a problem that introduces mixed-mode SIFs should be examined.

6.2 Verification problem: an inclined penny crack embedded in an infinite body

This section discusses the verification of the accuracy and adequacy of the modified WARP3D-IIM using an inclined penny crack embedded in an infinite body. The geometry of the inclined penny cracked body is shown in Fig. 6.1. The cracked body shown in Fig. 6.1 gives one-half symmetric body about x-axis. The semi-elliptical penny crack has an aspect ratio (*a*/*c*) of 0.35 with a slant angle of 45°. The cracked body subjected to a uniaxial stress in z-direction. Due to the geometry of the inclined crack, mixed-mode SIFs are obtained. The FE model corresponding to the inclined penny cracked body is shown in Fig. 6.2. The FE model (Fig. 6.2) generated by the same procedures described in chapter 4. The FE model consists of cracked mesh which generated with a fine mesh density (refer to section 4.2) and global mesh. The two meshes generated using 20-noded isoparametric hexahedral elements. The cracked mesh then connected to the global mesh using the tying option available in WARP3D code. Young's modulus and Poisson's ratio employed in the analysis have values of 206 GPa and 0.3 respectively. The rigid body motion of the models was prevented by applying the minimum displacement constraints, as shown in Fig. 6.2.

As a first step in verifying the modified WARP3D-IIM, the external loading solutions obtained by the WARP3D-IIM were validated with those calculated by analytical equations (i.e. analytical solutions). The equations of analytical solutions that used to verify the external loading solutions computed by the WARP3D-IIM taken from Kassir and Sih[102].

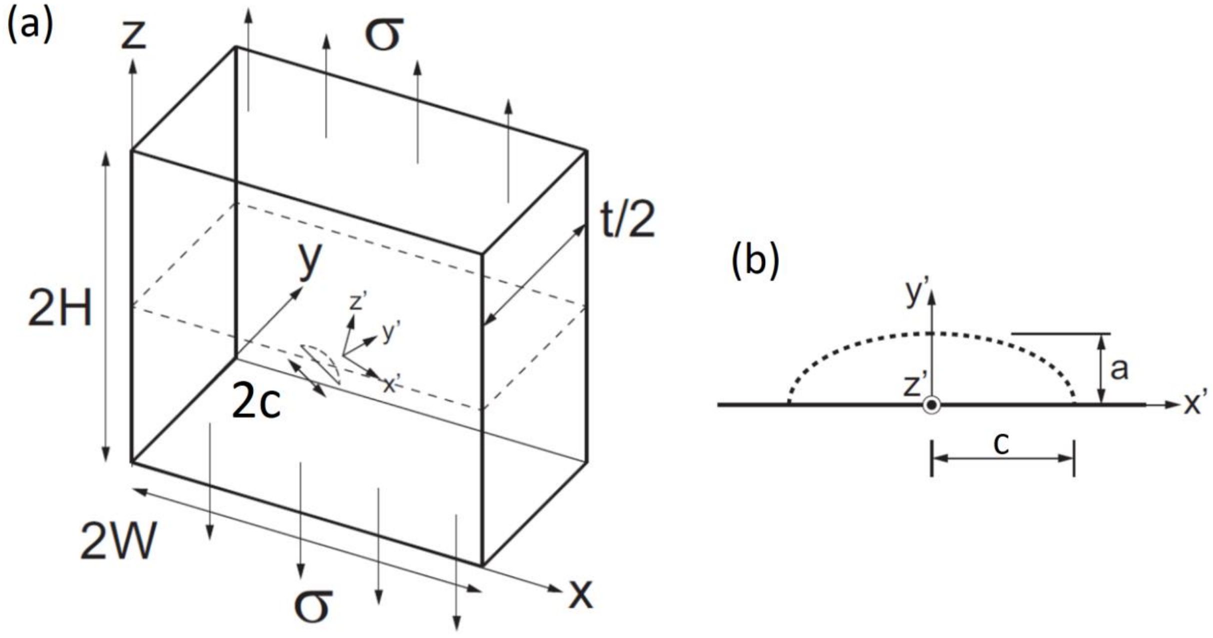

Fig. 6.1 One-half inclined penny crack embedded in an infinite body. (a) geometry of the penny cracked body and (b) geometry of the semi-elliptical penny crack.

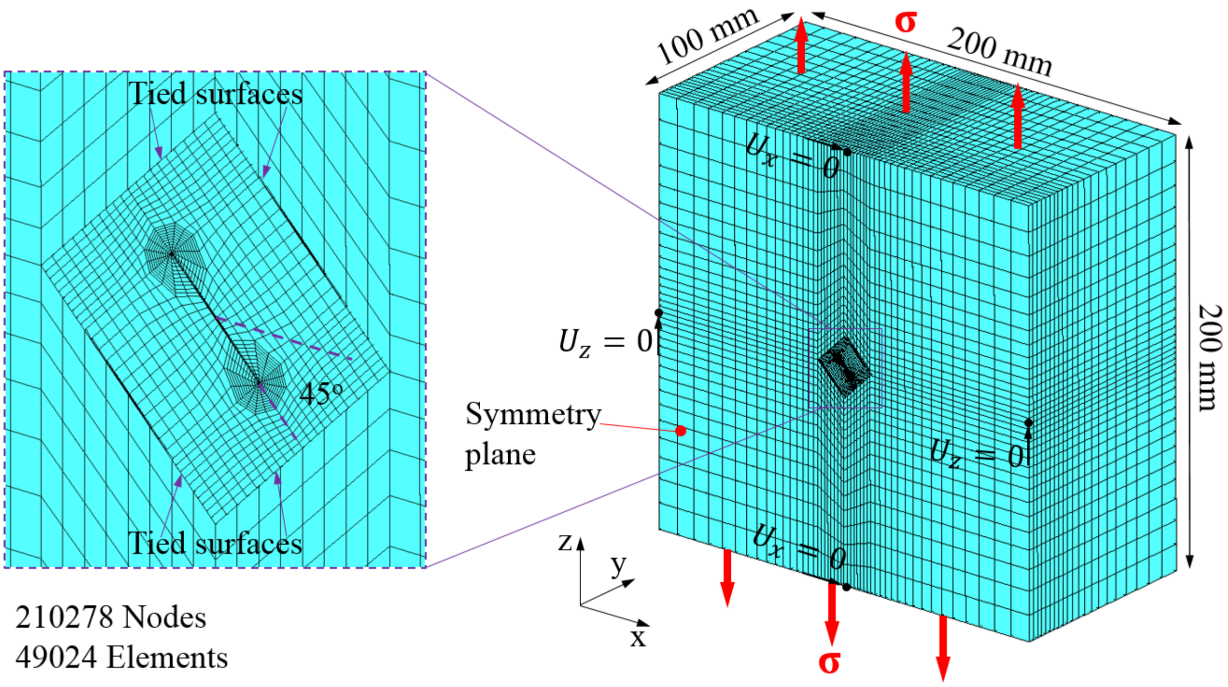

Fig. 6.2 Typical one-half symmetric FE mesh of an inclined penny cracked body using Zencrack software.

The equations of analytical solutions for calculating the mixed-mode SIFs for an inclined penny crack embedded in an infinite body are given in Eqns. 6.13–6.15:

$$K_I = \frac{\sigma\sqrt{\pi a}}{E(k)}(1 - k^2 cos^2\varphi)^{1/4} \tag{6.13}$$

$$K_{II} = \left(\tau\frac{k' cos\varphi}{B}\right)\frac{\sqrt{\pi a}k^2}{(1 - k^2 cos^2\varphi)^{1/4}} \tag{6.14}$$

$$K_{III} = \left(\tau\frac{sin\varphi}{B}\right)\frac{(1-\nu)\sqrt{\pi a}k^2}{(1 - k^2 cos^2\varphi)^{1/4}} \tag{6.15}$$

where σ and τ are normal and shear stresses, respectively over the inclined crack face. The variables k, $E(k)$ and B are defined as following:

$$k = \sqrt{\left(1 - \frac{a^2}{c^2}\right)} \tag{6.16}$$

$$E(k) = \sqrt{Q\left(\frac{a}{c}\right)} \tag{6.17}$$

$$B = (k^2 - \nu)E(k) + \nu k'^2 K(k) \tag{6.18}$$

where $Q(a/c)$ defined previously in Eq. 3.2 and , k' and $K(k)$ are given as following:

$$k^2 + k'^2 = 1 \tag{6.19}$$

$$K(k) = \int_0^{\pi/2} \frac{d\varphi}{\sqrt{1 - k^2 sin^2\varphi}} \tag{6.20}$$

then the calculated mixed-mode SIFs are normalized as following:

$$K_{I(normalized)} = \frac{K_I}{\sigma\sqrt{\frac{\pi a}{Q(a/c)}}} \tag{6.21}$$

$$K_{II(normalized)} = \frac{K_{II}}{\tau\sqrt{\frac{\pi a}{Q(a/c)}}} \tag{6.22}$$

$$K_{III(normalized)} = \frac{K_{III}}{\tau\sqrt{\frac{\pi a}{Q(a/c)}}} \tag{6.23}$$

The validation of the external loading mixed-mode solutions calculated by the WARP3D-IIM with those given by the analytical equations are shown in Fig. 6.3. As shown in Fig. 6.3 excellent agreement obtained between the external loading solutions and those given by analytical equations. The percentage difference between the external loading solutions and analytical solutions is less than 0.3% at the crack deepest point (at $2\varphi/\pi = 1$).

After validating the external loading solutions, the superposition method was implemented using the modified WARP3D-IIM to verify the accuracy of the CFT mixed-mode SIFs with those obtained by external loading. The same procedures mentioned in section 4.2.2 were followed in order to implement the superposition method. The validation of the calculated CFT mixed-mode SIFs with those computed by external loading is shown in Fig. 6.4. A very good matching between the CFT-solutions and external loading solutions was obtained. A percentage difference of less than 1% was obtained at the crack deepest point between the CFT mixed-mode SIFs and those given by external loading.

On the other hand, a difference between the CFT-solutions and those given by external loading was observed at and near the crack mouth (see Fig. 6.4). To understand why this difference was obtained, another verification example of an inclined penny crack embedded in an infinite body was examined using another crack meshing software. The FE model of the second verification example is shown in Fig. 6.5. The FE model generated using FEAcrack software[1]. The FE model represents a one-half symmetric body about x-axis with a semi-elliptical inclined penny crack. The semi-elliptical crack has an aspect ratio (*a*/*c*) of 0.75 with a slant angle of 30°. The FE model generated using 20-noded isoparametric hexahedral elements. The cracked body subjected to a uniaxial stress in z-direction. Young's modulus and Poisson's ratio used in the analysis have values of 206 GPa and 0.3 respectively. The rigid body motion of the models was prevented by applying the minimum displacement constraints, as shown in Fig. 6.5.

---

[1] FE mesh was generated with the assistance from Dr. Greg Thorwald, Quest Integrity

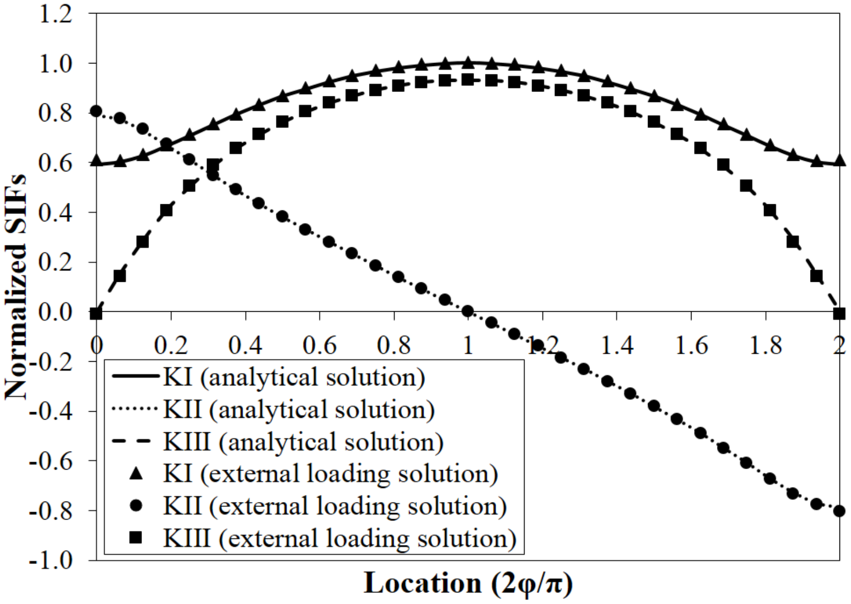

Fig. 6.3 Validation of the external loading mixed-mode SIFs obtained by WARP3D-IIM with those calculated by analytical equations using a Zencrack mesh.

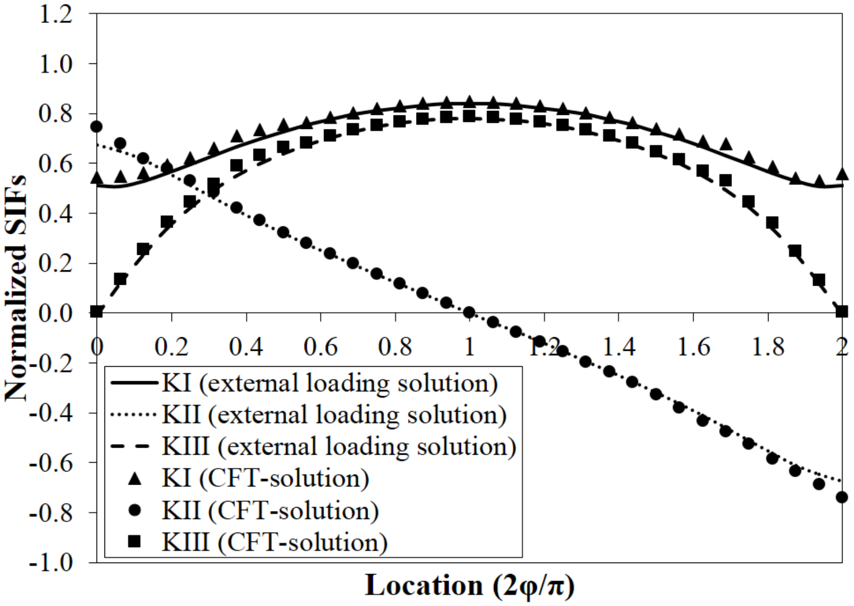

Fig. 6.4 Validation of the calculated CFT mixed-mode SIFs using the modified WARP3D-IIM with those obtained by external loading based on the superposition method using a Zencrack mesh.

The same procedures that conducted for the first verification example (Figs. 6.2–6.4) were also employed for the second verification example. Figure 6.6 illustrates the verification of the external loading solutions with those given by analytical equations. An excellent matching was obtained between the mixed-mode SIFs given by the external loading and analytical equations along the crack front. Moreover, a percentage difference of less than 0.05% between the solutions shown in Fig. 6.6 was obtained at the deepest point.

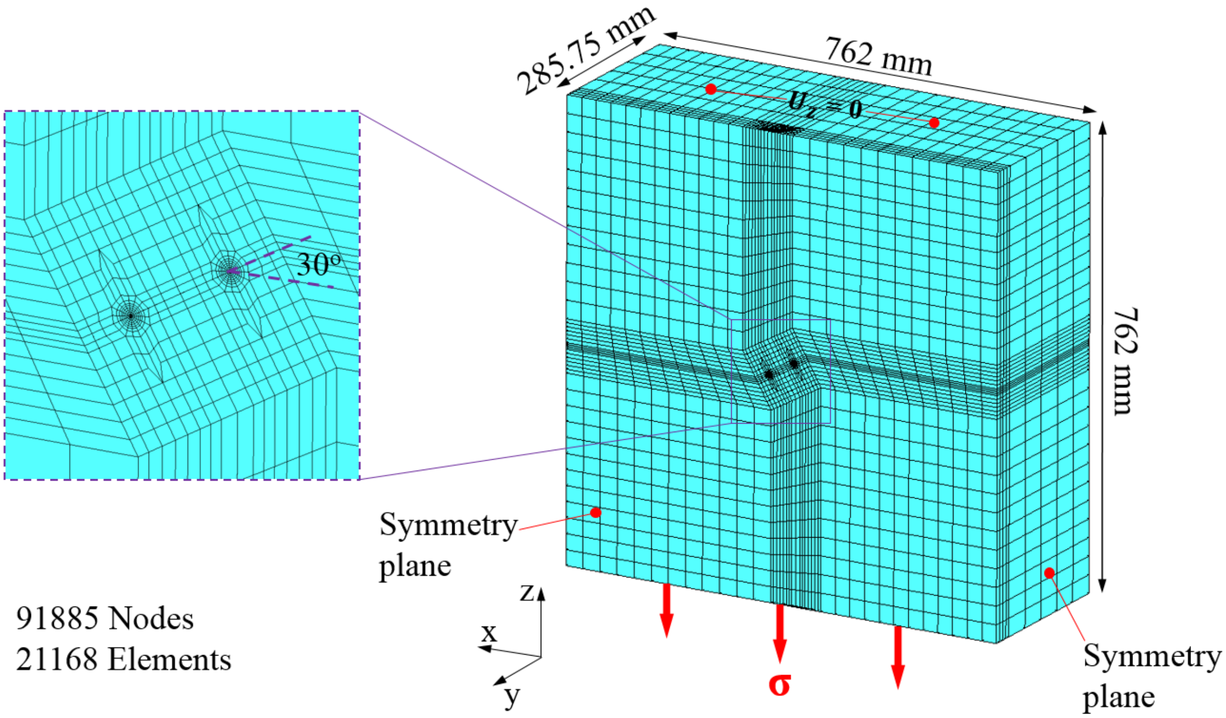

Fig. 6.5 Typical one-half symmetric FE mesh of an inclined penny cracked body using FEAcrack software.

Further, the mixed-mode SIFs calculated using CFT were validated with those given by external loading as shown in Fig. 6.7. The results illustrated in Fig. 6.7 shows an excellent agreement between CFT-solutions and those obtained by external loading with a percentage difference of less than 0.6% along the crack front, in general. Furthermore, a percentage difference of less than 0.5% was obtained between the CFT-solutions and external loading solutions at the deepest point. As well, the CFT-solutions shown in Fig. 6.7 give a smooth behavior especially at the crack mouth locations.

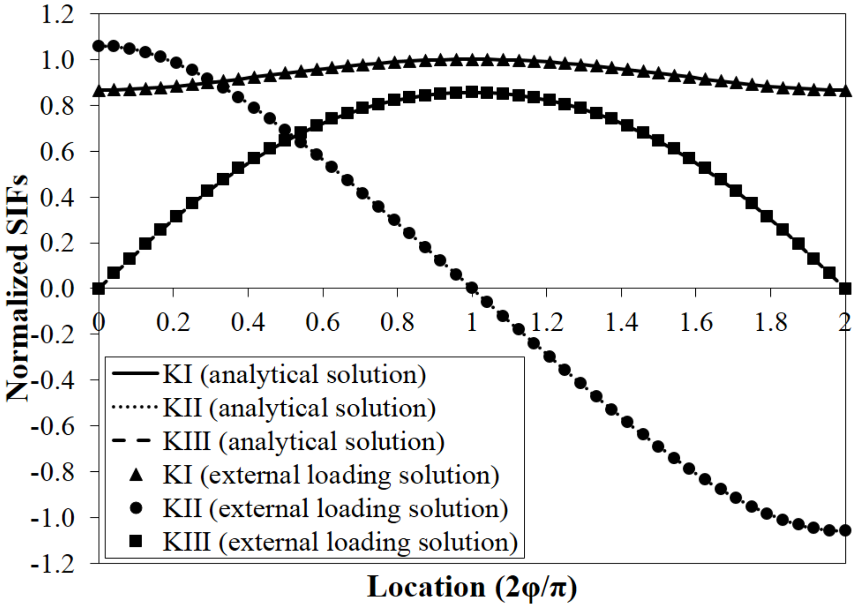

Fig. 6.6 Validation of the external loading mixed-mode SIFs obtained by the WARP3D-IIM with those calculated by analytical equations using a FEAcrack mesh.

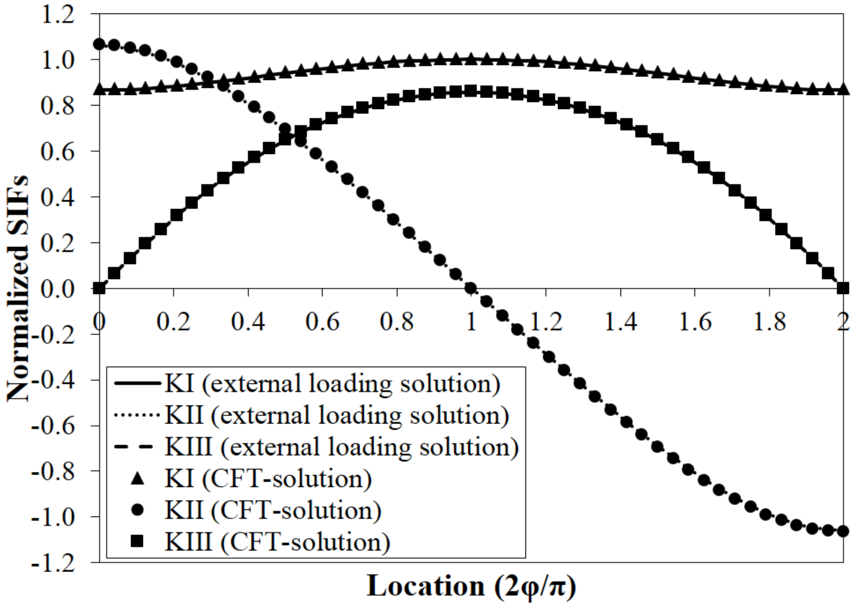

Fig. 6.7 Validation of the calculated CFT mixed-mode SIFs using the modified WARP3D-IIM with those obtained by external load based on the superposition method using a FEAcrack mesh.

To understand why the CFT-solutions given by Zencrack mesh (Fig. 6.4) did not show a smooth behavior at some locations along the crack front (i.e. at and near the crack front), the geometry of the crack face mesh was examined. Figure 6.8 shows a comparison between the crack face meshes generated by Zencrack (see Fig. 6.2) and FEAcrack (see Fig. 6.5). It is clear from Fig. 6.8 (a) that the geometry of the elements adjacent to the crack front shows an abrupt change compared to the geometry of the elements on the crack face. However, the elements adjacent to the crack front in Fig. 6.8 (b) shows a homogenous geometry as those on the crack face.

In the previous chapters, some reasons were mentioned about the difference in SIF between CFT-solutions and those given by external loading at the crack mouth. However, in this chapter, the inhomogeneous behavior of the CFT-SIFs at some locations along the crack front given in Fig. 6.4 may be due to the steep change in the geometry of the elements adjacent to the crack front (see Fig. 6.8 (a)). In addition, the shear stress components that are applied to the crack face may also contribute to the inhomogeneous behavior of the CFT-solutions shown in Fig. 6.4. Based on the results shown in Figs. 6.4 and 6.7 as well as the geometry of the elements adjacent to the crack front illustrated in Fig. 6.8, it is found that the smoothness and accuracy of the calculated CFT-SIFs may influence due to the geometry of the crack face elements. Therefore, an appropriate crack mesh must be prepared to obtain accurate and smooth SIFs. On the other hand, although some SIFs solutions has no smooth behavior at some locations at the crack front when Zencrack mesh is employed. However, the accuracy of the CFT-solutions obtained by the Zencrack mesh gave a very good matching with those obtained by the external loading especially at the crack deepest point.

6.3 Summary

In this study, the WARP3D-IIM was modified based on the Cauchy stress tensor approach in which the normal and shear stress components (i.e. 6-components of stress) can be included in the calculation of the traction forces when a simulated or real non-uniform stress field is applied to the crack face. To verify the adequacy of the modified WARP3D-IIM, an inclined penny crack embedded in an infinite body was examined. Two FE numerical examples were studied using different crack mesh softwares (i.e. Zencrack and FEAcrack). To validate the calculated mixed-mode SIFs for the inclined penny crack problem, the SIFs obtained by the external loading using the WARP3D-IIM were verified firstly with analytical solutions. The percentage difference between the SIFs obtained by the external loading and analytical equations is less than 0.3% for the Zencrack mesh and less than 0.05% for the FEAcrack mesh at the crack deepest point. The superposition method was thereafter employed to evaluate the mixed-mode SIFs based on the modified WARP3D-IIM when a non-uniform stress field with normal and shear components is applied to the crack face. The mixed-mode SIFs calculated by CFT were validated with those given

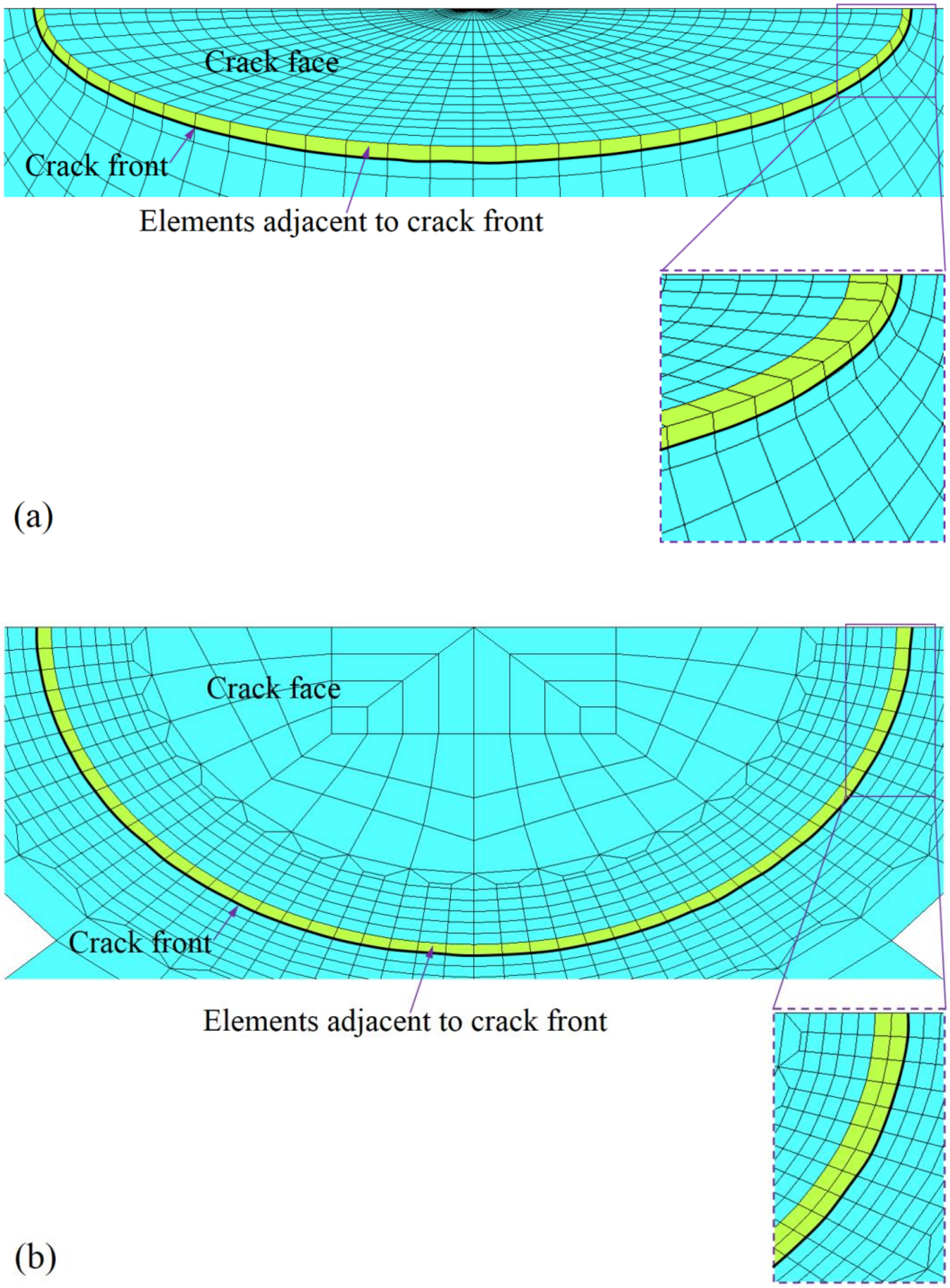

Fig. 6.8 FE crack face mesh. (a) crack mesh generated by Zencrack, and (b) crack mesh generated by FEAcrack.

by external loading for the two numerical examples. A percentage difference of less than 1% was obtained between the SIFs computed by CFT and those given by the external loading at the crack deepest point for the Zencrack mesh. On the other hand, a percentage difference of less than 0.5%

was obtained at the crack deepest point for the FEAcrack mesh. It is observed that the behavior of the CFT-SIFs given by Zencrack mesh is not smooth at some locations at and near the crack front. This behavior may be due to the geometry of the crack face elements adjacent to the crack front. Therefore, an appropriate crack mesh must be employed in order to obtain accurate and smooth SIFs.

CHAPTER 7

Conclusions and further works

7.1 Conclusions

In the present study, a new technique was proposed to evaluate SIFs accurately for fatigue cracks in non-uniform stress fields. The adequacy of the proposed technique was verified using different FE models, loading conditions as well as various welding RS conditions. The proposed technique is appropriate for evaluating SIFs for surface cracks in welded joints. Computation procedures of the proposed technique were described in details, and applications based on the proposed technique were conducted to verify its adequacy and effectiveness.

The summary and conclusions of the present study are summarized for each chapter as follows:

1) A background on RS produced due to welding and their influence on the integrity of structures was addressed. As well, a review of cracks, their types, and their existence in RS fields was given. Moreover, the concept of the SIF and the principle of superposition were introduced. On the other hand, the challenges, faced problems, objectives and outlook related to this study were discussed.

2) A background on the numerical integration methods that used in SIF evaluation for 3-D cracks with crack face tractions was addressed. In addition, an exhaustive review on the mathematical formulations of the DI method and IIM, that form the basis of the numerical procedures used in this study, was given.

3) The superposition method was validated numerically using different FE models by employing the DI and IIM. Furthermore, the significance and effectiveness of the CFT-integral in improving the accuracy of the CFT-solution was discussed. The influence of stress field that arises over the crack surface was included in the SIF solutions by using the superposition method. The accuracy of the numerical DI and IIM has been validated by the CFT cases as well as validation parameters (i.e. U and $CMOD$). To verify the significance of the CFT-integral on the accuracy of the SIF solutions, this study was divided into two parts: 1) evaluation of SIF using face tractions without considering the CFT-integral, and 2) evaluation of SIF using face tractions with considering the CFT-

integral. Based on the numerical analyses results, the following conclusions can be drawn:

- The effectiveness of the CFT-integral was verified for different numerical examples of a flat plate model using WARP3D-IIM with a uniform stress field over the crack face. It was found that the percentage difference between the solutions obtained by the CFT and those given by external loading is less than 0.5% at the crack deepest point.
- The CFT-integral highly improves the accuracy of the CFT-solutions for flat plate models with semi-elliptical surface cracks based on the WARP3D-IIM. The CFT-solutions were improved by 5–6.5% along the crack front (except SIF at the crack mouth) for the examined numerical examples of the flat plate model when compared with the solutions that neglect this integral.
- A percentage difference of less than 5% was obtained at the crack deepest point between the CNT-solutions and those calculated by external loading for the flat plate model and T-butt welded model, using MSC Marc-DI method that neglects the CFT-integral.
- Commercial nonlinear FE codes that neglect the CFT-integral can be used for rough estimation of SIF for engineering fracture mechanics problems under the conditions examined in this study.

4) A new technique was proposed to evaluate SIF for semi-elliptical surface cracks in welding RS fields based on WARP3D-IIM. The influence of the crack-block mesh density on the accuracy of the SIF solutions was examined under different loading conditions. The proposed technique was then validated using different numerical FE examples under different loading conditions. The SIF was thereafter evaluated for a surface cracked butt-welded joint based on real welding RS. Based on the analyses results, the following conclusions can be drawn:

- The proposed technique mainly based on two main points: a) utilizing the CFT-integral implemented in WARP3D-IIM, and b) using a particular crack-block mesh density.
- The crack-block mesh density showed a significant influence on the calculated CFT-solutions along the crack front under different loading conditions. It was observed that when the crack-block mesh becomes fine enough (e.g. $a_1/a \leq 0.06$), the smoothness and accuracy of the CFT-solutions are improved. Thus to take the advantage of the CFT-

integral implemented in WARP3D-IIM and to improve the accuracy of the CFT-solutions, a fine crack-block mesh must be utilized in the employed cracked models.

- Although the CFT-integral that implemented in WARP3D-IIM is available only for crack face bears a uniform distributed stress field; however, when a fine crack-block mesh is used the same CFT-integral can be utilized to evaluate SIF accurately for surface cracks in non-uniform stress fields.
- The results of the different FE examples examined in this chapter showed an excellent agreement between the CFT-solutions and those given by external loading along the crack front especially at the crack deepest point based on the proposed technique.
- By using the proposed technique, a percentage difference of less than 1% was obtained at the crack deepest point between the CFT-solution and that given by external loading for all the numerical examples examined in this chapter.
- The proposed technique was validated for a butt-welded joint using a calculated welding RS. The SIF solutions calculated by the proposed technique gave excellent agreement along the crack front with those obtained by the reference solution (Shiratori's solution).
- The proposed technique was employed to calculate SIF along the crack front for a surface cracked butt-welded joint based on real welding RS. The SIF solutions calculated by real welding RS showed a good agreement with the solution obtained by mechanical loading. As well, negative SIF solutions were obtained when a compressive welding RS was used.
- Simplification of welding RS has a clear influence on the behavior of SIF. Therefore, actual welding RS distribution is highly recommended to be used in order to obtain accurate and realistic SIF solutions.
- The SIF solution obtained by actual welding RS revealed an irregular distribution especially around the crack deepest point. This distribution gave a realistic SIF behavior and showed that some regions of the crack front may propagate faster than other regions.
- A percentage difference of less than 4% was obtained at the crack deepest point between the CNT-solutions and those calculated by external loading using MSC Marc-DI for the studied numerical examples under different loading conditions. Thus, commercial FE codes that omit the CFT-integral can be utilized for rough estimation of SIF for surface

cracks in non-uniform stress fields for engineering problems under the conditions examined in this chapter.

5) The influence of the change in welding HI on welding RS distribution and the behavior of SIF and FCP was investigated using a BOP FE model. As well, the influence of welding RS on the behavior of SIF and FCP was discussed. The proposed technique that introduced in chapter 4 was employed to calculate SIF solutions resulting from welding RS as well as external loading for surface cracks placed at the weld toe. Based on the analyses results; the following conclusions can be drawn:

- The change in welding HI has a clear influence on welding penetration, welding distortion and welding RS distribution. However, it did not give considerable impact on the behavior of SIF and FCP for the applied welding HI cases and selected FE model.
- Based on the simulation results, an uncertainty in the applied welding conditions (i.e. welding HI) may influence the distribution of the induced welding RS. However, this uncertainty in welding conditions may have no considerable impact on the behavior of SIF and FCP.
- A fundamental study was conducted to examine the influence of the change in RS on the behavior of SIF and FCP. For this purpose, engineering equations were formulated to generate different RS distributions over the crack face. It is observed that when the difference in the applied RS is small, the RS has a negligible influence on the behavior of SIF and FCP. However if the difference in the applied RS is large, the RS reveals a considerable impact on the behavior of SIF and FCP.
- Welding RS has a significant influence on the behavior of SIF and FCP when compared with those neglect the influence of welding RS. When welding RS considered in SIF solutions, SIF magnitude significantly increased compared to the case of no welding RS. Therefore, a large reduction in the calculated fatigue lives was observed when welding RS taken into account. A reduction percentage of 37.8%–49.3% in fatigue lives was obtained for the applied stress amplitude loadings.
- The calculated fatigue lives based on the proposed technique that adopted for computing SIF solutions considering welding RS were validated with experiments. As well, the accuracy of the calculated fatigue lives were verified with simulated data.

6) In this study, the WARP3D-IIM was modified based on the Cauchy stress tensor approach in which the normal and shear stress components (i.e. 6-components of stress) can be included in the calculation of the traction forces when a simulated or real non-uniform stress field is applied to the crack face. To verify the adequacy of the modified WARP3D-IIM, an inclined penny crack embedded in an infinite body was examined. Two FE numerical examples were studied using different crack mesh softwares (i.e. Zencrack and FEAcrack). To validate the calculated mixed-mode SIFs for the inclined penny crack problem, the SIFs obtained by the external loading using the WARP3D-IIM were verified firstly with analytical solutions. The percentage difference between the SIFs obtained by the external loading and analytical equations is less than 0.3% for the Zencrack mesh and less than 0.05% for the FEAcrack mesh at the crack deepest point. The superposition method was thereafter employed to evaluate the mixed-mode SIFs based on the modified WARP3D-IIM when a non-uniform stress field with normal and shear components is applied to the crack face. The mixed-mode SIFs calculated by CFT were validated with those given by the external loading for the two numerical examples. A percentage difference of less than 1% was obtained between the SIFs computed by CFT and those given by the external loading at the crack deepest point for the Zencrack mesh. On the other hand, a percentage difference of less than 0.5% was obtained at the crack deepest point for the FEAcrack mesh. It is observed that the behavior of the CFT-SIFs given by Zencrack mesh is not smooth at some locations at and near the crack front. This behavior may be due to the geometry of the crack face elements adjacent to the crack front. Therefore, an appropriate crack mesh must be employed in order to obtain accurate and smooth SIFs.

7.2 Recommendations for future works

1. Although the proposed technique was validated successfully for various numerical examples including cracks in welding RS fields. However, in the proposed technique, RS field is distributed uniformly on each element face over the crack face. For this reason, a fine crack mesh density was proposed in the current proposed technique. When a fine crack mesh density is utilized, small elements with small element faces are obtained over the crack face. Due to the presence of small element faces over the crack face the RS stress can be applied uniformly to each element face where accurate solutions can be obtained. However to introduce a non-uniform stress field to each element face over the crack face, the current

proposed technique should be modified. By modifying the current proposed technique, SIFs solutions with high accuracy are expected to be obtained using a coarse crack mesh density. Based on that, the computation time will be shorter compared to the current proposed technique where the size of the FE model will reduce. As well, the accuracy of SIFs solutions will be guaranteed and improved.

2. Further accurate discussion is needed to examine the FCP based on mean stress range and local welding RS. Where the engineering equations formulated in this study represent macroscopic stress scale through thickness. For this reason, a powerful tool is needed to achieve this target. The crack cohesive force model is considered an efficient tool that deals with local RS at the crack front. By using this model, more accurate FCP can be obtained for fatigue cracks in welding RS fields.
3. The developed WARP3D-IIM, in chapter 6, was examined using a benchmark problem and it was thereafter verified based on the superposition method. However, the capabilities of the developed WARP3D-IIM were not exploited well enough for applications with complicated welded joints including surface cracks. The developed WARP3D-IIM can be employed to calculate SIFs for surface cracks for various practical engineering problems due to its high accuracy. One of the interesting problems that may reveal the effectiveness of the developed WARP3D-IIM is tubular joints. These kind of welded joints offer clear mixed-mode SIFs. The developed WARP3D-IIM can be used to calculate the mixed-mode SIFs accurately and the FCP can be evaluated based on the calculated SIFs. The evaluated mixed-mode SIFs and fatigue life can be validated with well-established references (experiments and/or simulations) to examine the adequacy of the developed WARP3-IIM.

ACKNOWLEDGMENTS

First and foremost, I thank my God from my deep heart for his limitless love, grace, support and for completing this work in such form.

I express from my deep appreciation and my sincere gratitude to my supervisor Prof. Naoki Osawa for his guidance and support during my PhD study. I also gratefully thank Asst. Prof. Satoyuki Tanaka (Hiroshima University) for the great support, fruitful discussions and advices.

I gratefully thank Prof. Masahiko Fujikubo (Osaka University) and Assoc. Prof. Seiichiro Tsutsumi (Osaka University), members of the examination committee, for their support and valuable comments.

Special thanks go to Prof. Robert Dodds, JR, College of Engineering, University of Illinois and member of the WARP3D code developers, for the huge support and valuable comments related to WARP3D code.

I am extremely indebted to Prof. Sherif Rashed for his sincere and invaluable advices, comments, support, patience, and discussions in which were very much appreciated and valuable. Special thanks go to Prof. Hidekazu Murakawa (Osaka University) for the fruitful discussions and huge support. I thank Assoc. Prof. Junichi Katsuta (Nagasaki University) for the fruitful discussion.

Persons who have always been ready to help me are our secretary Ms. Hisami Kamei and Ms. Nobuko Ehira. I deeply thank them for taking care of all my non-scientific works and for their support. Many thanks go to the staff of the department of Naval Architecture and Ocean Engineering for their cooperation and warm help. It is my pleasure to acknowledge all my current and previous colleagues in Prof. Osawa laboratory for their kindness and support.

Special thanks go to Fr. Moisis and Fr. Lokas for their continuous care in Egypt and in Japan. I deeply thank them for their sincere care, support and uninterrupted prayers.

I gratefully thank Fr. Joshua and all the congregation of St. Mary and St. Mark Coptic Orthodox church in Kyoto for their love, support and sharing good memories together. I also acknowledge Fr. David, Fr. George and the congregation of the Russian Orthodox church in Osaka. They gave me happiness in all occasions we communicated together and friendship that I needed.

I deeply thank all who supported me, gave me their hands to make me happy and took care of me during my study.

Lastly but not the least, I warmly thank my beloved parents for their love, encouragement, and continuous prayers for me. I love them so much; I would not have made it this far without their prayers. I also thank my dear sister, her husband and their lovely children Arsanious and Batoul for giving me happiness, encouragement and support.

REFERENCES

[1] R. I. Karlsson and B. L. Josefson, "Three-dimensional finite element analysis of temperatures and stresses in a single-pass butt-welded pipe," *J. Press. Vessel Technol.*, vol. 112, no. 1, pp. 76–84, 1990.

[2] B. Taljat, B. Radhakrishnan, and T. Zacharia, "Numerical analysis of GTA welding process with emphasis on post-solidification phase transformation effects on residual stresses," *Mater. Sci. Eng. A*, vol. 246, no. 1–2, pp. 45–54, 1998.

[3] A. Ohta, K. Matsuoka, N. T. Nguyen, Y. Maeda, and N. Suzuki, "Fatigue strength improvement of lap joints of thin steel plate using low-transformation- temperature welding wire," *Weld. J.*, vol. 82, pp. 78–83, 2003.

[4] P. J. Withers, "Residual stress and its role in failure," *Rep. Prog. Phys.*, vol. 70, pp. 2211–2264, 2007. http://iopscience.iop.org/0034-4885/70/12/R04

[5] J. Altenkirch, J. Gibmeier, A. Kromm, T. Kannengiesser, T. Nitschke-Pagel, and M. Hofmann, "In situ study of structural integrity of low transformation temperature (LTT)-welds," *Mater. Sci. Eng. A*, vol. 528, no. 16–17, pp. 5566–5575, 2011.

[6] UNITOR, *Maritime Welding Handbook: Welding and Related Processes for Repair and Maintenance Onboard*, 14th ed. https://www.wilhelmsen.com/globalassets/marine-products/welding/documents/wilhelmsen-ships-service---unitor-welding-handbook.pdf

[7] KOBELCO, *Weld Imperfections and Preventive Measures*. KOBE STEEL, LTD., 2015.

[8] X. Qian, S. Swaddiwudhipong, C. T. Nguyen, Y. Petchdemaneengam, P. Marshall, and Z. Ou, "Overload effect on the fatigue crack propagation in large-scale tubular joints," *Fatigue Fract. Eng. Mater. Struct.*, vol. 36, no. 5, pp. 427–438, 2013.

[9] S. Tanaka, S. Okazawa, H. Okada, Y. Xi, and Y. Ohtsuki, "Analysis of three-dimensional surface cracks in a welded joint structure using the shell-solid mixed method," *Int. J. Offshore Polar Eng.*, vol. 23, pp. 232–239, 2013.

[10] X. R. Wu and J. Carlsson, "Welding residual stress intensity factors for half-elliptical surface cracks in thin and thick plates," *Eng. Fract. Mech.*, vol. 19, no. 3, pp. 407–426, 1984.

[11] Y. Lu, "A practical procedure for evaluating SIFs along fronts of semi-elliptical surface cracks at weld toes in complex stress fields," *Int. J. Fatigue*, vol. 18, no. 2, pp. 127–135, 1996.

[12] T. Nakamura, K. Taniguchi, S. Hirano, N. Marekazu, and T. Sato, "Stress corrosion cracking in welds of reactor vessel nozzle at Ohi-3 and of other vessel's nozzle at Japan's PWR plants," in *Volume 1: Codes and Standards*, 2009, pp. 629–637.

[13] S. N. Atluri, S. G. Sampath, and P. Tong, Eds., *Structural Integrity of Aging Airplanes*. Verlag Berlin Heidelberg: Springer, 1991.

[14] T. L. Anderson, *Fracture Mechanics: Fundamentals and Applications*, 3rd ed. Florida, USA: CRC Press, Taylor & Francis Group, 2005.

[15] D. Radaj, "Extended Stress Intensity Factor Concepts," in *Advanced Methods of Fatigue Assessment*, Berlin, Heidelberg: Springer Berlin Heidelberg, 2013, pp. 101–265.

[16] D. Radaj and S. Zhang, “Analogies between crack tip and rigid line tip stresses and displacements,” *Eng. Fract. Mech.*, vol. 44, no. 6, pp. 913–919, 1993.

[17] S. J. Maddox, *Fatigue Strength of Welded Structures*, 2nd ed. Abington publishing, 1991.

[18] R. Bao, X. Zhang, and N. A. Yahaya, “Evaluating stress intensity factors due to weld residual stresses by the weight function and finite element methods,” *Eng. Fract. Mech.*, vol. 77, no. 13, pp. 2550–2566, 2010.

[19] L. Fratini, S. Pasta, and A. Reynolds, “Fatigue crack growth in 2024-T351 friction stir welded joints: Longitudinal residual stress and microstructural effects,” *Int. J. Fatigue*, vol. 31, no. 3, pp. 495–500, 2009.

[20] G. Pouget and A. P. Reynolds, “Residual stress and microstructure effects on fatigue crack growth in AA2050 friction stir welds,” *Int. J. Fatigue*, vol. 30, no. 3, pp. 463–472, 2008.

[21] M. Beghini, L. Bertini, and E. Vitale, “Fatigue crack growth in residual stress fields: Experimental results and modelling,” *Fatigue Fract. Eng. Mater. Struct.*, vol. 17, no. 12, pp. 1433–1444, 1994.

[22] T. Nagashima and N. Miura, “Crack analysis in residual stress field by X-FEM,” *J. Comput. Sci. Technol.*, vol. 3, no. 1, pp. 136–147, 2009.

[23] J. R. Rice, “A path independent integral and the approximate analysis of strain concentration by notches and cracks,” *J. Appl. Mech.*, vol. 35, no. 2, pp. 379–386, 1968.

[24] J. K. Knowles and E. Sternberg, “On a class of conservation laws in linearized and finite elastostatics,” *Arch. Ration. Mech. Anal.*, vol. 44, no. 3, pp. 187–211, 1972.

[25] B. Budiansky and J. R. Rice, “Conservation laws and energy-release rates,” *J. Appl. Mech.*, vol. 40, no. 1, pp. 201–203, 1973.

[26] B. Healy, A. Gullerud, K. Koppenhoefer, A. Roy, S. RoyChowdhury, J. Petti, M. Walters, B. Bichon, K. Cochran, A. Carlyle, J. Sobotka, M. Messner, and R. Dodds, “WARP3D-Release 17.6.0,” Report No. UILU-ENG-95-2012, Civil Engineering, University of Illinois, Urbana, IL 61801, USA, 2015.

[27] M. Beghini and L. Bertini, “Fatigue crack propagation through residual stress fields with closure phenomena,” *Eng. Fract. Mech.*, vol. 36, no. 3, pp. 379–387, 1990.

[28] G. Servetti and X. Zhang, “Predicting fatigue crack growth rate in a welded butt joint: The role of effective R ratio in accounting for residual stress effect,” *Eng. Fract. Mech.*, vol. 76, no. 11, pp. 1589–1602, 2009.

[29] G. Labeas and I. Diamantakos, “Numerical investigation of through crack behaviour under welding residual stresses,” *Eng. Fract. Mech.*, vol. 76, no. 11, pp. 1691–1702, 2009.

[30] M. Gosz and B. Moran, “An interaction energy integral method for computation of mixed-mode stress intensity factors along non-planar crack fronts in three dimensions,” *Eng. Fract. Mech.*, vol. 69, no. 3, pp. 299–319, 2002.

[31] C. F. Shih, B. Moran, and T. Nakamura, “Energy release rate along a three-dimensional crack front in a thermally stressed body,” *Int. J. Fract.*, vol. 30, no. 2, pp. 79–102, 1986.

[32] B. Moran and C. F. Shih, “A general treatment of crack tip contour integrals,” *Int. J. Fract.*, vol. 35, no. 4, pp. 295–310, Dec. 1987.

[33] B. Moran and C. F. Shih, “Crack tip and associated domain integrals from momentum and energy balance,” *Eng. Fract. Mech.*, vol. 27, no. 6, pp. 615–642, Jan. 1987.

[34] R. H. Dodds and P. M. Vargas, “Numerical evaluation of domain and contour integrals for nonlinear fracture mechanics: Formulation and implementation aspect,” Report No. UILU-ENG-88-2006, 1988.

[35] G. P. Nikishkov and S. N. Atluri, “Calculation of fracture mechanics parameters for an arbitrary three-dimensional crack, by the ‘equivalent domain integral’ method,” *Int. J. Numer. Methods Eng.*, vol. 24, no. 9, pp. 1801–1821, 1987.

[36] K. N. Shivakumar and I. S. Raju, “An equivalent domain integral method for three-dimensional mixed-mode fracture problems,” *Eng. Fract. Mech.*, vol. 42, no. 6, pp. 935–959, 1992.

[37] M. C. Walters, G. H. Paulino, and R. H. Dodds, “Interaction integral procedures for 3-D curved cracks including surface tractions,” *Eng. Fract. Mech.*, vol. 72, no. 11, pp. 1635–1663, 2005.

[38] M. Stern, E. B. Becker, and R. S. Dunham, “A contour integral computation of mixed-mode stress intensity factors,” *Int. J. Fract.*, vol. 12, no. 3, pp. 359–368, 1976.

[39] J. F. Yau, S. S. Wang, and H. T. Corten, “A mixed-mode crack analysis of isotropic solids using conservation laws of elasticity,” *J. Appl. Mech.*, vol. 47, no. 2, pp. 335–341, 1980.

[40] S. S. Wang, J. F. Yau, and H. T. Corten, “A mixed-mode crack analysis of rectilinear anisotropic solids using conservation laws of elasticity,” *Int. J. Fract.*, vol. 16, no. 3, pp. 247–259, 1980.

[41] T. Nakamura and D. M. Parks, “Antisymmetrical 3-D stress field near the crack front of a thin elastic plate,” *Int. J. Solids Struct.*, vol. 25, no. 12, pp. 1411–1426, 1989.

[42] I. S. Raju and K. N. Shivakumar, “An equivalent domain integral method in the two-dimensional analysis of mixed mode crack problems,” *Eng. Fract. Mech.*, vol. 37, no. 4, pp. 707–725, 1990.

[43] P. P. L. Matos, R. M. McMeeking, P. G. Charalambides, and M. D. Drory, “A method for calculating stress intensities in bimaterial fracture,” *Int. J. Fract.*, vol. 40, no. 4, pp. 235–254, 1989.

[44] T. Nakamura, “Three-dimensional stress fields of elastic interface cracks,” *J. Appl. Mech.*, vol. 58, no. 4, pp. 939–946, 1991.

[45] M. Gosz, J. Dolbow, and B. Moran, “Domain integral formulation for stress intensity factor computation along curved three-dimensional interface cracks,” *Int. J. Solids Struct.*, vol. 35, no. 15, pp. 1763–1783, 1998.

[46] X. Qian, R. H. Dodds, and Y. S. Choo, “Mode mixity for tubular K-joints with weld toe cracks,” *Eng. Fract. Mech.*, vol. 73, no. 10, pp. 1321–1342, 2006.

[47] B. N. Rao and S. Rahman, “An interaction integral method for analysis of cracks in orthotropic functionally graded materials,” *Comput. Mech.*, vol. 32, no. 1–2, pp. 40–51, 2003.

[48] J.-H. Kim and G. H. Paulino, “Consistent formulations of the interaction integral method

for fracture of functionally graded materials," *J. Appl. Mech.*, vol. 72, no. 3, pp. 351–364, 2005.

[49] G. H. Paulino and J.-H. Kim, "A new approach to compute T-stress in functionally graded materials by means of the interaction integral method," *Eng. Fract. Mech.*, vol. 71, no. 13–14, pp. 1907–1950, 2004.

[50] J.-H. Kim and G. H. Paulino, "T-stress, mixed-mode stress intensity factors, and crack initiation angles in functionally graded materials: A unified approach using the interaction integral method," *Comput. Methods Appl. Mech. Eng.*, vol. 192, no. 11–12, pp. 1463–1494, 2003.

[51] J. Johnson and J. Qu, "An interaction integral method for computing mixed mode stress intensity factors for curved bimaterial interface cracks in non-uniform temperature fields," *Eng. Fract. Mech.*, vol. 74, no. 14, pp. 2282–2291, 2007.

[52] H. Yu, L. Wu, L. Guo, Q. He, and S. Du, "Interaction integral method for the interfacial fracture problems of two nonhomogeneous materials," *Mech. Mater.*, vol. 42, no. 4, pp. 435–450, 2010.

[53] H. Yu, L. Wu, L. Guo, H. Wu, and S. Du, "An interaction integral method for 3D curved cracks in nonhomogeneous materials with complex interfaces," *Int. J. Solids Struct.*, vol. 47, no. 16, pp. 2178–2189, 2010.

[54] H. Yu, L. Wu, L. Guo, S. Du, and Q. He, "Investigation of mixed-mode stress intensity factors for nonhomogeneous materials using an interaction integral method," *Int. J. Solids Struct.*, vol. 46, no. 20, pp. 3710–3724, 2009.

[55] R. Daimon and H. Okada, "Mixed-mode stress intensity factor evaluation by interaction integral method for quadratic tetrahedral finite element with correction terms," *Eng. Fract. Mech.*, vol. 115, pp. 22–42, 2014.

[56] N. Sukumar, N. Moes, B. Moran, and T. Belytschko, "Extended finite element method for three-dimensional crack modelling," *Int. J. Numer. Methods Eng.*, vol. 48, no. 11, pp. 1549–1570, 2000.

[57] N. Moes, A. Gravouil, and T. Belytschko, "Non-planar 3D crack growth by the extended finite element and level sets-Part I: Mechanical model," *Int. J. Numer. Methods Eng.*, vol. 53, no. 11, pp. 2549–2568, 2002.

[58] H. Yu, L. Wu, L. Guo, H. Li, and S. Du, "T-stress evaluations for nonhomogeneous materials using an interaction integral method," *Int. J. Numer. Methods Eng.*, vol. 90, no. 11, pp. 1393–1413, 2012.

[59] R. Nahta and B. Moran, "Domain integrals for axisymmetric interface crack problems," *Int. J. Solids Struct.*, vol. 30, no. 15, pp. 2027–2040, 1993.

[60] M. L. Williams, "On the stress distribution at the base of a stationary crack," *J. Appl. Mech.*, vol. 24, pp. 109–114, 1957.

[61] D. Bowness and M. M. K. Lee, "Prediction of weld toe magnification factors for semi-elliptical cracks in T-butt joints," *Int. J. Fatigue*, vol. 22, no. 5, pp. 369–387, 2000.

[62] FEAcrack User's Manual, "3D finite element software for cracks version 3.2 Quest Integrity

Group," 2010.

[63] Zencrack, "User manual for Zencrack 7.2 version 7.2 Zentech Inc.," 2003.

[64] J. C. Newman and I. S. Raju, "Stress-intensity Factor Equations for Cracks in Three-dimensional Finite Bodies Subjected to Tension and Bending Loads," Technical memorandum No. 85793, NASA, Langley Research Center, Hampton, VA, 1984.

[65] J. C. Newman and I. S. Raju, "An empirical stress-intensity factor equation for the surface crack," *Eng. Fract. Mech.*, vol. 15, no. 1–2, pp. 185–192, 1981.

[66] J. C. Newman and I. S. Raju, "Analyses of surface cracks in finite plates under tension or bending loads," Technical paper No. 1578, NASA, Langley Research Center, Hampton, VA., 1979.

[67] BSI Standards Publication, "Guide to methodes for assessing the acceptability of flaws in metallic structures," BS 7910:2013+A1, 2015.

[68] S. Tanaka, T. Kawahara, and H. Okada, "Study on crack propagation simulation of surface crack in welded joint structure," *Mar. Struct.*, vol. 39, pp. 315–334, 2014.

[69] R. Gadallah, N. Osawa, and S. Tanaka, "Numerical estimation on stress intensity factors for surface cracks in a welding residual stress field," in *ASME 2016 35th International Conference on Ocean, Offshore and Arctic Engineering*, 2016, OMAE2016-54495.

[70] R. Gadallah, N. Osawa, and S. Tanaka, "Numerical evaluation of stress intensity factors of three-dimensional surface cracks in welded joints using the superposition method," in *Japan Society of Naval Architects and Ocean Engineers*, 2015, pp. 389–394.

[71] R. Gadallah, N. Osawa, and S. Tanaka, "Evaluation of stress intensity factor for a surface cracked butt welded joint based on real welding residual stress," *Ocean Eng.*, vol. 138, pp. 123–139, 2017.

[72] R. Gadallah, N. Osawa, and S. Tanaka, "Calculation of SIFs along a 3-D Crack Front with the Interaction Integral Method Using a Non-Uniform Residual Stress Field," in *Japan Society of Naval Architects and Ocean Engineers*, 2016, pp. 447–452.

[73] J. H. L. Pang, K. S. Tsang, and H. J. Hoh, "3D stress intensity factors for weld toe semi-elliptical surface cracks using XFEM," *Mar. Struct.*, vol. 48, pp. 1–14, 2016.

[74] D. Bowness and M. M. K. Lee, "Stress intensity factor solutions for semi-elliptical weld-toe cracks in t-butt geometries," *Fatigue Fract. Eng. Mater. Struct.*, vol. 19, no. 6, pp. 787–797, 1996.

[75] M. Shiratori, T. Miyoshi, and K. Tanikawa, "Analysis of stress intensity factors for surface cracks subjected to arbitrarily distributed surface stresses," *Trans. Japan Soc. Mech. Eng. Ser. A*, vol. 52, pp. 390–398, 1986.

[76] R. Gadallah, S. Tsutsumi, K. Hiraoka, and H. Murakawa, "Prediction of residual stresses induced by low transformation temperature weld wires and its validation using the contour method," *Mar. Struct.*, vol. 44, pp. 232–253, 2015.

[77] E. Ostertagová and O. Ostertag, "Forecasting using simple exponential smoothing method," *Acta Electrotech. Inform.*, vol. 12, no. 3, pp. 62–66, 2012.

[78] C.-H. Lee, K.-H. Chang, and V. N. Van Do, "Modeling the high cycle fatigue behavior of

T-joint fillet welds considering weld-induced residual stresses based on continuum damage mechanics," *Eng. Struct.*, vol. 125, pp. 205–216, 2016.

[79] C.-H. Lee and K.-H. Chang, "Finite element computation of fatigue growth rates for mode I cracks subjected to welding residual stresses," *Eng. Fract. Mech.*, vol. 78, no. 13, pp. 2505–2520, 2011.

[80] K. Hemmesi, M. Farajian, and A. Fatemi, "Application of the critical plane approach to the torsional fatigue assessment of welds considering the effect of residual stresses," *Int. J. Fatigue*, vol. 101, pp. 271–281, 2017.

[81] D. Tchoffo Ngoula, H. T. Beier, and M. Vormwald, "Fatigue crack growth in cruciform welded joints: Influence of residual stresses and of the weld toe geometry," *Int. J. Fatigue*, vol. 101, pp. 253–262, 2017.

[82] P. Rettenmeier, E. Roos, and S. Weihe, "Fatigue analysis of multiaxially loaded crane runway structures including welding residual stress effects," *Int. J. Fatigue*, vol. 82, pp. 179–187, 2016.

[83] T. H. Tra, M. Okazaki, and K. Suzuki, "Fatigue crack propagation behavior in friction stir welding of AA6063-T5: Roles of residual stress and microstructure," *Int. J. Fatigue*, vol. 43, pp. 23–29, 2012.

[84] W. V. Vaidya, P. Staron, and M. Horstmann, "Fatigue crack propagation into the residual stress field along and perpendicular to laser beam butt-weld in aluminium alloy AA6056," *Fatigue Fract. Eng. Mater. Struct.*, vol. 35, no. 5, pp. 399–411, 2012.

[85] E. Mikkola, M. Dore, G. Marquis, and M. Khurshid, "Fatigue assessment of high-frequency mechanical impact (HFMI)-treated welded joints subjected to high mean stresses and spectrum loading," *Fatigue Fract. Eng. Mater. Struct.*, vol. 38, no. 10, pp. 1167–1180, 2015.

[86] S. Kusuba, "Study on fatigue life assessment by crack monitoring and simulation," PhD dissertation, Nagasaki University, 2007. (in Japanese)

[87] D. Deng and H. Murakawa, "Influence of transformation induced plasticity on simulated results of welding residual stress in low temperature transformation steel," *Comput. Mater. Sci.*, vol. 78, pp. 55–62, 2013.

[88] N. Ma, Z. Cai, H. Huang, D. Deng, H. Murakawa, and J. Pan, "Investigation of welding residual stress in flash-butt joint of U71Mn rail steel by numerical simulation and experiment," *Mater. Des.*, vol. 88, pp. 1296–1309, 2015.

[89] H. Murakawa, M. Beres, C. M. Davies, S. Rashed, A. Vega, M. Tsunori, K. M. Nikbin, and D. Dye, "Effect of low transformation temperature weld filler metal on welding residual stress," *Sci. Technol. Weld. Join.*, vol. 15, no. 5, pp. 393–399, 2010.

[90] H. Murakawa, N. Ma, and H. Huang, "Iterative substructure method employing concept of inherent strain for large-scale welding problems," *Weld. World*, vol. 59, no. 1, pp. 53–63, 2015.

[91] M. Klesnil and P. Lukas, "Influence of strength and stress history on growth and stabilisation of fatigue cracks," *Eng. Fract. Mech.*, vol. 4, no. 1, pp. 77–92, 1972.

[92] R. Kumar, "Review on crack closure for constant amplitude loading in fatigue," *Eng. Fract.*

Mech., vol. 42, no. 2, pp. 389–400, 1992.

[93] W. Elber, “The significance of fatigue crack closure,” in *Damage Tolerance in Aircraft Structures*, West Conshohocken, PA 19428-2959: ASTM International, 1971. Doi: 10.1520/STP26680S

[94] D. Simunek, M. Leitner, J. Maierhofer, and H.-P. Gänser, “Fatigue crack growth under constant and variable amplitude loading at semi-elliptical and V-notched steel specimens,” *Procedia Eng.*, vol. 133, pp. 348–361, 2015.

[95] S. M. Beden, S. Abdullah, and A. K. Ariffin, “Factors affecting the fatigue crack growth behavior of metallic structure under variable amplitude,” in *Malaysian Metallurgical Conference-MMC*, 2008. Doi: 10.13140/2.1.2454.3045

[96] S. Roth, G. Hütter, and M. Kuna, “Simulation of fatigue crack growth with a cyclic cohesive zone model,” *Int. J. Fract.*, vol. 188, no. 1, pp. 23–45, 2014.

[97] A. Ural, V. R. Krishnan, and K. D. Papoulia, “A cohesive zone model for fatigue crack growth allowing for crack retardation,” *Int. J. Solids Struct.*, vol. 46, no. 11–12, pp. 2453–2462, 2009.

[98] J. L. Bouvard, J. L. Chaboche, F. Feyel, and F. Gallerneau, “A cohesive zone model for fatigue and creep–fatigue crack growth in single crystal superalloys,” *Int. J. Fatigue*, vol. 31, no. 5, pp. 868–879, 2009.

[99] B. Yang, S. Mall, and K. Ravi-Chandar, “A cohesive zone model for fatigue crack growth in quasibrittle materials,” *Int. J. Solids Struct.*, vol. 38, no. 22–23, pp. 3927–3944, 2001.

[100] W. H. Press, S. A. Teukolsky, W. T. Vetterling, and B. P. Flannery, “Numerical recipies in Fortran 77,” *Press Synd. Univ. Cambridge, Cambridge*, 2001.

[101] G. Evans, *Practical Numerical Integration*. John Wiley and Sons, Chichester, 1993.

[102] M. K. Kassir and G. C. Sih, “Three-dimensional stress distribution around an elliptical crack under arbitrary loadings,” *J. Appl. Mech.*, vol. 33, no. 3, pp. 601–611, 1966.

Publications related to this study

1. Journal papers

[1] R. Gadallah, N. Osawa, and S. Tanaka, “Evaluation of stress intensity factor for a surface cracked butt welded joint based on real welding residual stress,” *Ocean Eng.*, vol. 138, pp. 123–139, 2017.

[2] R. Gadallah, S. Tsutsumi, K. Hiraoka, and H. Murakawa, “Prediction of residual stresses induced by low transformation temperature weld wires and its validation using the contour method,” *Mar. Struct.*, vol. 44, pp. 232–253, 2015.

2. Conference papers/proceedings

[1] R. Gadallah, N. Osawa and S. Tanaka, “Influence of welding heat input and welding residual stress on fracture parameter and fatigue crack propagation of a bead-on-plate specimen”, Proceedings in: the 70th IIW Annual Assembly and International Conference, 25-30 June, 2017, Shanghai, China. IIW Doc. No. XIII-2700-17.

[2] R. Gadallah, N. Osawa and S. Tanaka, “Numerical estimation on stress intensity factors for surface cracks in a welding residual stress field”, Proceedings in: the 69th IIW Annual Assembly and International Conference, 10-15 July, 2016, Melbourne, Australia. IIW Doc. No. XIII-2652-16.

[3] R. Gadallah, N. Osawa, and S. Tanaka, “Numerical estimation on stress intensity factors for surface cracks in a welding residual stress field,” in *ASME 2016 35th International Conference on Ocean, Offshore and Arctic Engineering*, 2016. doi:10.1115/OMAE2016-54495.

[4] R. Gadallah, N. Osawa, and S. Tanaka, “Calculation of SIFs along a 3-D crack front with the interaction integral method using a non-uniform residual stress field”, Proceedings in: the Japan Society of Naval Architects and Ocean Engineers (JASNAOE), 26- 27 May 2016, Vol. 22, pp. 447-452, ISSN 2185-1840.

[5] R. Gadallah, N. Osawa, and S. Tanaka, “Numerical evaluation of stress intensity factors of three-dimensional surface cracks in welded joints using the superposition method”, Proceedings in: the Japan Society of Naval Architects and Ocean Engineers (JASNAOE), 16, 17 Nov. 2015, Vol. 21, pp. 389-394, ISSN 2185-1840.

3. Paper under review

[1] R. Gadallah, N. Osawa, and S. Tanaka, “Influence of welding heat input and welding residual stress on fracture parameter and fatigue crack propagation of a bead-on-plate specimen,” Fatigue & Fracture of Engineering Materials & Structures.